

University of St Andrews



Full metadata for this thesis is available in
St Andrews Research Repository
at:

<http://research-repository.st-andrews.ac.uk/>

This thesis is protected by original copyright

QUANTITATIVE ASPECTS OF LASER MICRO-SPECTRAL ANALYSIS

**A thesis
presented by
J Watson, Grad Inst P
to the
University of St Andrews
in application for the Degree
of Doctor of Philosophy**



Th 9241



Frontispiece :

Vaporisation of a steel target by focused radiation from an RO-mode Nd-glass laser (ave power density = 40 GW m^{-2}).

FOR JOYCE

CERTIFICATE

I certify that J Watson, Grad Inst P, has spent nine terms at research work in the School of Physical Sciences, in the University of St Andrews, under my direction, that he has fulfilled the conditions of Ordinance No 12 and resolution of the University Court, 1967, No 1 and that he is qualified to submit the accompanying thesis in application for the Degree of Doctor of Philosophy.

Research Supervisor

DECLARATION

I hereby certify that this thesis has been composed by me, and is a record of work done by me, and has not previously been presented for a Higher Degree.

This research was carried out in the School of Physical Sciences at the University of St Andrews, under the supervision of Dr A Maitland.

J Watson

CAREER

The author attended Beath High School, Cowdenbeath and Boroughmuir Secondary School, Edinburgh before joining Hilger Electronics, Dalkeith in 1967. After three years with Hilger Electronics initially, as a Draughtsman and finally as an Electro-Optics Technician, he spent one year with Microwave and Electronic Systems Ltd, Newbridge as a Development Engineer. During this time he attended Napier College, Edinburgh by day release, obtaining a Higher National Certificate in Applied Physics in 1970 and adding three Supplementary Endorsements in 1971. From August 1972, the Author attended Napier College full time, and was awarded the Graduateship of the Institute of Physics with middle honours in July 1973. From October 1973 until September 1976, the Author was engaged as a Research Student in the School of Physical Sciences at the University of St Andrews, under the supervision of Dr A Maitland. While at St Andrews, he investigated the spectroscopic behaviour of laser - produced vaporisation of solid targets with application to the spectrochemical analysis of steels. Since October 1976, he has been employed as a Higher Scientific Officer at Dounreay Nuclear Power Development Establishment engaged in the development of scientific instruments for use in the Fuel Reprocessing Cycle.

ACKNOWLEDGEMENTS

I would like to express my sincere thanks to my Supervisor, Dr A Maitland, to whom I owe a great deal for all the advice and support he has given me over the past five years. Also, I would like to thank my friend and associate Dr R S Adrain, of Marchwood Engineering Laboratories, for his great help and encouragement. Among the others to whom I owe thanks are: my past colleagues in the School of Physical Sciences with whom I have had many helpful discussions, especially Mr H Shields, Dr J N Ross and Dr M H Dunn; Mrs J Izatt for typing the manuscript; Mr T McQueen for reproducing it; and Mr C Jones (Dounreay Nuclear Establishment) and Mr B McAndie for copying the photographs and diagrams. Finally I would like to acknowledge the support of the Science Research Council, who awarded me a Research Studentship to carry out this work and the co-operation of CZ Instruments Ltd and their permission to use photographs in this thesis.

ABSTRACT

For quantitative Laser Micro-Spectral Analysis, two modes of laser operation are used to produce plasmas at metal surfaces, viz relaxation oscillator mode and Q-switched mode. Application of a spark discharge across either of these plasmas enhances the spectral emission from them. The plasmas which result from these excitation modes differ in a number of physical characteristics which influence their suitability as excitation sources for spectrochemical analysis.

The temporal and spatial behaviour of laser-produced plasmas was studied using time-integrated and time-resolved spectroscopy. From this work, the plasmas were characterised in terms of expansion velocity, electron temperature and electron density. The experimental results obtained are compared with those predicted by the Krokhin models of plasma production. For successful quantitative analysis, the plasmas should exist in a state of local thermodynamic equilibrium and this is shown to be the case for all the plasmas considered here. The temporal behaviour of plasmas produced by Q-switched lasers suggested that the emission spectrum could be simplified (with an improvement in line-to-background ratio) by gating the continuum and multiply-ionised species emission from the atomic species emission. One method of achieving this is described.

Quantitative analysis of steels is discussed and working curves of spectral line intensity against minor constituent concentration are presented for each of the modes of operation. The curves are compared in terms of the precision of the predicted concentration of a minor constituent.

QUANTITATIVE ASPECTS OF LASER MICRO-SPECTRAL ANALYSIS

1.	<u>PRINCIPLES OF LASER MICRO-SPECTRAL ANALYSIS</u>	1.1
1.1	INTRODUCTION	1.1
1.2	LASER-PRODUCED VAPORISATION OF SOLID TARGETS	1.5
1.2.1	Basic Phenomena	1.5
1.2.2	Low Temperature Regime	1.9
1.2.3	High Temperature Regime	1.11
1.3	PLASMA EMISSION AND SPECTROCHEMICAL ANALYSIS	1.14
1.3.1	Local Thermodynamic Equilibrium (LTE)	1.15
1.3.2	Spectral Intensity and Equilibrium Relationships	1.17
1.3.3	Electron Temperature and Electron Density	1.19
1.3.4	Photographically Measured Spectral Intensities	1.20
1.3.5	Spectrochemical Analysis	1.22
1.4	LASER MICRO-SPECTRAL ANALYSIS	1.23
1.5	SUMMARY	1.26

FIGURES 1.1, 1.2.

2.	<u>EXPERIMENTAL TECHNIQUES AND INSTRUMENTATION</u>	2.1
2.1	THE LASER MICROANALYSER LMA-1	2.1
2.1.1	The Laser	2.1
2.1.2	Laser Output Parameters	2.3
2.1.3	Auxiliary Spark Discharge	2.5
2.2	QUARTZ SPECTROGRAPH	2.6
2.2.1	Spectrograph Illumination	2.6
2.3	PHOTOGRAPHIC TECHNIQUES AND MATERIALS	2.8
2.3.1	Film and Plate Development	2.8
2.3.2	Plate Calibration by the Preliminary Curve Method	2.9
2.4	IMAGE CONVERTER CAMERA	2.11
2.4.1	Image Converter Camera Model 1D	2.11
2.4.2	Streak and Framing Units	2.12
2.4.3	STL Trigger Delay Generator Model 2A	2.13

FIGURES 2.1 - 2.9.

3.	<u>SPECTROSCOPY OF LASER PRODUCED PLASMAS</u>	3.1
3.1	TIME AND SPATIALLY INTEGRATED SPECTRA	3.1
3.2	TIME AND SPATIALLY RESOLVED SPECTRA	3.4
3.2.1	Unsparked Plasmas	3.5
3.2.2	Line-to-Background Ratios	3.8

3.2.3	Time and Spatially Resolved Plasma Parameters	3.8
3.2.4	Ejection Velocity and Kinetic Energy	3.12
3.2.5	Spark-assisted Plasmas	3.12
3.3	CONCLUSION	3.13
	FIGURES 3.1 - 3.10	
4.	<u>ELECTRO-OPTIC GATING OF THE RADIANT EMISSION FROM LASER-PRODUCED PLASMAS</u>	4.1
4.1	INTRODUCTION	4.1
4.2	THE POCKELS ELECTRO-OPTIC EFFECT	4.2
4.3	EXPERIMENTAL METHODS	4.4
4.4	ALIGNMENT OF THE POCKELS CELL	4.6
4.5	EXPERIMENTAL RESULTS	4.8
4.6	DISCUSSION	4.10
	FIGURES 4.1 - 4.3	
5.	<u>QUANTITATIVE SPECTROCHEMICAL ANALYSIS OF STEEL STANDARDS</u>	5.1
5.1	INTRODUCTION	5.1
5.2	EXPERIMENTAL DETAILS	5.2
5.3	EXPERIMENTAL RESULTS	5.3
5.4	DISCUSSION	5.4
	FIGURES 5.1 - 5.13	
6.	<u>DISCUSSION AND CONCLUSION</u>	6.1
	FIGURE 6.1	
7.	<u>FUTURE DEVELOPMENTS</u>	7.1
	<u>APPENDICES</u>	
A.	<u>TEMPORAL DEVELOPMENT OF LASER-PRODUCED PLASMAS</u>	A.1
A.1	Laser Plasmas (Q-Switched mode)	A.1
A.2	Laser Plasmas (QS) with Auxiliary Excitation	A.2
A.3	Framing Photographs of RO Ruby Laser Plasmas	A.4
A.4	Framing Photographs of Nd-Laser Plasmas with Auxiliary Excitation	A.5
A.5	Discussion	A.6
	FIGURES A.1 - A.4	
B.	<u>RAT'S NEST CALORIMETER</u>	B.1
B.1	Construction	B.1
B.2	Baker's Analysis	B.1
B.3	Rat's Nest in Wheatstone Bridge Configuration	B.3
B.4	Rat's Nest Calibration	B.4
	FIGURES B.1, B.2	

C.	<u>SUMMARY OF STATISTICAL FORMULAE</u>	C.1
	C.1 Basic Definitions	C.1
	C.2 Linear Regression	C.1

D.	<u>TERMINOLOGY, UNITS AND SYMBOLS</u>	D.1
	D.1 Terminology and Units	D.1
	D.2 Symbols	D.2

REFERENCES

E.	PUBLISHED PAPERS	E.1
----	------------------	-----

F.	NOTE ADDED IN PROOF : RECALCULATION OF ELECTRON TEMPERATURES USING REVISED TRANSITION PROBABILITIES.	F.1
----	---------------------------------------------------------------------------------------------------------	-----

REFERENCES

CHAPTER 1

PRINCIPLES OF LASER MICRO-SPECTRAL ANALYSIS

1.1 INTRODUCTION

When high power radiation from a pulsed laser is focused at a solid target, intense local heating causes a rapid rise in the surface temperature. As the boiling point is reached small amounts of target material are evaporated. The evaporated material forms an expanding radiant plume of energetic atoms and ions originating from the target and the atmosphere.

The essence of Laser Micro-Spectral Analysis (LMSA) is the production of a radiant plasma at the surface of a solid target by irradiating it with high power laser radiation. By imaging the radiation emitted from the plasma onto the entrance slit of a spectrograph a line spectrum is obtained which is characteristic of the target material. Qualitative analysis of the constituent elements of an unknown sample can be carried out quickly and simply and the technique is gaining acceptance as a supplement to conventional arc and spark analysis. The problems, however, lie with quantitative analysis.

In LMSA, two modes of laser operation are generally used viz: relaxation oscillator (RO) operation and Q-switched (QS) operation. The character of the laser-target interaction and plasma emission depends on the mode of laser operation and on the laser power density at the target surface.

A laser operating in the RO mode gives a burst of output pulses lasting several hundred microseconds. With a total output energy of about 1J a focused power density of about $10^{10} - 10^{12} \text{ W m}^{-2}$ per spike, is obtained. In this mode of operation a low temperature vapour is produced which is mainly atomic in character. The vapour emission is accompanied by the ejection of molten material. Craters of the order of 100 μm deep, with a similar diameter are left in the material.

Operating a laser in the QS mode usually gives a single output pulse lasting less than 100 ns with a focused power density of about $10^{12} - 10^{15}$ $W m^{-2}$. In this regime, a high temperature plasma is formed which emits radiation from the ionic species as well as from the atomic species. In this mode of operation material is removed from the sample mainly by ablation. The craters tend to be much shallower for QS operation than for RO operation, depths of 2-3 μm being typical with diameters of the order of 100 μm . Due to the high pressures exerted on the target by the expanding vapour, vaporisation in this mode can occur at temperatures well in excess of the normal boiling point of the material at atmospheric pressure.

As can be seen from the above description, the phenomenon of laser-induced vaporisation at a solid target is complex and is usually discussed in terms of the following distinct processes.

- (i) the target heating process, ie the conduction of heat in a solid and the phase transitions occurring in a solid heated to its boiling point,
- (ii) particle emission, ie the ejection of electrons, ions and X-ray emission,
- (iii) plasma production, ie mass removal in the form of a vapour plume from a heated solid, the establishment of a transient plasma and the emission of radiation from the plasma.

These processes, together with the principal experimental techniques used to study them and their main applications are outlined in Fig 1.1. The target-heating process has been studied extensively with regard to the use of lasers for welding and hole-drilling; plasma production processes have been studied for their own sake and are now attracting much attention because of the possibility of laser induced thermo-nuclear fusion. The benefits of this research have extended to other applications involving laser plasmas, in particular, to their use in Laser Micro-Spectral Analysis, the subject of this thesis.

We are concerned with the quantitative aspects of LMSA and consequently we must understand the processes of target heating and plasma production by laser irradiation. The success of quantitative LMSA relies on the spectral line intensities of an element in the plasma being single-valued functions of element concentration within a target. Ultimately, relative spectral line intensities must be correlated with target composition. Thus we must consider the detailed processes by which target material becomes emitting plasma.

In the main body of this thesis we are principally concerned with the spectroscopic aspects of laser-produced plasmas and with the use of these plasmas as excitation sources in spectrochemical analysis. Those items not directly related to the main theme are discussed in the Appendices.

We start our discussion (Chapter 2) of the experimental work in this thesis, with a description of the operation and performance of the main items of apparatus used (laser microanalyser, spectrograph and image converter camera), together with a discussion of photographic materials and film calibration. We studied the temporal and spatial behaviour of laser-produced plasmas using time-integrated and time-resolved spectroscopy (Chapter 3); and from this work we characterised the plasmas produced by the various modes of laser operation in terms of expansion velocity, electron temperature and electron density. We were able to assess the importance of the condition of local thermodynamic equilibrium (LTE) for successful quantitative LMSA. The temporal behaviour of plasmas produced by Q-switched lasers, suggested that the emission spectrum could be simplified (with a resultant improvement in line-to-background ratio) by gating the continuum and multiply-ionised species emission from the atomic species emission. One method of gating the unwanted emission from the atomic

species emission, by using a Pockel's cell as an optical switch, is explored in Chapter 4. In Chapter 5, we discuss the quantitative analysis of steel samples using LMSA and we present working curves of spectral line intensity ratio against Si and Cr concentration. The various modes of laser sampling and excitation are compared in terms of the precision and accuracy of the estimated concentrations of the minor constituents (eg Si and Cr). We conclude the main body of the thesis (Chapter 6) with a discussion of the important points of the preceding chapters and we present general conclusions regarding the use of LMSA for the quantitative analysis of steels. Suggestions are given for the future development and improvement of Laser Micro-Spectral Analysis.

In the Appendices we discuss those items which are important to the main theme of the thesis, but are not directly related to it. An experimental study of the temporal development of the bulk plasma using high speed photography is described in Appendix A. In Appendix B, we discuss the measurement of pulsed laser energy using a Rat's Nest Calorimeter. Some useful statistical formulae are presented in Appendix C. In Appendix D, we outline the terminology and units and present a list and description of all the mathematical symbols used throughout this thesis.

In the remainder of this Chapter (Chapter 1), we outline the basic ideas and concepts required for a study of quantitative LMSA. We first discuss the interaction of high power laser light with solid targets and then present a mathematical model of laser-produced vaporisation and plasma production. The emission from these plasmas is described together with a discussion of local thermal equilibrium and spectral intensity. The standard plasma equilibrium relations are presented before going on to give a brief review of quantitative Laser Micro-Spectral Analysis.

1.2 LASER-PRODUCED VAPORISATION OF SOLID TARGETS

1.2.1 Basic Phenomena

When high power radiation from a pulsed laser is focused onto a solid target, intense local heating causes a rapid rise in surface temperature of the material of the order of 10^{10} K s^{-1} (Ready 1971). Heat is conducted into the interior and a thin layer of molten material forms below the surface and travels through the material to a depth of about $(a t_\ell)^{\frac{1}{2}}$ where a is the thermal diffusivity and t_ℓ is the duration of the laser pulse (Afanasyev et al 1966). The penetration depth is typically $100 \mu\text{m}$ for a $200 \mu\text{s}$ pulse train onto a metal. As the thermal energy increases, a point is reached where the energy required to take a liquid material through the liquid-vapour phase boundary is exceeded. Heat cannot be conducted away from the point of irradiation fast enough to prevent the surface reaching its boiling temperature and evaporation occurs from the surface of the solid. The surface temperature is now governed by the evaporation process and heat conduction is not now an important mechanism of energy balance, but serves only to keep a thin layer of molten material behind the evaporation front. The energy density deposited at the surface of the target by a laser of power density F is $F t_\ell$ and the average energy per unit mass acquired by the thin layer of molten metal is $F t_\ell / \rho_0 (a t_\ell)^{\frac{1}{2}}$, where ρ_0 is the density of the solid target. For evaporation to occur the energy deposited in the thin layer must exceed the latent heat of sublimation of the target (L_s). Thus the threshold power density needed for evaporation to occur is given (Afanasyev et al 1966, Ready 1971 and Krokhin 1972) by

$$F_{\min} = \rho_0 L_s a^{\frac{1}{2}} t_\ell^{-\frac{1}{2}} \quad (\text{Wm}^{-2}) \quad (1.1)$$

For metals, F_{\min} is about $10^{10} - 10^{11} \text{ Wm}^{-2}$.

In the following discussion, we assume that (in one-dimensional co-ordinates) the incident laser beam approaches the target from the $+x$

direction and strikes the surface perpendicularly. The surface of the target corresponds to $x = 0$ and the bulk solid occupies the space $x < 0$. We assume further that the temporal profile of the laser pulse is rectangular, and that the beam strikes the target at a time $t = 0$.

The temperature distribution within a solid target which is heated by laser irradiation can be estimated by solving the differential equation of heat-conduction into a semi-infinite solid (Carslaw and Jaeger 1959). For the one-dimensional case, the time-dependent temperature at the surface of a metal after time t , is given (Ready 1971 p73) by

$$T_0 = \frac{2F_a}{K} \left(\frac{at}{\pi}\right)^{\frac{1}{2}} \quad (1.2)$$

where F_a is the constant absorbed power density at the surface and K is the thermal conductivity. When the power density is greater than F_{min} then evaporation occurs at the surface of the heat conduction layer. The velocity at which the heat conduction layer retreats into the solid approaches a steady state given (Landau 1950) by

$$u = \frac{dx}{dt} = - \frac{F_a}{\rho_0 [L_s + C(T_v - T_a)]} \quad (1.3)$$

The depth vaporised after a time t is given by

$$x_t = \frac{dx}{dt} (t - t_v) \quad (1.4)$$

where the time taken to reach the boiling temperature (T_v) from ambient temperature (T_a) is

$$t_v = \frac{\pi K \rho_0 C}{4 F_a} (T_v - T_a)^2 \quad (1.5)$$

where C is the specific heat capacity. Equations (1.2), (1.4) and (1.5) are useful for estimating the surface temperature, depth vaporised and time taken to reach the boiling temperature when the power density is close to the threshold value.

For an Fe target and an incident power density of $2 \times 10^{10} \text{ Wm}^{-2}$,

the time taken to reach the normal boiling temperature of 3023 K is about 4.2 μs (by eqn 1.5). The steady state velocity of retreat of the heat conduction layer is (by eqn 1.3) 0.3 ms^{-1} and the depth vaporised by a 200 μs laser pulse (by eqn 1.4) is about 63 μm . In practice, the crater depths are larger than those predicted by eqn (1.4) because of the ejection of molten material (Ready 1971).

If the absorbed power density just exceeds F_{min} (eg using RO lasers) surface evaporation proceeds at the normal boiling point of the material, under atmospheric pressure (Ready 1971, Krokhin 1972). The expanding vapour plume exerts a pressure on the liquid layer (known as "ablation pressure") which forces the ejection of molten material from the craters (Scott and Strasheim, 1970). The molten material is ejected with a high kinetic energy (Frontispiece). Craters of, typically, 100 μm deep (Fig 1.2a) with a similar diameter are left in the material (Ready 1971). When using QS lasers, the absorbed power density is much greater than F_{min} and we can now have substantial radiation and ablation pressures exerted on the target. For a laser pulse of power density 10^{14} Wm^{-2} the radiation pressure at the focus of the beam is about 3 atmos, however, the ablation pressure can be as much as $10^4 - 10^5$ times greater than this (Askaryan and Moroz 1963). The ablation pressure is defined by the following relationship (Hughes 1975 p277, Askaryan and Moroz 1963).

$$p_A \approx F_a v_1 / (L_v + \frac{1}{2} v_1^2) \quad (\text{J m}^{-3}) \quad (1.6)$$

where v_1 is the expansion velocity of the vapour and L_v is the latent heat of vaporisation per unit mass. When the expanding vapour plume is established, the ablation pressure exerted on the target prevents further evaporation until the critical temperature is reached where there is no distinction between a superheated liquid and a saturated vapour. At this temperature, substantially above that of the normal boiling point, vaporisation can proceed (Ready 1971). Material is ejected predominantly

as a vapour and shallow craters of about 2 μm deep are formed in the material (Fig 1.2b).

Once the vaporisation process is established at the surface of the solid, the subsequent behaviour of the vapour can be described mathematically by the equations of gas dynamics (Afanasyev et al 1966, Afanasyev and Krokhin 1967, Krokhin 1972). The main details of this model are outlined in the remainder of this section, and we present mathematical relationships for the temperature, density and expansion velocity of laser-produced plasmas.

The equations of gas dynamics for the one-dimensional case are, the continuity equation

$$\frac{\partial \rho}{\partial t} + \frac{\partial}{\partial x} (\rho v) = 0, \quad (1.7)$$

the Euler equation

$$\frac{\partial v}{\partial t} + v \frac{\partial v}{\partial x} + \frac{1}{\rho} \frac{\partial p}{\partial x} = 0, \quad (1.8)$$

and the energy conservation equation

$$\frac{\partial}{\partial t} (\rho \varepsilon + \frac{1}{2} \rho v^2) + \frac{\partial}{\partial x} [\rho v (\varepsilon + \frac{1}{2} v^2 + \frac{p}{\rho})] + \frac{\partial F}{\partial x} = 0, \quad (1.9)$$

where v , ρ , ε and p are, respectively, the velocity, density, internal energy and pressure of the vapour.

For power densities greater than F_{min} , the energy contained in the heat absorbing layer is much less than that absorbed by the target and the gas, and we can neglect the presence of the liquid phase. Thus we can regard the heat absorbing layer as a boundary between the solid and vapour phases. Across the phase boundary, we have

$$\rho_0 u = \rho_1 (u - v_1) \quad (1.10)$$

$$p_0 + \rho_0 u^2 = p_1 + \rho_1 (u - v_1)^2 \quad (1.11)$$

$$F = -\rho_0 u (\varepsilon_1 + v_1^2/2) + p_1 v_1 \quad (1.12)$$

and
$$\varepsilon_1 = [p_1/\rho_1(\gamma-1)] + L_s \quad (1.13)$$

where u is the velocity of the vaporisation boundary (previously given by eqn 1.3), γ is the specific heat ratio, and the subscripts (0) and (1) refer to the solid and vapour phases respectively. The equations (1.10), (1.11) and (1.12) describe, respectively, mass conservation, the pressure exerted on the target due to the evaporation process and the power balance of the system.

We now discuss the solutions of eqns (1.7)-(1.9) with the boundary conditions (eqns 1.10-1.13) for two regimes of vapour production: a low temperature regime ($F \approx 10^{10} - 10^{12} \text{ W m}^{-2}$) in which the vapour is transparent to the laser beam, and a high temperature regime ($F \approx 10^{12} - 10^{15} \text{ W m}^{-2}$) in which significant absorption of the laser beam can occur in the vapour. The treatments of Afanasyev and Krokhin (1967) and Krokhin (1972) are followed closely.

1.2.2 Low Temperature Regime

When F is just above F_{\min} ($\approx 10^{10} - 10^{12} \text{ W m}^{-2}$), we postulate the formation of a low temperature vapour which is mainly atomic in character and is virtually transparent to the incident laser beam. In this case, the term $\partial F/\partial x$ vanishes from eqn (1.9) and the gas expansion is adiabatic. The maximum velocity of the vapour expansion relative to the velocity at which the evaporation front recedes into the target is given by the Chapman-Jouquet condition (eg Krokhin 1972),

$$v_1 - c_1 = u \quad (1.14)$$

and c_1 is the adiabatic sound velocity of the gas at the interface, given by

$$c_1 = (\gamma p_1 / \rho_1)^{\frac{1}{2}} \quad (1.15)$$

Equations (1.7) - (1.9) with $\partial F/\partial x = 0$, and the boundary conditions (1.10) - (1.13) describe a centred rarefaction wave corresponding to an isentropic expansion of gas (Landau and Lifshitz 1959). These

equations (1.7 - 1.9) can be solved for v, ρ and p in terms of a dimensionless variable given by

$$\lambda = L_s^{1/2} x/t. \quad (1.16)$$

Thus, we have, for the vapour density (ρ_1), the velocity (v_1), the pressure (p_1), the temperature (T_1) and the evaporation front velocity (u),

$$\rho_1 = \frac{(\gamma+1)|\lambda_1|}{(\gamma-1)|\lambda_2|\eta} \frac{F}{L_s^{3/2}} \quad (1.17)$$

$$v_1 = \frac{(\gamma-1)|\lambda_2|}{(\gamma+1)} L_s^{1/2} \quad (1.18)$$

$$p_1 = \frac{(\gamma-1)|\lambda_1||\lambda_2|}{\gamma(\gamma+1)\eta} \frac{F}{L_s^{1/2}} \quad (1.19)$$

$$T_1 = \frac{(\gamma-1)^2|\lambda_2|^2}{\gamma(\gamma+1)^2} \frac{A_o L_s}{R_g} \quad (1.20)$$

and
$$u = \lambda_1 L_s^{1/2} \quad (1.21)$$

where $\eta = F/L_s^{3/2} \rho_o$,

A_o is the kg atomic weight and R_g is the general gas constant. The dimensionless variables, λ_1 and λ_2 , can be evaluated numerically using the following approximate expressions (Afanasyev and Krokhin, 1967):

$$\frac{(\gamma-1)^2 \lambda_2^3}{2(\gamma+1)^3} + \frac{(\gamma-1)\lambda_2}{(\gamma+1)^2} \approx \frac{F}{L_s^{3/2} B} \exp \left[\frac{\gamma(\gamma+1)^2}{(\gamma-1)^2 \lambda_2^2} \right] \quad (1.22)$$

and
$$\lambda_1 \approx - \left(\frac{B}{\rho_o} \right) \frac{\lambda_2(\gamma-1)}{(\gamma+1)^2} \exp \left[- \frac{\gamma(\gamma+1)}{(\gamma-1)^2 \lambda_2^2} \right] \quad (1.23)$$

where the constant B (in kg m^{-3}) is obtained from the relationship between the saturation vapour pressure p_{sat} and density,

$$\rho_{\text{sat}} = B \exp (-L_s \rho_{\text{sat}}/p_{\text{sat}}) \quad (1.24)$$

For a laser power density (F) of 10^{11} W m^{-2} incident on an Fe target, we have $B \approx 33 \times 10^6 \text{ kg m}^{-3}$, $L_s = 6.6 \times 10^6 \text{ J kg}^{-1}$ and $\gamma = 5/3$, thus we

get $\lambda_2 = 1.395$ and $\lambda_1 = -6.05 \times 10^{-4}$. Substituting in eqns (1.17) - (1.20) we arrive at,

$$\rho_1 = 2.30 FL_s^{-3/2}, \quad (1.25)$$

$$v_1 = 0.35 L_s^{1/2}, \quad (1.26)$$

$$p_1 = 0.17 FL_s^{-1/2}, \quad (1.27)$$

and
$$T_1 = 0.07 A_o L_s R_g^{-1}. \quad (1.28)$$

Examination of eqns (1.26) and (1.28) show that the velocity and temperature of the vapour depend strongly on the latent heat of sublimation of the target and not on the power density. Typical values of v_1 and T_1 (from eqns 1.26 and 1.28) are 900 ms^{-1} and 3000 K respectively.

1.2.3 High Temperature Regime

For power densities greater than about 10^{12} Wm^{-2} , the vapour pressure is so high that we must consider the effects of absorption of the laser beam within the vapour plume. The temperature of the vapour is high enough to cause significant excitation and ionisation of the evaporated atoms (Krokhin 1972). In this case the strongly absorbing layer is a partially ionised plasma, and the electron density (N_e) approaches the critical electron density which will cause the laser light to be reflected from the plasma surface (Hughes 1975). Laser light will be reflected from a plasma if its frequency is less than the plasma frequency, given by

$$\nu_p \approx 8.9 N_e^{1/2} \quad (\text{Hz}) \quad (1.29)$$

(where N_e is in m^{-3}). The critical electron density for which the plasma frequency and the laser frequency are equal is about

$2.4 \times 10^{27} \text{ m}^{-3}$ for ruby laser light. The temperature of the vapour increases by free-free absorption (inverse bremsstrahlung) of the laser radiation. Free-free absorption occurs when a photon is

absorbed by an electron in the presence of the field of a heavy particle (atom or ion). The electron is raised to a higher energy state in the continuum available to it.

We now postulate the existence of a self-regulating plasma system, in which the (dimensionless) optical depth of the plasma is equal to one at all times (Krokhin 1965, Caruso et al 1966). For a homogeneous layer, L, of the plasma, the optical depth is defined (eg Lochte-Holtgreven 1968 p136) by

$$d_{\nu} = a_{\nu} L. \quad (1.30)$$

The absorption coefficient a_{ν} (in m^{-1}) of a laser beam of frequency ν , in a plasma of effective charge z , is given (eg Hughes 1975 p44) as

$$a_{\nu} = \frac{e^6 N_e N_i G z^2}{6\sqrt{3} (2\pi)^{5/2} h c m_e^{3/2} \nu^3 \epsilon_0^3 (kT)^{1/2}} \left[1 - \exp\left(-\frac{h\nu}{kT}\right) \right] \quad (1.31)$$

where e is the electron charge, m_e is its mass, c is the velocity of light, N_i is the ion density, h is Planck's constant, k is Boltzmann's constant, ϵ_0 is the permittivity of free space and G is the Gaunt factor (~ 1).

In the self-regulating system, if $d_{\nu} \ll 1$, the plasma is transparent to the incoming radiation and most of the laser power goes into evaporating the target material, giving an increase in density of the plasma. If $d_{\nu} \gg 1$, the plasma is very dense and will absorb most of the radiation, resulting in plasma heating and expansion, which in turn reduces the optical depth, and so on.

Returning to the gas dynamic equations (1.7-1.9), we now have for the absorption term

$$\frac{\partial F}{\partial x} = -a_{\nu} F. \quad (1.32)$$

If the solid is restricted to $x < 0$, we have

$$F(x) = F_a \exp\left[-\int_x^{\infty} a_{\nu}(x) dx\right] \quad (1.32)$$

where F_a is the absorbed power density. Following the method of Krokhin (1972) based on similarity relations, we can find approximate solutions of

equations (1.7-1.9) together with the boundary equations (1.10-1.13)

For a fully-ionised plasma with the electron temperature (T_e) equal to the ion temperature (T_i) and assuming that the plasma frequency is always less than the laser frequency and that L_s is much less than the energy per unit mass supplied to the target, we have

$$\rho_1 \approx 0.46 (a_o t)^{-3/8} F_a^{1/4} \quad (1.34)$$

$$v_1 \approx 0.77 (a_o t)^{1/8} F_a^{1/4} \quad (1.35)$$

$$p_1 \approx 0.34 (a_o t)^{-1/8} F_a^{3/4} \quad (1.36)$$

$$T_1 \approx 0.74 (a_o t)^{1/4} F_a^{1/2} A_o R_g^{-1} \quad (1.37)$$

For the mass of target evaporated per unit area and converted into plasma, we have

$$M \approx 0.47 a_o^{-1/4} t^{3/4} F_a^{1/2} \quad (1.38)$$

The constant a_o has the dimensions of $m^8 kg^{-2} s^{-3}$, and is related to a_v by the following expression,

$$a_v = a_o \rho_1^{7/2} p_1^{-3/2} \quad (1.39)$$

Allowing for the finite rise time of the laser pulse (instead of assuming a square pulse), the numerical constants in eqns(1.34)-(1.38) alter. Thus, if we assume that the rise time is proportional to t^2 , then the constants become 0.63, 0.73, 0.36, 0.55 and 0.26 respectively.

Expressions (1.34)-(1.38) can be written in terms of the initial expansion velocity (v_1) which can be determined experimentally.

Using the " t^2 " numerical constants for a laser pulse with a finite rise time, we have

$$\rho_1 = 0.25 F_a v_1^{-3} \quad (1.40)$$

$$p_1 = 0.26 F_a v_1^{-1} \quad (1.41)$$

$$T_1 = 1.03 v_1^2 A_o R_g^{-1} \quad (1.42)$$

$$\text{and } M = 0.14 t F_a v_1^{-2} \quad (1.43)$$

Vapour expansion velocities in excess of 10^3 ms^{-1} are obtained (Ready 1971)

giving a vapour temperature (by eqn 1.42) of 7000 K. Examination of eqns (1.37) and (1.38) show that the temperature and mass of the plasma are proportional to $t^{1/4}$ and $t^{3/4}$ respectively, so, consequently most of the laser power goes into vaporising the target.

Expressions which differ from eqns (1.34)-(1.38), only by the constants, have been obtained by Caruso and Gratton (1968) using dimensional analysis.

1.3 PLASMA EMISSION AND SPECTROCHEMICAL ANALYSIS

Spectroscopic analysis of laser plasmas shows a strong continuum emission occurring close to the target surface, with strongly broadened lines from the atomic and ionic species superimposed upon it. The line emission extends beyond the continuum into the higher regions of the plume (Scott and Strasheim 1970, Batanov et al 1973).

In the RO mode, radiation is emitted from the plasma in pulses which coincide with the relaxation oscillator spikes of the laser pulse. The continuum emission only occurs during the individual laser spikes, whereas decaying line emission is observed between spikes (Archbold et al 1964, Scott and Strasheim 1970). This behaviour implies rapid heating and cooling of the vapour plume which coincides with each laser spike. Resonance lines are strongly self-reversed (Scott and Strasheim 1970).

The continuum emitted from QS mode plasmas is more intense than that for the RO mode. Lines from doubly and triply ionised states are often observed (Archbold et al 1964, Scott and Strasheim 1970). The continuum is emitted in a short pulse after the peak of the laser pulse. Spectral lines are emitted from the plasma in order of decreasing ionisation state. Lines from multiply-ionised species coincide with the continuum emission,

whereas lines from the singly-ionised and neutral species peak in intensity at progressively later times in the plasma life (Boland et al 1968). The singly-ionised and neutral species are injected into the plasma at greater distances from the target and with lower kinetic energies than are the multiply-ionised species. Production of lower-ionic states by recombination of free electrons with highly-ionised species is not thought to be a dominant mechanism (Boland et al 1968, Piepmeier and Malmstadt 1969). Again extreme self-reversal of the resonance lines can occur by re-absorption of photons by the neutral species in the cooler outer regions of the plume (Rasberry et al 1967, Scott and Strasheim 1970).

In the early part of the plasma lifetime, when the electron density is high the continuum emission will be predominantly black-body radiation. As the plasma expands and becomes transparent to its own radiation (when the optical thickness of the plasma is less than unity) the plasma emission will be predominantly bremsstrahlung (Archbold et al 1964, De Michelis 1970, Hughes 1975). Bremsstrahlung emission (free-free radiation) is the inverse of free-free absorption (Sec 1.2.3) and occurs when free electrons lose energy by collisions with heavy particles and emit photons, resulting in a continuous spectrum. In a hot plasma, collisions between electrons and ions dominate the energy transfer processes, although in a partially ionised plasma, electron-atom collisions are important.

1.3.1 Local Thermodynamic Equilibrium (LTE)

To quantitatively determine the concentration of an element in a plasma plume, the plasma must exist in a condition of local thermodynamic equilibrium (LTE). The state of LTE is characterised by the following conditions (Griem 1964):

(i) the velocities of the free electrons and free heavy particles (atoms and ions) follow a Maxwell distribution at temperatures of T_e (electron) and

T (gas) respectively;

(ii) for each type of particle, the relative populations of the bound levels follow a Boltzmann distribution (eqn 1.47);

(iii) the state of ionisation of each species is described by the Saha equation (eqn 1.52).

The LTE state is distinguished from complete thermodynamic equilibrium (TE) by not possessing a black body radiation field.

For LTE to occur, electron collisions must dominate the other energy transfer processes (viz radiative decay and recombination) establishing a Boltzmann distribution among the bound energy levels. This condition is particularly critical for the lower-lying levels, because their radiative lifetimes tend to be short and their collisional cross-sections are small (Griem 1964). In a partially ionised vapour, electron collisions will be the dominant mechanism of energy transfer because of their high velocities and long-range coulomb interaction. The populations of the resonance levels of the major constituents of a plasma are nearly always established by radiative processes, and self-absorption can occur in the outer regions of the plasma. Often, in quantitative LMSA of trace elements, the resonance lines are the only lines which are strong enough to be used for intensity measurements. However, the small concentrations of trace elements present in the plasma ensure that electron collisions dominate the radiative processes, and LTE can be established between the resonance levels.

For less than 10% departure from LTE, the rate of energy transfer by electron collisions must be about ten times faster than the radiative decay rate. This leads to the following criterion for the establishment of LTE in a plasma (McWhirter 1965) viz,

$$N_e \geq 1.7 \times 10^{20} (kT_e)^{\frac{1}{2}} (E_p - E_q)^3 \quad (\text{m}^{-3}) \quad (1.44)$$

where kT_e is the electron temperature (in eV) and $(E_p - E_q)$ is the largest energy gap (in eV) for which eqn(1.44) is least likely to be satisfied, ie the resonance levels.

In the QS mode, electron densities $> 10^{23} \text{ m}^{-3}$ and electron temperatures $> 1\text{eV}$ (Ready 1971) ensure that LTE conditions apply to most excited atomic states in the vapour plume (for measurements of N_e and T_e , see Chapter 3). By contrast, the lower temperatures and densities which frequently occur in the vapour produced by RO mode lasers can prevent reliable quantitative analysis. To ensure favourable plasma conditions, when operating in either the RO or the QS mode, a pair of carbon electrodes are often positioned above the target to intercept the rising vapour plume. The electrodes are electrically biased to just below the atmospheric breakdown potential. The partially ionised vapour plume initiates a spark discharge causing further excitation (Rasberry et al 1967). Use of auxiliary spark excitation gives spectra which are sharper and more intense than those obtained with either laser mode on its own. The likelihood of self-reversal of resonance lines is also reduced. However, the molecular bands of cyanogen appear on the spectrum.

1.3.2 Spectral Intensity and Equilibrium Relationships

In this section we discuss the term spectral intensity as it is applied to plasmas and we present the basic intensity relationships used in plasma spectroscopy (McWhirter 1965, Cooper 1966, Griem 1964 and Lochte-Holtgreven 1968).

We assume that the plasma produced by vaporisation of a small area of a target on irradiation by a high power pulsed laser, is a pure metallic vapour (ie we neglect atmospheric gases). We also assume that the vapour

exists in a state of local thermodynamic equilibrium (LTE) and that the plume is optically thin (ie radiation is emitted from the plume without any re-absorption).

The radiance of a spectral line λ_{pq} emitted from a source due to spontaneous transitions from energy level p to energy level q, is given by (McWhirter, 1965):

$$I_{pq} = \frac{1}{4\pi} \int_0^L \frac{hc}{\lambda_{pq}} A_{pq} N_p d\ell \quad (\text{Jm}^{-2} \text{s}^{-1} \text{sr}^{-1}) \quad (1.45)$$

where A_{pq} is the probability of a spontaneous transition between levels p and q (Einstein A), N_p is the number of particles per unit volume of a source in level p, h is Planck's constant and c is the velocity of light.

Integration is over the plasma depth ℓ , measured along the line of sight of the spectrograph. Thus for a homogeneous layer of source of depth L we have

$$I_{pq} = \frac{hc}{4\pi} \frac{A_{pq}}{\lambda_{pq}} N_p L \quad (1.46)$$

The quantity I_{pq} is usually called the intensity of a spectral line λ_{pq} , but we will use the term "radiance" throughout this thesis.

In the LTE approximation the populations of the energy levels have a Boltzmann distribution and N_p is given by

$$N_p = N \frac{g_p}{Z} \exp\left(-\frac{E_p}{kT}\right) \quad (1.47)$$

where Z, the partition function is given by

$$Z = \sum_p g_p \exp\left(-\frac{E_p}{kT}\right) \quad (1.48)$$

and N is total number of particles per unit volume, g_p is the statistical weight of level p, E_p is the excitation energy of the upper level p and kT is the vapour temperature in electron-volts (eV). Equation (1.46)

can now be written as

$$I_{pq} = \frac{hc}{4\pi} \frac{A_{pq} g_p}{\lambda_{pq} Z} LN \exp\left(-\frac{E_p}{kT}\right) \quad (1.49)$$

From eqn (1.49) we can write the intensity ratio between two spectral lines λ_{pq} and λ_{mn} of the same element and ionisation state as

$$\frac{I_{pq}}{I_{mn}} = \frac{A_{pq} \lambda_{mn} g_p}{A_{mn} \lambda_{pq} g_m} \exp \left[- \frac{(E_p - E_m)}{kT} \right] \quad (1.50)$$

Consider now two spectral lines which are from the same element but belong to two consecutive ionisation states. From eqn (1.46) we can write the intensity ratio between a spectral line λ_{mn}^z of one ionisation state and a line λ_{pq}^{z+1} of the next higher ionisation state as

$$\frac{I_{pq}^{z+1}}{I_{mn}^z} = \frac{A_{pq}^{z+1} \lambda_{mn}^z N_p^{z+1}}{A_{mn}^z \lambda_{pq}^{z+1} N_m^z} \quad (1.51)$$

The relationship between the population densities of two energy levels in consecutive ionisation states is given by the Saha equation as

$$\frac{N_e N_p^{z+1}}{N_m^z} = 2 \frac{g_p^{z+1}}{g_m^z} \left[\frac{2\pi m_e kT}{h^2} \right]^{3/2} \exp \left[- \frac{(E_p^{z+1} - E_m^z)}{kT} \right] \quad (1.52)$$

where N_e is the electron density, N_p^{z+1} is the population density of level p of the upper ionisation state (z+1), N_m^z is the population density of level m of the lower ionisation state (z), E_p^{z+1} is the energy required to ionise a particle in level n of the lower ionisation species and m_e is the electron mass. Substituting eqn (1.52) into eqn (1.51), we arrive at

$$\frac{I_{pq}^{z+1}}{I_m^z} = \frac{2 A_{pq}^{z+1} \lambda_{mn}^z g_p^{z+1}}{N_e A_{mn}^z \lambda_{pq}^{z+1} g_m^z} \left[\frac{2\pi m_e kT}{h^2} \right]^{3/2} \exp \left[- \frac{(E_p^{z+1} - E_m^z)}{kT} \right] \quad (1.53)$$

1.3.3 Electron Temperature and Electron Density

We have seen (sec 1.3.1) that in a plasma in LTE, the energy transfer processes are dominated by electron collisions. Since electrons are the

principal energy carriers, we can replace the gas temperature, T , in the preceding equilibrium relations by the electron temperature, T_e .

The equilibrium relationships presented above can be manipulated into forms suitable for determining the basic plasma parameters of electron temperature and electron density. Equation (1.50) can be rewritten as

$$-\frac{(E_p - E_m)}{kT_e} = \ln \left[\frac{I_{pq} A_{mn} \lambda_{pq} g_m}{I_{mn} A_{pq} \lambda_{mn} g_p} \right] \quad (1.54)$$

Thus a plot of $(E_p - E_m)$ against the right hand side of equation (1.54) should yield a straight line of slope $(-1/kT_e)$ passing through the origin. The electron temperature can be determined from the slope.

If the intensity ratio is known between two lines in consecutive ionisation states together with the electron temperature then equation (1.53) can be used to determine the electron density. Electron temperatures estimated using equation (1.50) are somewhat inaccurate if the term $(E_p - E_m)$ is small and the method can be rather insensitive (Griem 1964). Equation (1.53) is better but requires a knowledge of the electron density. The use of this equation also requires that both the ionic and atomic levels are in a condition of LTE (Cooper 1966).

1.3.4 Photographically Measured Spectral Intensities

The radiance of a spectral line emitted from a source, due to spontaneous transitions between two energy levels is given by eqn (1.45). In practice the radiance is usually estimated from a photographic or photometric record of the spectral line. When the photographic medium is used the optical density (amount of blackening) of a spectral line is measured using a microphotometer. The optical density (D) is related to the exposure (Q) of the emulsion by means of a characteristic curve (Sec 2.3.2). The characteristic curve is linear only over a limited range of Q , and in

this region we can write

$$D = \gamma \log Q \quad (1.55)$$

where γ is the slope of the linear portion of the curve.

When a light source is imaged on a spectrograph, the irradiance, at the film, of a spectral line λ_{pq} emitted from the source is given (Betz and Johnson, 1971) by

$$H_{pq} = \tau \omega I_{pq} \quad (\text{W m}^{-2}) \quad (1.56)$$

where τ is a factor which accounts for light losses incurred in the detection system, and ω is the solid angle subtended at the film by the camera lens of the spectrograph. The exposure, Q_{pq} , of a photographic emulsion is defined by integrating the irradiance of the line with respect to time,

$$Q_{pq} = \int H_{pq} dt \quad (\text{J m}^{-2}) \quad (1.57)$$

$$= \int \tau \omega I_{pq} dt \quad (1.58)$$

In conventional spectrochemical analysis, it is assumed that all spectral lines are exposed for the same length of time Δt and that H_{pq} is not a function of time. We can write eqn (1.57) as

$$Q_{pq} = H_{pq} \Delta t \quad (1.59)$$

and the exposure ratio between two lines λ_{pq} and λ_{mn} is

$$\frac{Q_{pq}}{Q_{mn}} = \frac{H_{pq}}{H_{mn}} = \frac{I_{pq}}{I_{mn}} \quad (1.60)$$

The exposure ratio, and hence radiance ratio, is estimated from measurements of the optical density of the lines. When the radiance ratio is estimated from photographic plate measurements, we will refer to this as the "photographic intensity ratio" and define it as follows:

$$\frac{J_{pq}}{J_{mn}} \equiv \frac{I_{pq}}{I_{mn}} \quad (1.61)$$

Thus the measured ratio (J_{pq}/J_{mn}) is used in any expression involving

the radiance ratio.

1.3.5 Spectrochemical Analysis

The absolute radiance of a spectral line, λ_{pq} , emitted from a homogeneous layer of source has been given by eqn (1.45) in terms of the number density of atoms (or ions) in the plasma. However, in spectrochemical analysis, a radiance ratio of a minor to a major constituent is normally used, to reduce errors due to source fluctuations and detector calibration. For a spectral line λ_{pq} , from the analysis element A (normally a minor constituent) and a line λ_{mn} from the reference element R (major constituent), emitted from the same region of source, we have, from eqn (1.49):

$$\frac{I_{pq}}{I_{mn}} = \frac{A_{pq} g_p \lambda_{mn} Z(R) N(A)}{A_{mn} g_m \lambda_{pq} Z(A) N(R)} \exp \left[- \frac{(E_p - E_m)}{kT} \right] \quad (1.62)$$

where $N(A)$ and $N(R)$ are the number densities of one species of elements A and R respectively and $Z(A)$ and $Z(R)$ are the respective partition functions. Taking logs of both sides, we have

$$\log \frac{I_{pq}}{I_{mn}} = \log \frac{N(A)}{N(R)} + \log \left[\frac{A_{pq} g_p \lambda_{mn} Z(A)}{A_{mn} g_m \lambda_{pq} Z(R)} \right] - 0.43 \frac{(E_p - E_m)}{kT} \quad (1.63)$$

Thus, using photographically (or photometrically) measured intensities, we can plot the intensity ratio against the known concentration ratio of standard samples to give a straight line of the form

$$\log \frac{J_{pq}(A)}{J_{mn}(R)} = \log \frac{N(A)}{N(R)} + K_0 \quad (1.64)$$

where K_0 is a constant for a given pair of spectral lines. This is known as the "working curve", from which we can estimate the concentration of a minor constituent from a measured intensity ratio. In the ideal case, we see (from eqn 1.64) that the working curve should have a gradient of unity. A unity gradient implies that the ratio of spectral intensities in the plume

is a faithful representation of the element concentration in the target. Departures from unity indicate that one target species is evaporated into the plume in preference to another (ie selective volatilisation), or that the major constituent spectral line is being self-absorbed. The effects of self-absorption can also introduce a departure from linearity in the working curve, at higher concentration ranges (Mika and Torok 1974).

The analysis and reference lines are chosen so that $\log (J_{pq}(A)/J_{mn}(R))$ is affected only by composition and not by excitation conditions. Thus lines with similar excitation potentials and from the same region of plume should be chosen and, if possible, resonance lines should be avoided (see Sec 1.3.1). Also, the lines should be from the same wavelength region (Ahrens and Taylor 1961).

1.4 LASER MICRO-SPECTRAL ANALYSIS

The technique of LMSA offers a number of advantages over conventional arc and spark analysis. Since the sampling region is about 100 μm diameter by a similar depth, damage to target samples is minimal and true local analysis of target sites is possible. Optical rather than electrical power is used in target vaporisation, thus dielectric samples can be easily analysed and no special preparation of samples is needed before analysis. Speed and simplicity of operation are the main advantages of this technique (Rasberry et al 1967). Detection limits are at least as good as those obtained in arc and spark analysis. Relative limits of 10 ppm are not unusual and absolute limits as low as 10 pg have been obtained (Moenke and Moenke 1973).

Quantitative LMSA involves relating the spectral line intensity of an element to the concentration of that element in the sample. A spectral line intensity is actually a measure of the composition of the vapour plume,

which is in turn assumed to be a true replica of the sample composition. Whether or not this is true depends on the combined effects of the physical and chemical properties of the target on the plume composition. These effects are known as "matrix effects" (see Ahrens and Taylor 1961 and Boumans 1966). Thus the process of target sampling is of great importance in LMSA.

When accompanied by an auxiliary spark discharge, LMSA is a two-step process in which the laser is used to sample the target and the spark discharge excites the vapour. Each step can be separately optimised to yield the best possible spectra and obtain the greatest sensitivity. Care must be taken in positioning the electrodes and selecting the discharge parameters to ensure that the spark excites the vapour only and has no influence on target vaporisation (Yamane and Matsushita 1972). The craters formed in materials on laser irradiation have widely varying shapes and dimensions depending on the laser power density and the physical properties of the material (Nohe and Morton 1970, Ready 1971) and we would expect this to show a similar spread in spectral intensities.

In an analysis of the weight of Copper vaporised from a number of metallic matrices, Morton et al (1973) obtained a linear relationship between the spectral intensity ratio of Cu/matrix element and predicted the weight of Cu from volume measurements. This indicates that, at least for this set of alloys, no significant matrix effect is apparent. Consequently the data from a number of different alloys can be plotted together and predictions made of the vaporised weight of minor constituents for any crater size.

Important evidence for the existence of matrix effects in LMSA came from Baldwin (1970). The vapour ejected from a Zn/Cu foil was collected on a piece of polyester film placed above the target. Examination of the vapour deposit by X-ray fluorescence revealed that the Zn/Cu weight ratio of the

vapour could be as much as 30% greater than that of the target. The Zn/Cu weight ratio of the vapour was independent of the laser energy used and of the number of spikes in the laser output, but was still a linear increasing function of the weight ratio of the target. This evidence suggested that selective volatilisation occurs in the laser sampling process. An early study of matrix effects in LMSA (Cerrai and Trucco 1968) showed that line intensity also depends on factors other than target composition; in particular, it was shown that the line intensity is influenced by the grain size and metallurgical state of the sample.

Although it appears difficult to correlate spectral intensity directly with target composition, it is still possible to derive sample concentrations via the construction of a working curve. This method of approach has been adopted by some authors to compare the results obtained using the various methods of excitation in LMSA (Rasberry et al 1967, Scott and Strasheim 1970, Schroth 1972). Schroth (1972) showed that the slope of the working curves was nearer to unity and the standard deviation of the plotted results were smaller for the spark-assisted QS mode than for the spark assisted RO mode. However, we should note that Schroth operated the laser in the semi-QS mode (4 to 12 spikes), not in the single-spike mode. Scott and Strasheim (1970) used a ruby laser in the RO, QS and semi-QS modes to analyse ten Al standards for Cu content. The gradients they obtained for all the working curves were less than unity. The gradient of the RO mode curve was closest to unity (0.4) and the QS curve gradient was furthest from unity (0.25)ⁿ. However, when the curves were used to predict the concentration of the constituents, the variation coefficient of the estimated concentration was smallest for the QS mode curve. The gradient of the QS curves increased to about 0.4 when the effect of the background continuum was removed from the line emission by gating the photomultipliers used to detect the signal.

1.5 SUMMARY

Laser Micro-Spectral Analysis involves a series of complex phenomena from the process of target heating to the establishment of a radiant plasma above the target. These processes must be thoroughly understood before laser-produced plasmas can be used successfully as excitation sources in quantitative spectrochemical analysis. The laser-target interaction can be divided into two regimes depending on power density and mode of laser operation. For multi-spike lasers of low power density ($< 10^{12} \text{ W m}^{-2}$) a low temperature vapour is formed which is principally atomic in character. Much of the material is removed in liquid form leaving deep, wide craters in the target. For single-spike lasers of high power density ($> 10^{12} \text{ W m}^{-2}$), a high temperature plasma ($> 1 \text{ eV}$) is formed composed of highly ionised and atomic species. Material is removed principally as a vapour and shallow craters are left in the target. To be useful as excitation sources laser-produced plasmas must exist in a state of LTE, in which case, the usual concepts and relationships of plasma spectroscopy can be applied.

With Laser Microanalysis, working curves of log spectral intensity ratio against log concentration can be used to determine the concentration of minor constituents in a wide variety of matrices from metal alloys to biological samples. However it is not clear which of the operational modes of LMSA gives the best accuracy in estimating the concentration of minor constituents, if indeed any method is universally better. For instance QS operation is better for analysing glasses and transparent crystals (Moenke and Moenke 1973), and for locally analysing shallow inclusions, whereas the RO mode is better if large quantities of material are to be sampled. Whilst there appears to be some uncertainty as to the significance of matrix effects in LMSA, the effects do seem to be less troublesome than in conventional arc and spark analysis.

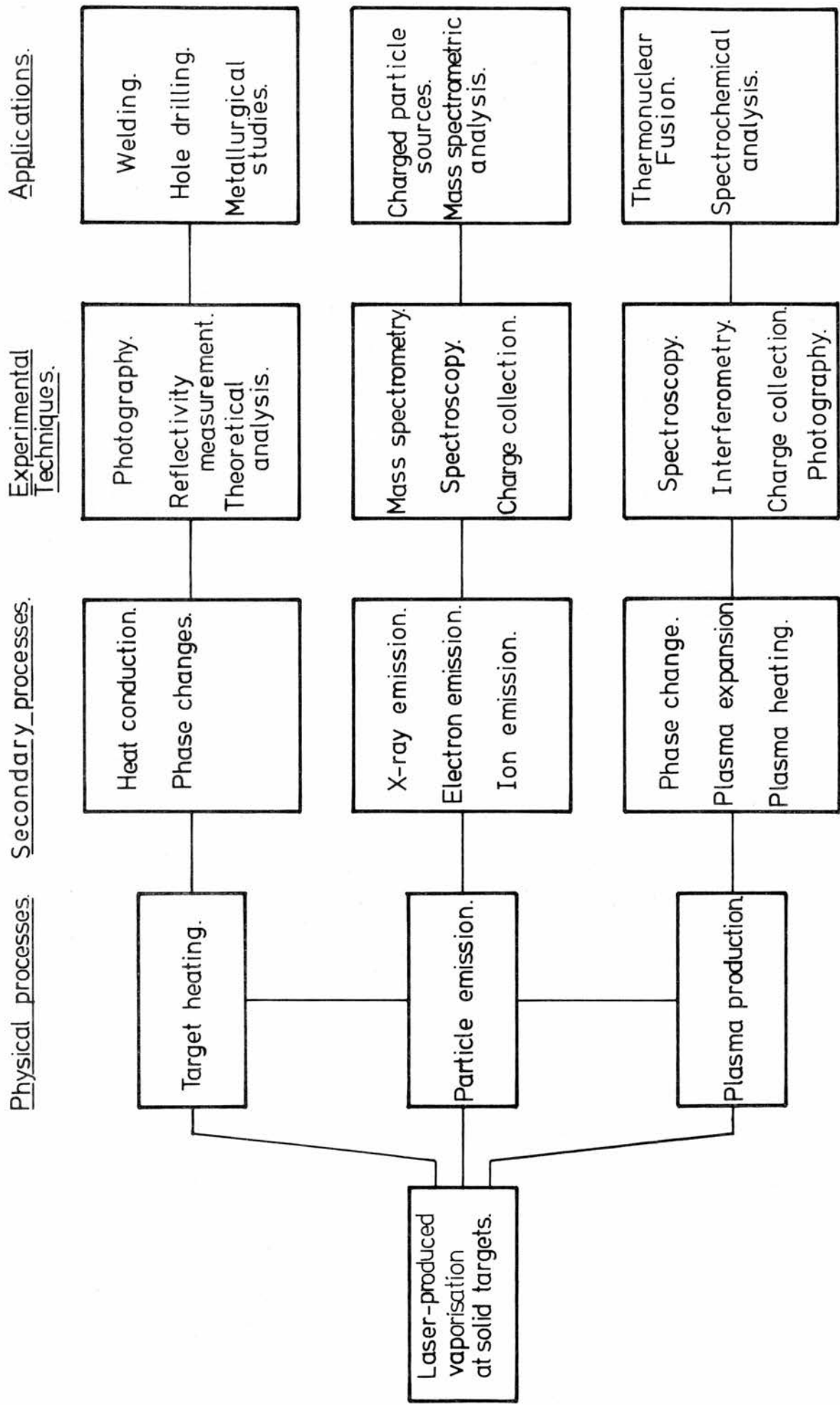
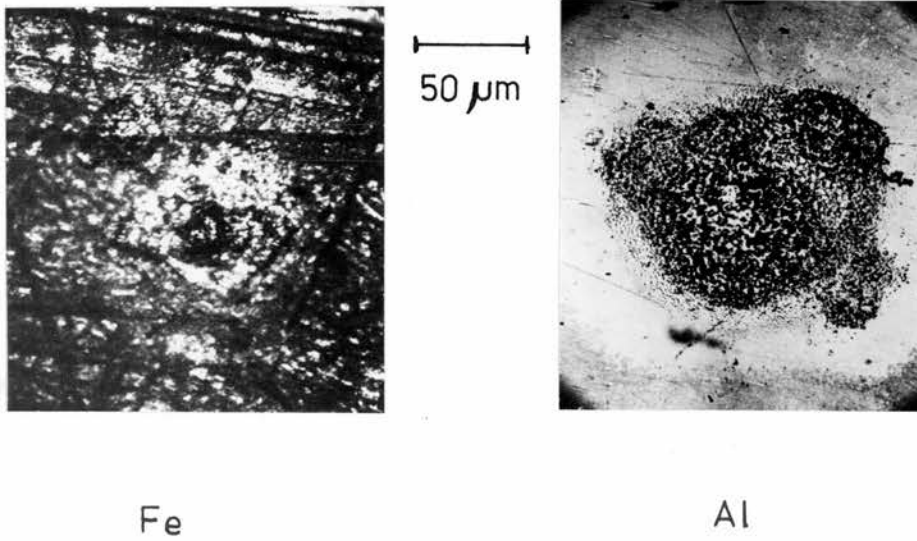


FIG.1.1 BLOCK DIAGRAM OF PHYSICAL PROCESSES IN LASER-PRODUCED VAPORISATION.



(a) Electron micrograph of crater produced in steel by an RO mode laser.



(b) Photomicrographs of craters produced in Fe & Al by a QS mode laser.

FIG 1.2: CRATERS PRODUCED IN METAL TARGETS

CHAPTER 2

EXPERIMENTAL TECHNIQUES AND INSTRUMENTATION

2.1 THE LASER MICROANALYSER TYPE LMA-1

For the work in this thesis we used a commercial Laser Microanalyser (Carl Zeiss, Jena Type LMA-1). The LMA-1 (Fig 2.1) consists of a pulsed laser to sample the target and excite the vapour plume and a microscope to select and examine the sampling area of the target (Fig 2.2). The laser radiation is focused onto the target by the objective lens of the microscope. Excitation of the vapour plume can be enhanced by applying a spark discharge which is formed between a pair of electrodes, across the plume.

2.1.1 The Laser

The active medium of the laser in the LMA-1 can be either a cylindrical rod of Nd^{3+} -glass or ruby. The energy levels of these crystals are characterised by having wide absorption bands and one or more narrow fluorescent emission lines (eg Chang 1969, Chapter 8). An optical cavity is formed by placing the laser rod longitudinally between a totally reflecting prism and a partially reflecting ($\approx 10\%$ R) mirror. A population inversion is established between the energy levels of the fluorescent emission by optically pumping the rod with intense broadband radiation from a pulsed flashtube. When the optical gain of the cavity due to the population inversion exceeds the cavity losses, laser action occurs. A population inversion is created and destroyed many times during the flashtube pulse giving a train of randomly varying output pulses (spikes) over about 200 μs . This mode of operation is variously known as "relaxation oscillator (RO)" "free-running", "normal" or "burst" operation.

The LMA-1 can also be operated in the Q-switched (QS) mode. By placing an optical shutter between the ruby resonator and the reflecting prism, the "Q" of the cavity is reduced and the threshold for laser action increased. Thus, if the cavity is maintained in the low Q state as the resonator is being

pumped, laser oscillation is prevented while the population inversion is increased to a value well above its normal threshold. Suddenly opening the shutter switches the cavity from low Q to high Q and releases the stored energy as one short energetic pulse of light (eg Chang 1969, Chapter 8). This mode of operation is also known as "giant pulse" or "Q-spoiled". Q-switching is achieved on the LMA-1 using a bleachable dye. A transparent cell containing the dye (a solution of cryptocyanine and methanol) is positioned between the ruby and the prism (Fig 2.3) and acts as an optical shutter. The transmission of the dye is a function of wavelength, intensity and duration of exposure to laser radiation. The gain of the cavity and hence the number of spikes in the laser output can be controlled by varying the dye concentration. The dye cell of the LMA-1 is divided into six sections of increasing dye concentration, each of which can be independently rotated into the optical path, thus giving a range of operation from multispike to single spike.

The flashtube radiation is focused into the laser rod by positioning the flashtube and the rod at the respective foci of an elliptical reflector. The cavity configuration is different for each of the two rods and these are shown in Fig 2.4. The Nd-glass rod is a one-piece cavity resonator (110 mm long by 9.5 mm diameter) with a totally reflecting prism at one end and a plane coated surface at the other (Fig 2.4b). It can only be operated in the R0 mode. The ruby rod (100 mm x 8 mm) has polished end surfaces, flat to within $1/5$ of wavelength and parallel to within 15 sec of arc. A resonant cavity is formed by placing a totally reflecting prism and a partially reflecting mirror at the respective ends of the rod (Fig 2.4a). The ruby rod can be operated in either the R0 or QS mode using the Q-switch described above. The xenon flashtube can be operated up to a maximum charging voltage of 2.0 kV with three pre-set capacitances of 254, 381 and 508 μ F. The maximum charging energy is 1016 J.

2.1.2 Laser Output Parameters

The characteristics of plasma production and development at a target depend on the parameters of the incident laser radiation. Thus a knowledge of the energy, power and temporal structure of the laser output is required. We measured the output energy for each mode of laser operation on the LMA-1 with a rat's nest calorimeter in a Wheatstone bridge configuration. A description of the calorimeter and its operation is given in Appendix B. The temporal profile of the laser output was monitored on a cathode ray oscilloscope (CRO) by reflecting the unfocused beam from a piece of black-board chalk onto a fast photodiode. The photodiode (EG & G, SD-100) had an IR response and was suitable for use with both the Nd-glass and ruby radiations.

The output energy of the Nd-glass laser as a function of flashtube charging parameters is shown in Fig 2.5. The maximum output energy of 240 mJ corresponds to a flashtube charging energy of 1016 J. The relative output energy was measured at 5 min intervals over a period of 45 min, with the laser air cooled in between shots (Fig 2.5). The energy decreases steadily over the first four or five shots before steadying at an average of $0.91 \text{ max } \pm 6\%$. The output pulse consists of several hundred relaxation spikes. The total pulse duration was about $380 \mu\text{s}$ for a flashtube energy of 1016 J.

pulse duration gives an average power of 630 W, with a peak power per spike of approximately 8 kW.

For a flashtube energy of 1016 J the output energy of the ruby laser was about 125 mJ in the RO mode and about 80 mJ in the QS mode. The relative energy of the QS mode measured over a 60 min period at 5 min intervals is shown in Fig 2.6. After the first shot the energy falls to an average relative energy of $0.61 \text{ max } \pm 7\%$. The temporal profile of the RO pulse consists of a train of 30-50 spikes over a duration of $200 \mu\text{s}$ (Fig 2.6). Thus for an energy of 125 mJ we have an average power of 625W, with a peak power per spike of 2-3 kW. In QS operation a single output spike is obtained

of 50 ns FWHM (Fig 2.6). This corresponds to a peak power of 1.6 MW for an output energy of 80 mJ.

The power density at the target surface is calculated from an estimate of the diameter to which the output beam can be focused. If a beam of divergence half-angle θ is focused to a spot by a lens of focal length f , the diffraction limited spot diameter (eg Longhurst 1967, p 221) is given by

$$d = 2f\theta \quad (2.1)$$

The diffraction limited divergence θ of a beam of wavelength λ , traversing an aperture of diameter D is usually given by

$$\theta = \frac{1.22\lambda}{D} \quad (2.2)$$

Equation (2.2) can only be applied to lasers oscillating in a single transverse cavity mode. Most solid state lasers oscillate in a number of transverse modes and the observed beam divergence is larger than that given by eqn (2.2). Thus spot diameters are estimated (from eqn 2.1) using experimentally observed beam divergences.

The laser beam is focused onto the target using one of two microscope objective lenses supplied with the LMA-1, viz:

- (i) a plane field, catadioptric lens X40/0.5 with $f = 6.3$ mm and a working distance of 15.7 mm
- (ii) a plane field achromat X16/0.2 with $f = 15.6$ mm and a working distance of 18 mm.

A beam divergence of 5 mrad is typical for both the Nd-glass and ruby lasers. Thus focused spot diameters of 150 μm are obtained using the 15.6 mm and 6.3 mm lenses respectively. Typical power densities using the 15.6 mm lens are $1.8 \times 10^{11} \text{ W m}^{-2}$ per spike for RO mode operation and $9 \times 10^{13} \text{ W m}^{-2}$ for QS mode operation.

The laser output parameters are summarised in Table 1.1.

Table 1.1

	<u>Relaxation oscillation (RO)</u>		<u>Q-switched (QS)</u>
	Nd-glass	Ruby	Ruby
Resonator rod			Ruby
Pulse-duration	380 μ s	200 μ s	50 ns (FWHM)
Number of spikes	200-300	30-50	1
Max energy	240 mJ	125 mJ	80 mJ
Ave power	630 W	625 W	-
Power per spike	8 kW	2-3 kW	1.6 MW
Spot diam (f=15.6mm lens)	150 μ m	150 μ m	150 μ m
Power density (per spike)	$4.5 \times 10^{11} \text{ Wm}^{-2}$	$1.7 \times 10^{11} \text{ Wm}^{-2}$	$9 \times 10^{13} \text{ Wm}^{-2}$
Power density (ave)	$3.6 \times 10^{10} \text{ Wm}^{-2}$	$3.5 \times 10^{10} \text{ Wm}^{-2}$	-

2.1.3 Auxiliary Spark Discharge

Excitation of the vapour plume can be enhanced by applying an auxiliary spark discharge across it. A pair of carbon electrodes (spectral pure) are positioned above the target surface (0.4 - few mm), with a point-to-point spacing of 0.5 to 2 mm. A voltage just below that of the breakdown potential in air, is applied across the electrodes. The rising vapour plume enters the electrode gap and initiates the spark discharge.

The discharge circuitry consists of one of four fixed capacitances of 1.0, 1.5, 2.0 and 2.5 μ F which can be charged to a maximum potential of 5.0 kV, giving a maximum spark energy of about 30 J. One of six inductances between 30 and 1000 μ H is in series with the spark gap. Increasing the capacitance is found to increase the overall intensity of the spectrum (including the molecular cyanogen (CN) bands). Increasing the inductance increases the ratio of atomic to ion species in the spark. Increasing the spark potential increases the population of the ions and also the overall spectrum intensity. Of the three main cyanogen bands which we observed, only the one with its bandhead at CN 388.34 has a possibility of interfering with element lines of an analysis since the

other two are very weak. However its effect can be reduced substantially by choosing the lower values of capacitance and inductance. The main carbon lines detected are CII 426.7 nm (doublet), CII 283.7 nm (doublet) CI 247.8 nm and CIII 229.7 nm. The ion lines disappear with step-wise increase of inductance, and the atom line does not vary markedly. All the line intensities increase with capacitance. The background continuum is reduced if low inductance and capacitance are used.

2.2 QUARTZ SPECTROGRAPH

All the time-integrated spectrograms produced in this work, were recorded using a quartz prism spectrograph (Carl Zeiss, Jena, Type Q24). The Q24 has a maximum aperture of $f/11$, and is designed to operate in the wavelength range 200 to 500 nm. The linear dispersion (inverse) is 0.39 nm mm^{-1} at 200 nm, 1.3 nm mm^{-1} at 300 nm and 3.15 nm mm^{-1} at 400 nm. The slit width is continuously variable between zero and 300 μm , and the height is adjustable in steps from 1 mm to 12 mm. A three step filter can be rotated in front of the slit for use in plate calibration and a wavelength scale can be exposed directly onto the photographic plate. The filter is constructed of quartz coated with platinum with steps of 100%, 50% and 10% transmittance respectively.

2.2.1 Spectrograph Illumination

In qualitative analysis, the requirements for illuminating the spectrograph with the light source are different from those needed in quantitative analysis. For qualitative work the maximum possible amount of light must be relayed to the spectrograph so that the minor constituents in a specimen can be detected. A single condenser focuses a X3 enlarged image of the source directly onto the slit (Fig 2.7a). The position of the condenser, and its diameter are chosen so as to completely fill the spectrograph

collimator with light, thus fulfilling the condition of maximum light input (Betz and Johnson, 1971). When the light source is focused on the slit, a spatially resolved image appears in the film plane. This method of illumination is useful when the spatial characteristics of the source are being studied. Since the resolution of spectral lines is important in qualitative analysis, a narrow slit width is chosen. With the Q24, a 10 μm slit gives a resolution factor which is 0.78 maximum and an irradiance at the collimator lens of 0.77 maximum. For quantitative work, the slit must be uniformly illuminated. This is desirable since microphotometer measurements are usually made of the photographic density of the lines, and errors will result if the density is not uniform over the total length of the lines. Uniform illumination of the slit can be accomplished (for example) by two-step focusing of an image of the source in the plane of the collimator lens (Mika and Torok 1974, p301). A magnified image of the source is formed, by a short focal length condenser, onto a disc with a hole in it, mounted on a second (longer focal length) condenser (Fig 2.7b). The image of this hole is focused onto the collimator lens of the spectrograph by a field lens placed in front of the slit. The long focal length lens projects the image of the homogeneously illuminated short focal length lens onto the slit, thus ensuring uniform illumination of slit. The two-step method ensures that the radiant power entering the spectrograph is the same as that obtained with the single-collecting lens (Betz and Johnson 1971). Thus the effects of light loss, loss of resolution and image degradation are minimised. A large slit width ensures that brightness, exposure time and line density are independent of slit width. A 30 μm slit gives a resolution of 0.31 maximum and an irradiance of 0.93 maximum.

The condenser lenses used to illuminate the spectrograph are UV achromats (Carl Zeiss, Jena) of focal length 75.8 and 150 mm. The lenses

are quartz/LiF combinations corrected so that the focal lengths at 253 and 589 nm are equal. This simplifies the procedure for setting up the illuminating system.

2.3 PHOTOGRAPHIC TECHNIQUES AND MATERIALS

The photographic medium is used almost exclusively for the data recording and diagnostic work reported in this thesis. Particular emphasis must therefore be placed on the sensitometric characteristics and the processing of photographic emulsions. In general the measured photographic density (D) of an exposed film must be related to the relative logarithmic exposure value (Q) through the characteristic curve (Hurter and Driffield Curve) of the emulsion (Mees 1954, Mika and Torok 1974). This is an empirical relationship for which, as yet, no direct mathematical expression has been found. The relationship between D and log Q is affected by many factors which include, the film, the developer, the wavelength of the light source, the development process, the development time, and the intensity and duration of the exposure. Thus, for precise work a characteristic curve must be constructed for each plate or length of film used, and for all wavelength regions of interest.

2.3.1 Film and Plate Development

We adopted the technique of dish/brush development of all negative photographic materials. The plates are developed in a flat dish and the developer is spread evenly over the emulsion by regular strokes along the length of the emulsion with a soft flat brush. This method of development is recommended when single plates are being developed. With practice this method yields evenly developed plates, the background fog density level varying by no more than 3% over the emulsion length (Mika and Torok 1974, p451).

For most of the work involving time-integrated spectrograms, Ilford LN plates were used in conjunction with Kodak D 19 developer. This is a high speed emulsion of moderate contrast and graininess, the wavelength sensitivity range is 230-500 nm. The plates were developed with brush agitation (1 brush stroke every 10s) in D 19 for 6 min at 20C. This combination yields a constant contrast factor (γ) in the range 275 to 320 nm.

For the time-resolved photographic work, Polaroid film was generally used, but when intensity measurements were required, it was necessary to use negative film. For this purpose Kodak Royal X-Pan was used with D 19 developer. This very fast panchromatic film (1250 ASA) has moderate contrast and a coarse grain structure. To increase the speed to that of Polaroid films (about 3000 ASA), the Royal X Pan was bathed in 3% solution of sodium metabisulphite prior to development in D 19. The film was brush-developed for 6 min at 20C, yielding an approximate speed rating of 3000 ASA. The coarse grain structure which resulted from this technique was a necessary sacrifice to gain film speed. This technique for enhancing the emulsion speed was also used with the Ilford LN plates when it was necessary (eg with the Pockels' cell work described in Chapter 4).

2.3.2 Plate Calibration by the Preliminary Curve Method

The preliminary curve method of emulsion calibration is particularly suitable for use in spectrochemical analysis, because a calibration spectrum of iron or steel can be included on each plate and calibration can be quickly and easily carried out at different wavelengths. Only a two-step filter is required and thus the illumination of the spectrograph need only be uniform over two or three millimetres of the slit height. The method is described by Mika and Torok (1974 p426) and Feldman (1960) but is repeated here since plate calibration is essential for precise spectrochemical analysis. The method is described as it is applied to Laser

Microanalysis.

A target such as iron is chosen because it yields a plasma rich in spectral lines. The plasma and spectrograph are arranged for uniform illumination of the slit (sec 2.2.1). The iron plasma is photographed through a two-step neutral density filter in front of the Q24 spectrograph slit. The Q24 contains a three-step filter of 100%, 50% and 10% transmission values which can be rotated in front of the spectrograph slit, but only two of the steps are needed, of which the 50% and 100% steps are most useful. An iron spectrum is obtained on the plate which contains a step recorded at 100% transmission and one at 50% transmission. There is a logarithmic ratio of 0.30 between the two steps.

In obtaining a characteristic curve from this spectrum, a preliminary curve is first constructed. A small wavelength range (of no more than 10 nm) is chosen around the region of interest, in which about twenty spectral lines of wide range of densities can be selected. The density of each spectral line is measured for the two steps and a graph is plotted of $D_{100\%}$ vs $D_{50\%}$ for each of the twenty or so lines. This is the preliminary curve. A typical preliminary curve for a steel plasma at 265 nm is shown in Fig 2.8.

The next step is the construction of a calibration curve. We require to plot a curve of optical density (D) vs log exposure ($\log Q$) where the $\log Q$ axis is labelled in units of the log step ratio, ie 0.30. Referring again to the preliminary curve, we select a point with the lowest possible $D_{50\%}$ value (say point a), this point together with its corresponding $D_{100\%}$ value (b') is plotted on the (separate) characteristic curve. Point a is plotted on the y-axis (optical density) of the characteristic curve, at an arbitrary point (say zero) on the x-axis (log exposure). The point b is plotted at one log step unit (ie 0.30) greater than point a. Returning now to the preliminary curve, point b' is transferred to point b on the $D_{50\%}$

axis (ie $|b'| = |b|$), and a new value of D 100% is obtained from this ie point c'. Point c' is now plotted on the characteristic curve one log step ratio greater than bb'. This procedure is continued until a complete characteristic curve is built up as shown in Fig 2.8.

2.4 IMAGE CONVERTER CAMERA

Much of the experimental work was based on the time development of the plume and time-resolved spectroscopy of the plasma emission. For this work an Image Converter Camera (TRW/STL model 1D) was used. The camera consists of a camera head, an operating console, various framing and streak plug-in units and a trigger delay generator.

2.4.1 Image Converter Camera Model 1D

The camera head is shown schematically in Fig 2.9. The light emitted by a luminous transient is imaged by the objective lens onto the photocathode. Electrons are ejected from the photocathode according to the initial photon distribution. Thus the photon image has been converted into an electron image. The electrons are drawn from the photocathode by an accelerating potential of 15 kV, and focused on the photoanode to form an optical image which is, in turn, focused onto the film plane of a conventional camera.

The gating grid acts as a shutter by preventing or allowing electrons to pass, by the application of a potential with respect to the photocathode. The beam is turned on and focused by a positive potential of 160 V and cut-off by a negative potential of 90 V. The image can be moved across the photoanode by applying a voltage to the deflection plates at the crossover of the electron beam.

The photocathode has an S-20 spectral response. The objective lens is an STL Elgeet Navitor, f/2.0, 125 mm focal length with a closest focusing

distance of 12 inches. The rear lens is an STL Elgeet Navitor, double coated, f/1.2, 85 mm focal length. The resolution is 16 line pairs per millimetre at the centre frame for a 200 ns exposure.

The films normally used are the fast Polaroid films 410, 107 or 57. If intensity measurements are to be made, then Kodak Royal-X Pan is used (sec 2.3.1).

2.4.2 Streak and Framing Units

The camera can be operated in either the streak (sweep) mode or the framing mode according to the choice of plug-in unit. In the framing mode a pulse is applied to the gating grid which switches on the electron beam, and is removed after a short time, cutting off the beam. Hence the film is exposed for the duration of the pulse. If the first pulse is followed by more pulses at rapid and pre-determined intervals, a photograph is obtained which contains a number of frames showing the spatial and time development of the luminous transient. The subsequent images are deflected onto different parts of the photoanode to prevent overlapping images. In the streak mode the grid is positively pulsed for the duration of the exposure, while the image is deflected linearly downward across the screen by a ramp voltage applied to one of the deflection plates. In this way we obtain a continuous record of the temporal development of a thin spatial element of the source.

We normally used the Type 4B Standard Framing Unit or the Type 5B Wide Range Streak Unit. The 4B Framing Unit offers three frames of 50, 100 or 200 ns exposure duration (set from the operating console) and interframe delay times of 0.5, 1, 2, 5, 10 μ s. The 5B Streak Unit offers streak durations of 0.5, 1, 2, 5 or 10 μ s (ie film writing speeds of 100, 50, 25, 10 and 5 mm μ s⁻¹ respectively). The maximum

time resolution (for the 0.5 μs streak) is 0.5 ns.

2.4.3 STL Trigger Delay Generator Model 2A

Both the 4B and 5B units require an input trigger pulse of 300 V and 10 ns rise time, this is derived from the Model 2A Trigger Delay Generator. The 2A will accept either an optical input (fibre optic light guide) or an electrical input. The minimum sensitivity of the optical input is 250 μW on the photodiode and the spectral response is 350 to 650 nm. The electrical input trigger pulse must be between 1 and 500 V with a rise time greater than 1 $\text{V } \mu\text{s}^{-1}$. The output trigger pulse can be delayed from zero to 99.99 μs . The minimum internal delay between input and output pulses is 30 ns. The optical input can be monitored and displayed on a CRO.

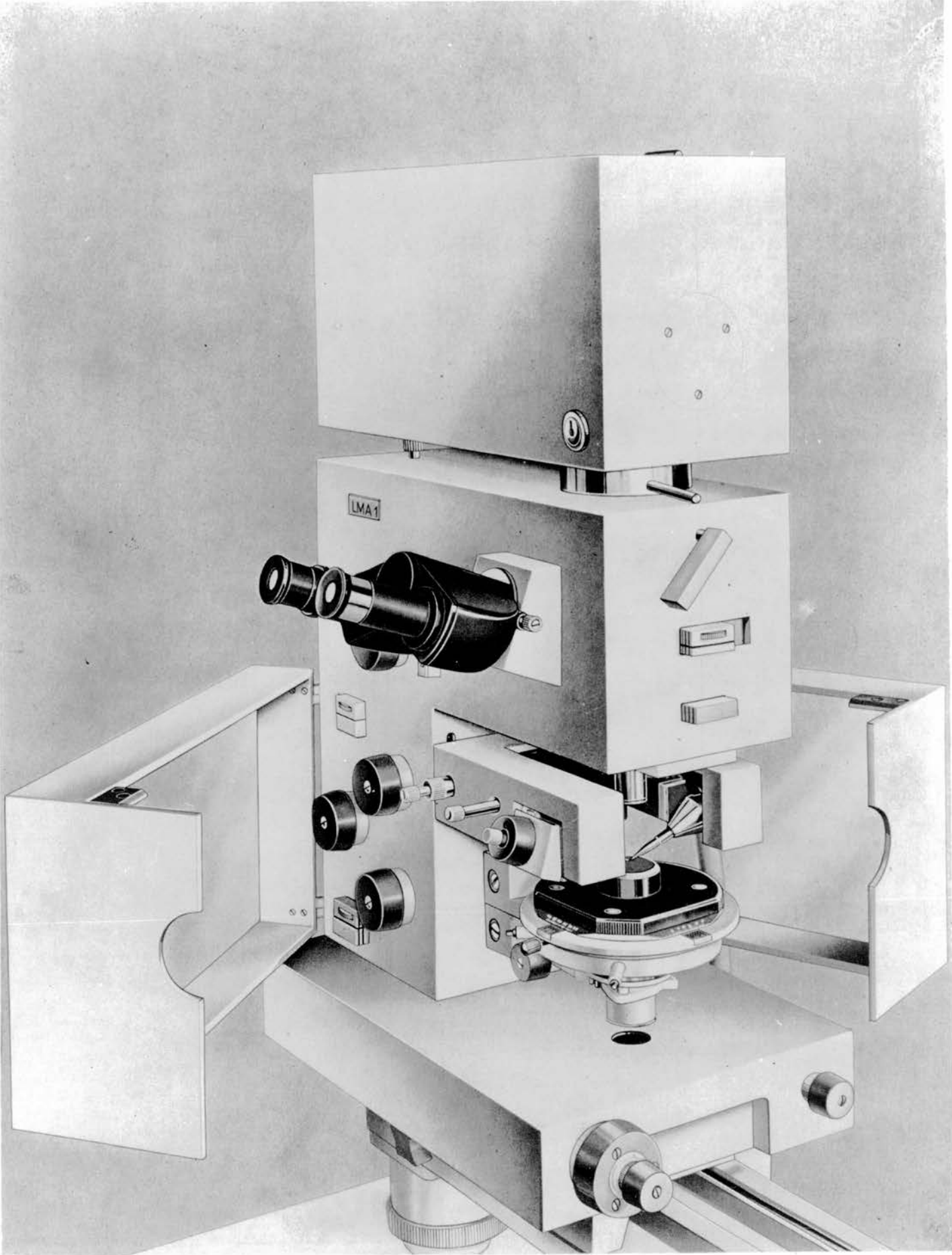


FIG 2.1: THE LASER MICROANALYSER, LMA-1

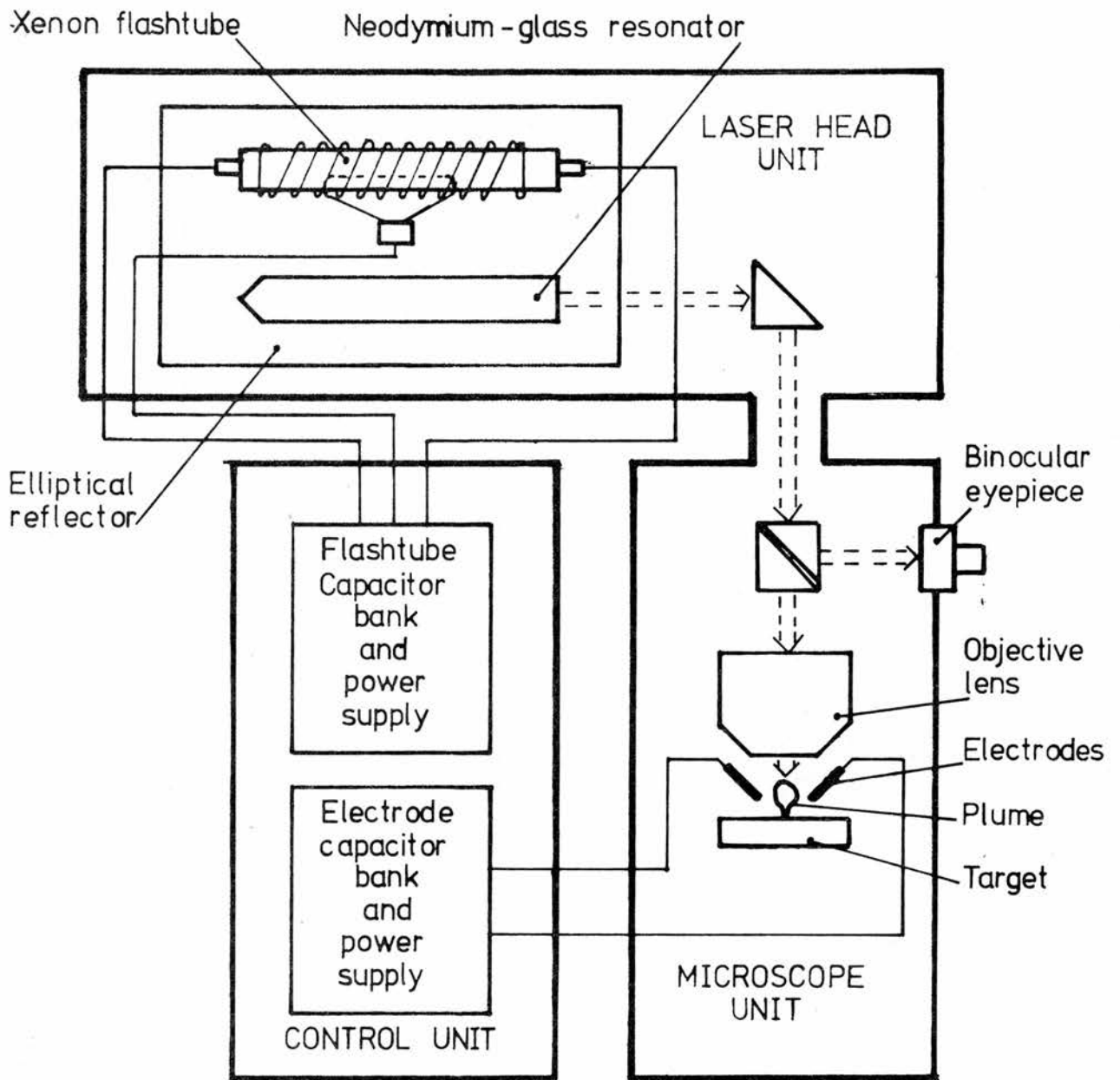


FIG2.2: SCHEMATIC OF LASER MICROANALYSER LMA-1

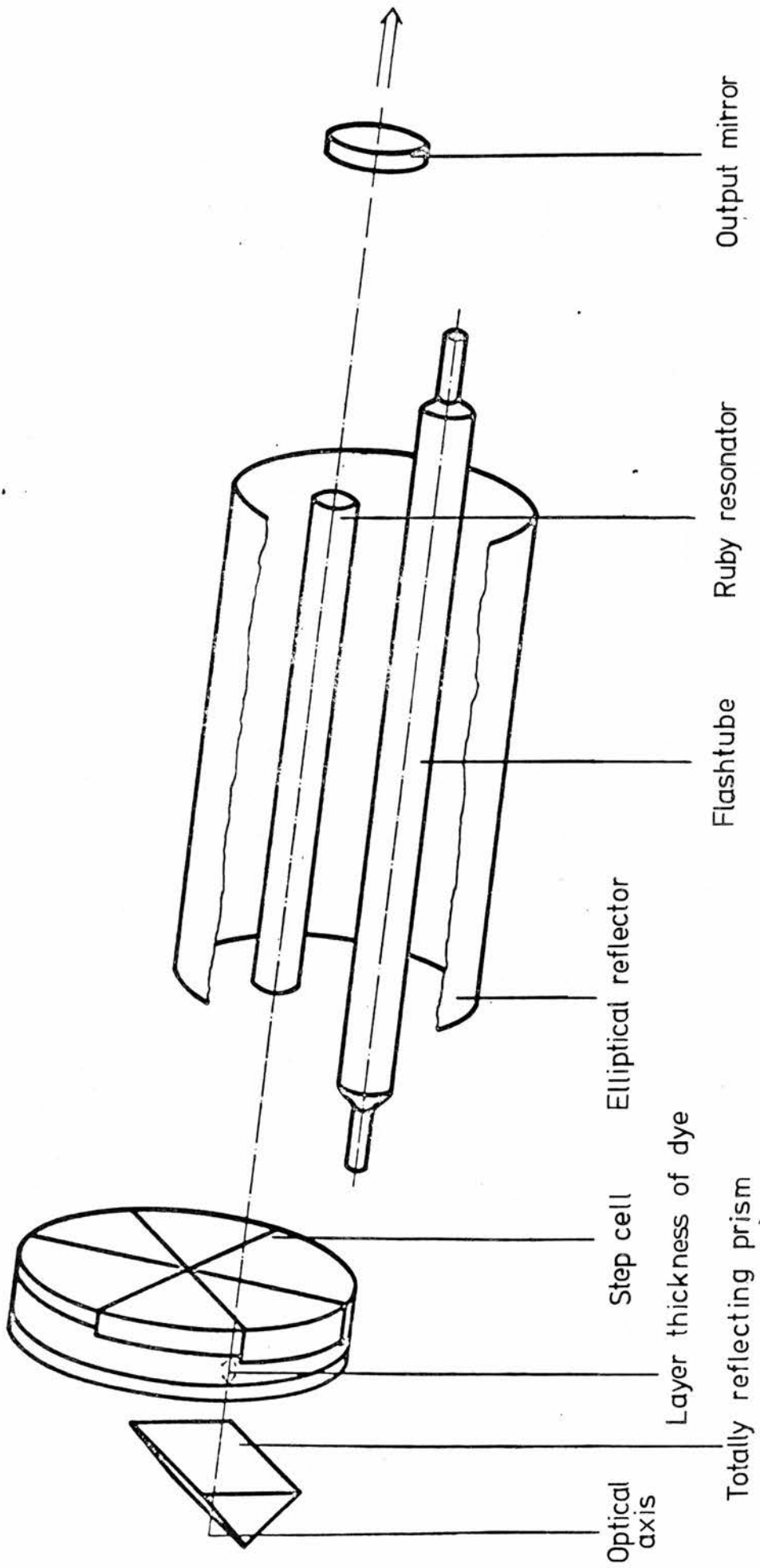
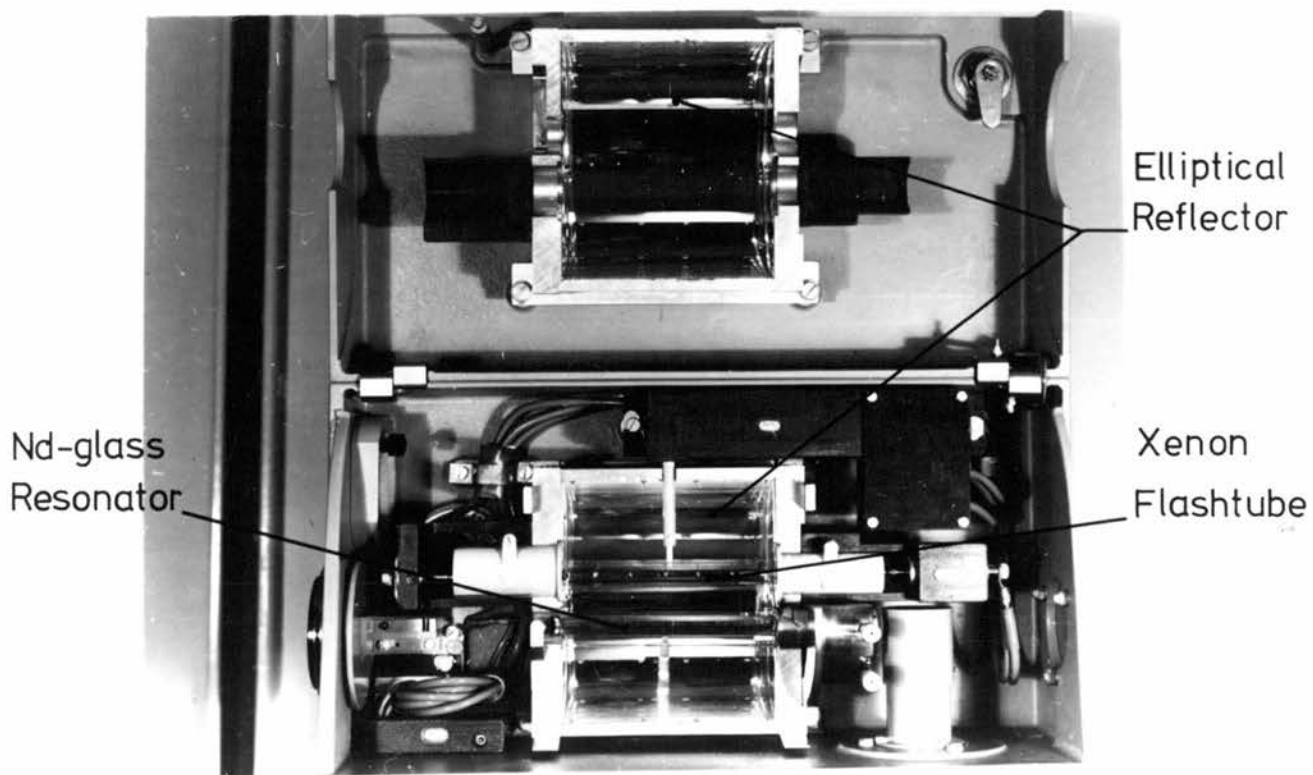
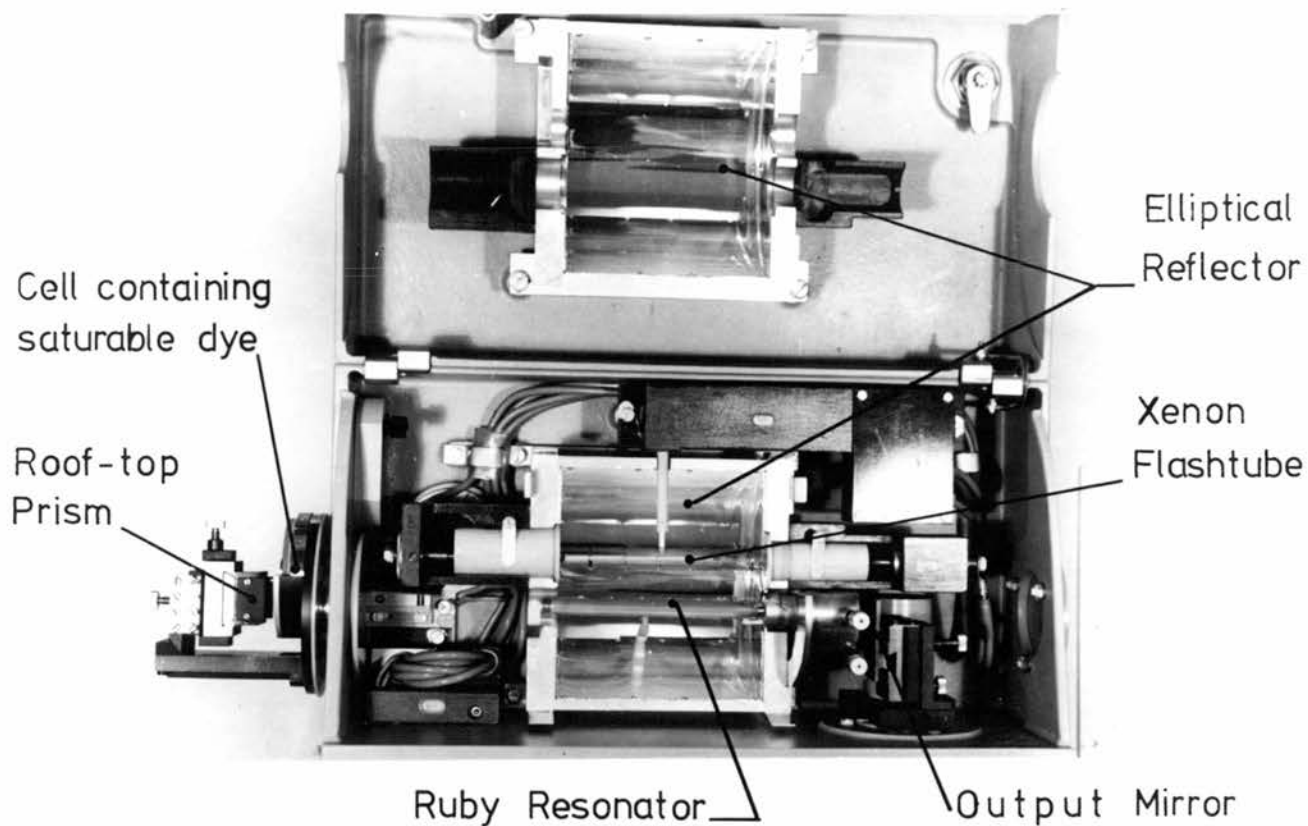


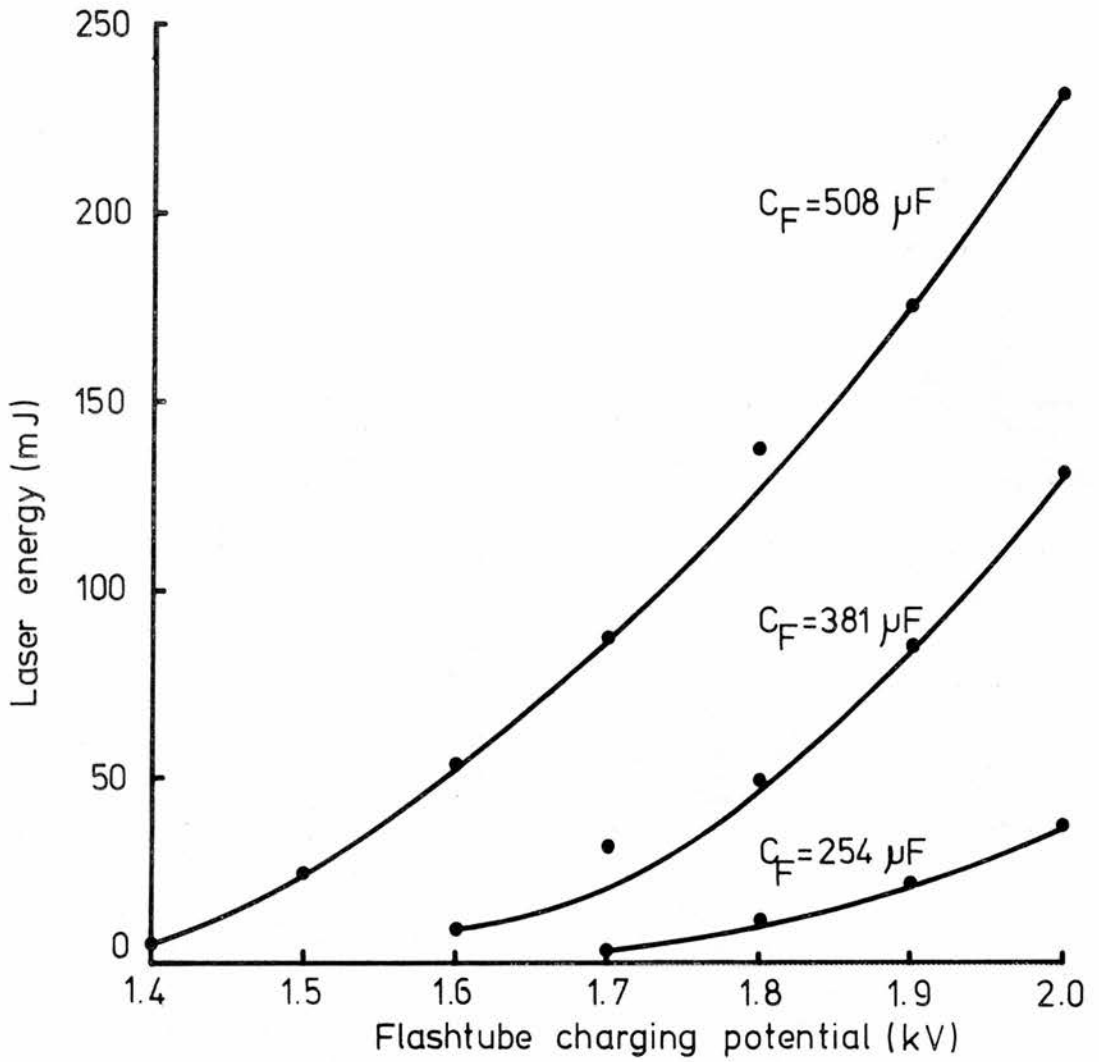
FIG2.3 : Q-SPOILING ARRANGEMENT

(a). Laser head fitted with Ruby resonator and showing Q-spoiling arrangement.

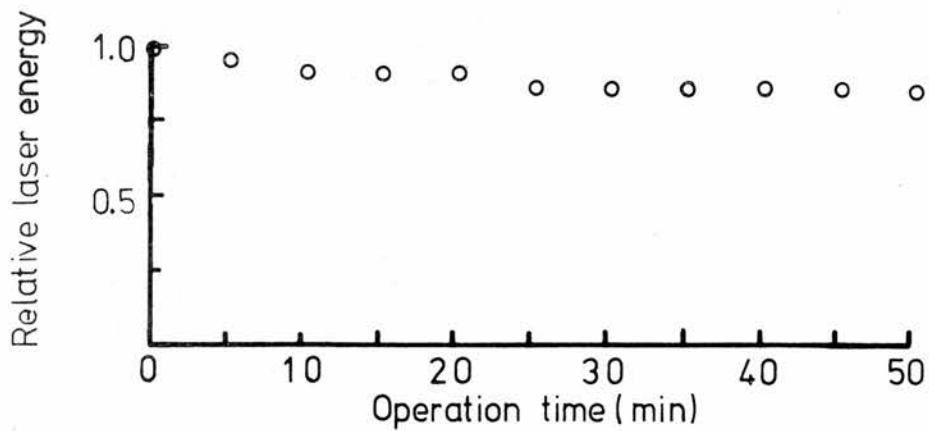


(b). Laser head fitted with Nd-glass resonator for normal pulse operation.

FIG2.4: THE INSIDE OF THE LASER HEAD SHOWN IN THE Q-SPOILED AND NORMAL PULSED ARRANGEMENTS.



(a) Laser energy vs. Flashtube charging potential for various discharge capacitances (C_F).

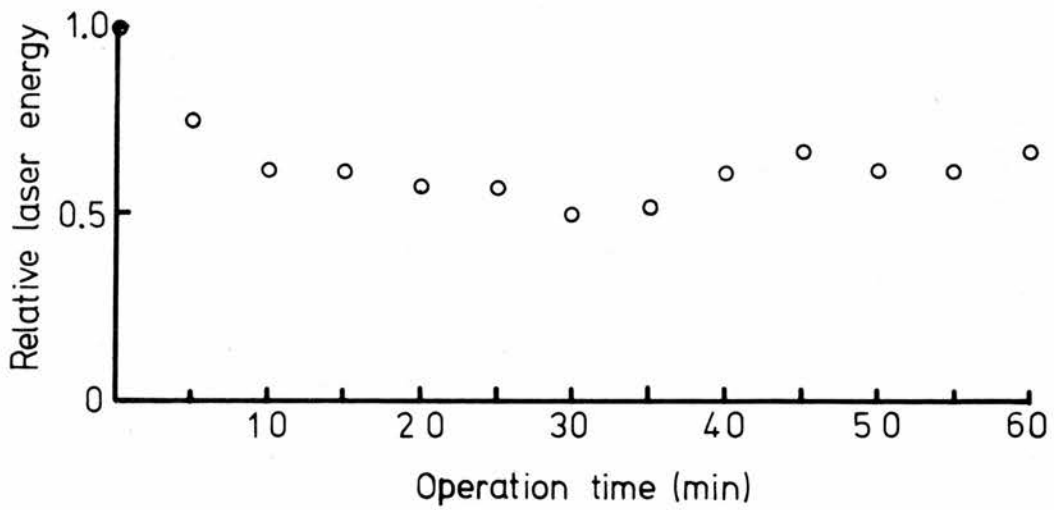


(b). Laser energy vs operation time.

FIG 2.5 : Nd-GLASS LASER ENERGY VARIATION WITH FLASHTUBE CHARGING ENERGY AND OPERATIONAL TIME.



(a) Output Pulses from Ruby Laser



(b) Relative Laser Energy vs Operation Time

FIG 26: OUTPUT CHARACTERISTICS OF RUBY LASER

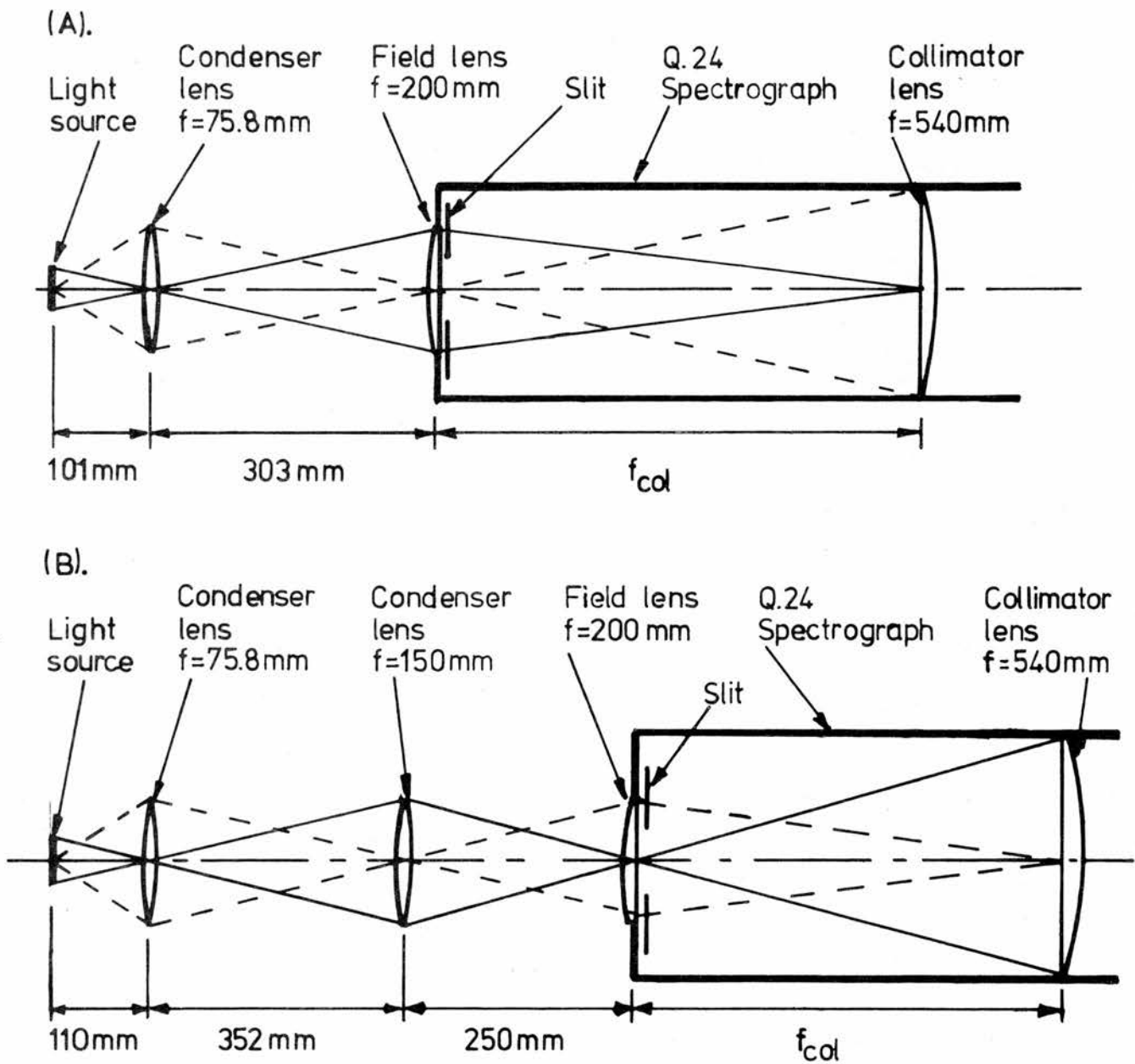


FIG.2.7: IMAGING OF LIGHT SOURCE ON SPECTROGRAPH BY:
 (A) FOCUSING ON SLIT and (B) TWO-STEP FOCUSING
 ON COLLIMATOR LENS.

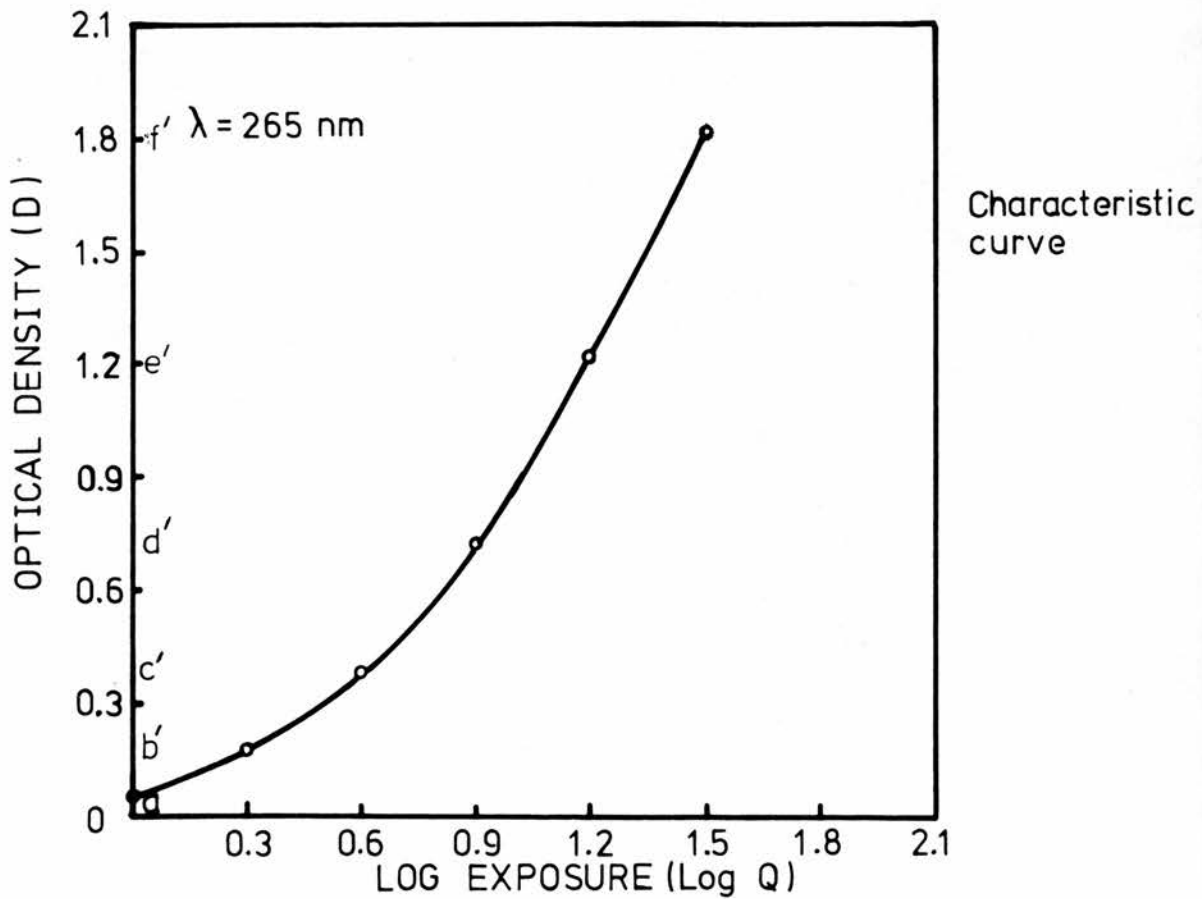
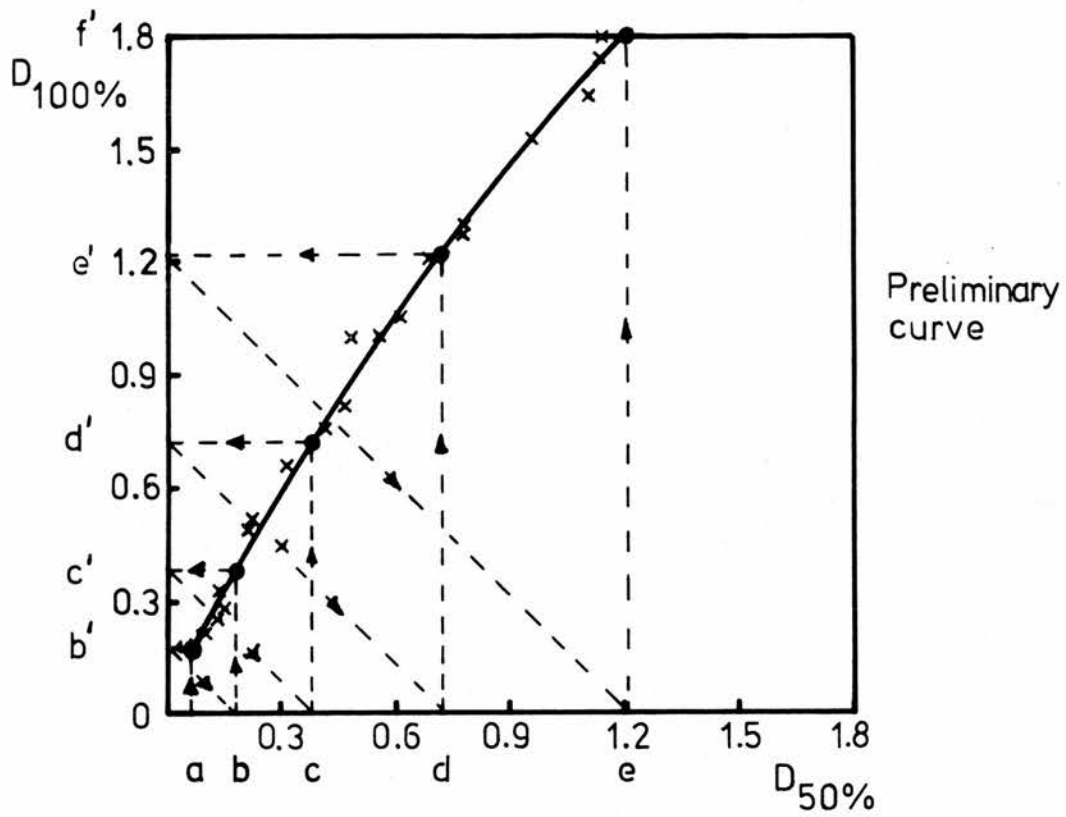


FIG 2.8: CONSTRUCTION OF CHARACTERISTIC CURVE OF A PHOTOGRAPHIC EMULSION BY THE PRELIMINARY CURVE METHOD.

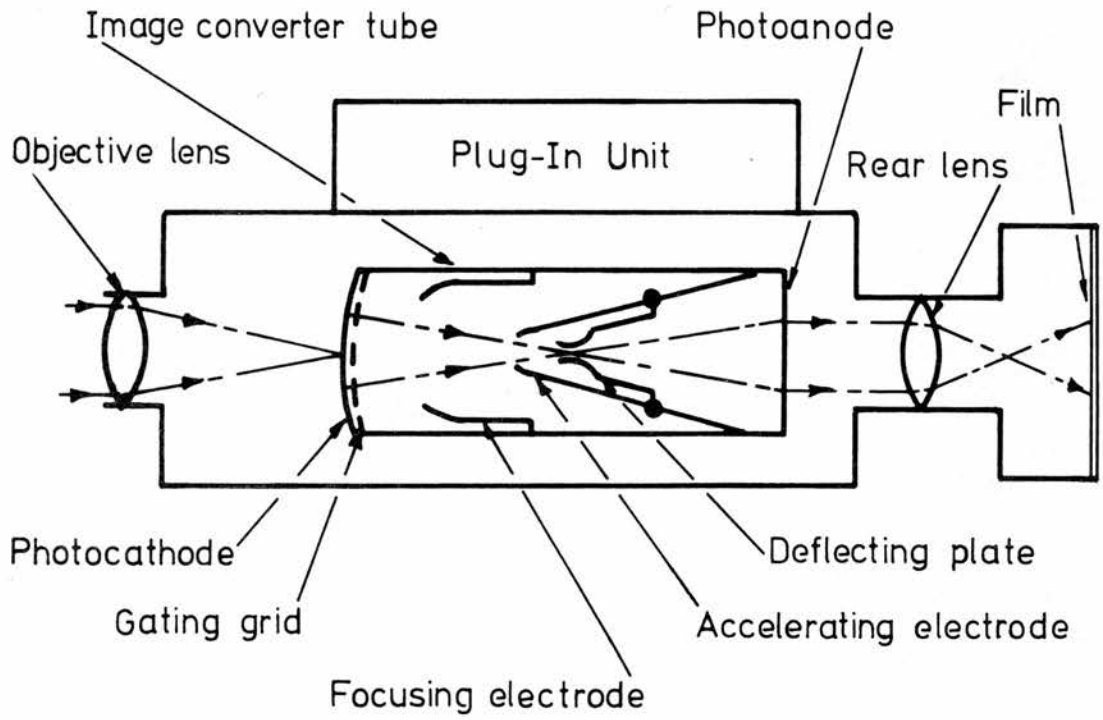


FIG 2.9: TRW/STL IMAGE CONVERTER CAMERA HEAD.

CHAPTER 3

SPECTROSCOPY OF LASER-PRODUCED PLASMAS

We describe here the spectral diagnostics of laser-produced plasmas, and present the results and conclusions of this work. We first report on spectral intensities measured from time and spatially integrated spectrograms. The electron temperature and electron density are estimated for the four basic modes of plasma production. We then present time and spatially resolved spectrograms of various laser-produced plasmas and again estimate the temperatures and densities with respect to plasma lifetime and plasma height. We have also estimated the velocity of ejection of atomic and ionic species into the plume.

From this work we gain an insight into the kinetics of the laser-produced plasmas, and have several useful pointers to the application of laser plasmas to quantitative spectrochemical analysis.

3.1 TIME AND SPATIALLY INTEGRATED SPECTRA

We photographed the spectral emission from the plasmas produced at a steel sample using the ruby laser in the four basic modes of plasma production (spark assisted RO and QS mode laser plasmas and unsparked RO and QS mode plasmas). The plasma was imaged on the slit by the two-step method of uniform illumination (Sec 2.2.1) thus the spectral intensities were spatially integrated over the length of the slit. Since a photographic plate integrates intensities over the duration of the exposure the spectral intensities described in this section are both time and spatially integrated. From these integrated intensities the electron temperature and density, averaged for the total emitting plasma are estimated for each plasma type.

A spectroscopic steel standard was analysed using the four modes of target excitation and plasma production. The input energy to the flash

lamp was in all cases 1016 J. Where appropriate the spark parameters were 2.5 kV, 2.0 μ F and 60 μ H, the electrode separation was 1.0 mm and the electrode-target distance was 1.2 mm. The slit width and height were 25 μ m and 1 mm respectively, except for the unsparked RO mode where the slit width and height were 30 μ m and 2 mm respectively. The spectrograph aperture was f/15 for the spark-assisted plasmas and f/11 for the unsparked plasmas. The spectra from each mode were recorded together with a calibration spectrum on separate Ilford LN plates. The plates containing the spark-assisted spectra were processed in Kodak D.19, and those containing the unsparked spectra were soaked in sodium metabisulphide solution prior to development, to enhance the emulsion speed (sec 2.3.1).

Using eqn (1.54), we plotted

$$\ln \left[\frac{J_{pq} A_{mn} \lambda_{pq} g_m}{J_{mn} A_{pq} \lambda_{mn} g_p} \right] \quad \text{vs.} \quad (E_p - E_m)$$

for a number of FeII line pairs, λ_{pq} and λ_{mn} , where λ_{pq} is the wavelength of the higher lying line and J_{pq}/J_{mn} is the photographically measured line intensity ratio. Applying linear regression analysis, a straight line of slope $-1/kT_e$ and zero intercept can be fitted to the plotted data. The results for the four excitation modes are shown in Fig 3.1. The intercepts, although not passing through the origin, are within 95% confidence limits of a zero intercept. The electron temperatures for each mode were estimated from the slopes of the regression lines, and the associated error derived from the standard error of the regression line (as defined by eqn C.12).

From the estimated values of kT_e , we can calculate the electron density (N_e) for each excitation mode, by eqn (1.53). The electron density was estimated using a number of FeII/FeI line pairs for each excitation mode, and an average value obtained. The associated standard error of the electron density was estimated using eqn (C.3). The average electron temperatures and densities, estimated for the four excitation modes are shown in Table 3.1, together with their standard errors (SE) and the number of data points (n)

used. Also given is the coefficient of determination (r^2), as defined by eqn (C.9).

Excitation Mode	kT_e (eV)	SE	n	r^2	N_e (cm^{-3})	SE	n
Spark-assisted RO	1.05	+0.10 -0.08	13	0.93	3.36×10^{24}	± 0.42	11
Spark-assisted QS	0.96	+0.08 -0.07	13	0.93	1.55×10^{24}	± 0.25	10
Unsparked RO	1.72	+0.21 -0.17	7	0.95	4.08×10^{26}	± 0.50	2
Unsparked QS	1.96	+0.57 -0.36	7	0.80	1.09×10^{27}	± 0.24	6

We see from Table (3.1) that the electron temperatures are higher for unsparked plasmas than for spark-assisted plasmas. Therefore, from the Boltzmann equation (1.47) we expect the spectra emitted from unsparked plasmas to be more intense than the emission from spark-assisted plasmas. However by examining typical spectra produced by each of the excitation modes (Fig 5.1) we see that the reverse is true. We can resolve this anomaly by noting that the spark-assisted plasmas have much longer lifetimes than the unsparked plasmas (milliseconds as compared with microseconds). Thus the integration times for the spark-assisted spectra are longer, and the resulting intensities greater, than for the unsparked spectra.

Calculating electron densities using eqn (1.53) involves an intensity ratio of spectral lines from different ionisation species. However for unsparked plasmas (see Sec 3.2.1), the spectral lines have lifetimes which increase with decreasing ionisation state and the corresponding intensities are integrated over different times. Thus we may not be justified in using eqn (1.53) to calculate N_e for the unsparked plasmas and the values obtained in this way should be treated with caution. However, we can take the

electron densities for the unsparked plasmas as likely upper limits.

Implicit in this work is the assumption that the plasma exists in a condition of local thermodynamic equilibrium (LTE). In the LTE approximation we assume that the distribution of electron populations is governed exclusively by particle collision processes and the time for electron-ion thermalisation is short compared to the expansion rate of the plasma (Sec 1.3.1). A necessary condition for LTE is that the collision rate should be at least ten times greater than the spontaneous emission rate, and this is usually expressed in terms of a minimum electron density (m^{-3}) given by (eqn 1.44).

$$N_e(\text{min}) = 1.7 \times 10^{20} (kT_e)^{\frac{1}{2}} (E_p - E_q)^3 \quad (3.1)$$

where kT_e is the electron temperature in eV and $(E_p - E_q)$ is the energy difference between levels p and q in eV.

If we take the largest value of $(E_p - E_q)$ for the ion/atom line pairs which we have used (ie 10.99 eV for the FeII 275.3 / FeI 272.3 pair) we arrive at values of $N_e(\text{min})$ of $2.96 \times 10^{23} \text{ m}^{-3}$ and $3.16 \times 10^{23} \text{ m}^{-3}$ for the unsparked RO and QS modes respectively; and values of 2.31×10^{23} and $2.21 \times 10^{23} \text{ m}^{-3}$ for the spark-assisted RO and QS modes respectively. Thus the estimated values of N_e in the table satisfy the LTE criterion.

3.2 TIME AND SPATIALLY RESOLVED SPECTRA

We now report on the temporal development of the spectral emission from laser-produced plasmas. A time-resolved spectrograph was improvised (see below) making use of the image converter camera described in sec 2.4. Using this arrangement time-resolved spectrograms were obtained of the spectral emission from plasmas induced by a QS laser, both with and without spark excitation. Traces are presented of the spectral intensity variation with plasma duration and plume height. The variations in electron temperature and electron density with plasma lifetime and height in the plume are

estimated for an Al plasma. Results from this work have been summarised by Maitland and Watson (1976).

3.2.1 Unsparked Plasmas

A magnified image of the luminous plume was focused onto a slit of width 0.2 mm placed perpendicular to the target surface. The light was collimated onto a reflection diffraction grating (600 lines mm^{-1}) and the first order diffracted image collected by the image converter camera.

A series of solid targets were irradiated by the ruby laser operating in the QS mode. Single output spikes of 50 ns FWHM were generated at the ruby wavelength of 694.3 nm with output energy 120 mJ. The radiation was focused to an estimated spot size of 150 μm using a 15.6 mm lens giving a power density at the target of $1.4 \times 10^{14} \text{ W m}^{-2}$. Spectrograms were taken with the image converter camera operated in both the streak and framing modes. A streak duration of 10 μs (writing speed of 5 $\text{mm } \mu\text{s}^{-1}$) was used. In the framing mode, three frames were recorded of 100 ns duration with an interframe delay of 0.5 μs . The camera was triggered from the stray laser light emitted between the corner cube reflector and the saturable dye holder, which are both outside the laser head. This stray light was fed via a light pipe to the photodiode input of the Trigger Delay Generator (TRW model 2A) (Sec 2.4.3), which, in turn, applied the correct trigger pulse to the camera. Allowing for the internal delays in the triggering system, light is first recorded in the photographs 100 ns after irradiation of the target has started.

The spectra were recorded on Kodak Royal X Pan at an image magnification of 1.5 times. In the case of the streak spectrograms a mask was placed at the slit, parallel to the target. The mask was used to sample a 0.4 mm segment of the plume at various heights above the target surface; this results in a temporal resolution, at the film, of 120 ns. The film was bathed in a sodium metabisulphite solution prior to development in Kodak D.19 (Sec 2.3.1)

to give an enhanced film speed of 3000 ASA (36 DIN).

Eight samples were used: 99.0% pure Al sheet (BS 1470/S 1C), 99.9% pure Zn pellets, 99.9% pure Cu sheet, and samples of Mg, Bi, Si, Ge, and Sn, all of unknown purity. All the samples were washed for a few seconds in a 3% solution of nitric acid to remove surface impurities.

Streak spectrograms of the plume development from 0.1 to 10.1 μs after irradiation are shown in Fig 3.2 for Al, Mg, Bi, Cu and Sn plasmas. All the spectrograms correspond to the light emission from a segment of the plume at a point $x = 0.5$ mm above the target surface. The target surface corresponds to $x = 0$. Temporal and spatial resolution is obtained from the framing spectrograms of Mg, Si, Al, Cu, Ge and Zn shown in Fig 3.3. The frames correspond to times $t = 0.1, 0.6$ and 1.1 μs after the leading edge of the laser pulse. The main spectral lines are shown in both sets of spectrograms.

Similar features appear in both sets of photographs. A dense continuum appears early in the plume development, and has a very short lifetime. The continuum is most intense close to the target surface. Spectral line emission appears at the same time as the continuum but has a much longer lifetime. The lines from the ionised species have shorter durations than those of the atomic species eg MgII 448.1 nm has a lifetime of about 1.6 μs whereas MgI 517.8 has a lifetime of about 6 μs .

Photographic density scans of the main spectral lines were made in terms of plume lifetime and height using a microphotometer (Carl Zeiss Jena, type GII). From a film calibration the densities were converted into photographic intensities. No correction was made for background. Traces of relative intensity vs plume lifetime are shown in Fig 3.4 for the Al plasma at heights of $x = 0, 0.5$ and 1.0 mm. A profile of intensity vs plume height is shown in Fig 3.5a for the Al plasma, measured at $t = 0.1$ μs .

The lifetime of the continuum (at $x = 0$) is about 200 to 300 ns, peaking at about 220 ns. The continuum (at $t = 0.1 \mu\text{s}$) peaks at about 0.5 mm.

The spectral lines appear and decay in the plume in a definite order: the ion lines peak first at about the same time as the continuum (230 ns at $x = 0.5$ mm) and decay rapidly. The atom lines peak later (330 ns at $x = 0.5$ mm) and decay over a much longer period. The time at which the spectral lines peak, increases with distance from the target surface. This is most clearly seen for the atom line which peaks at 240, 330 and 440 ns at heights of $x = 0, 0.5$ and 1.0 mm respectively (Fig 3.4). The line intensities also vary with plume height, and the height at which peak intensities are reached increases with decreasing ionic state. For example, the ion line peaks at about 0.5 mm whereas the atom line peaks at about 0.8 mm (Fig 3.5a).

Time-integrated, but spatially resolved spectrograms of the emission from plasmas produced at targets of Fe, Al, Mg, Si, Pb and Bi on irradiation by the RO and QS ruby lasers are shown in Figs 3.6 and 3.7. The plasma emission was focused onto the slit of the Q24 Spectrograph (Sec 2.2.1) to reveal the spatial character of the spectral emission. The spectral lines of the QS plasmas are more intense than those from the RO plasmas. The QS plasmas are characterised by the emission of a strong continuum which is absent from most of the RO plasmas except for those of the heavy metals. Self-reversal may be seen in some of the resonance lines of the atomic and ionic species shown in Figs 3.6, 3.7. The variation in intensity with height above the target is shown in Fig 3.5b for an Al plasma produced by irradiation with the RO mode ruby laser. The continuum, AlI and AlIII lines peak at lower heights than in the QS plasma. Some of the photographs (eg Mg in Fig 3.7) show an intense line of continuum close to the target surface which corresponds to black body radiation from the hot target spot, with a less intense region of continuum above the target, which is probably due to

bremsstrahlung emission (see Sec 3.2.4).

3.2.2 Line-to-Background Ratios

The microphotometer traces indicate that the influences of the background continuum and the ionised species are reduced if the spectral emission is observed late in the life of the plasma and at higher points in the plume. The line-to-background ratio (uncorrected for background) was calculated for Al I 395.6 nm in terms of plasma lifetime and height above the target (Fig 3.8). The line-to-background ratio is at a maximum at about 300 to 500 ns after irradiation has started and at a height of about 1 mm in the plume.

3.2.3 Time and Spatially Resolved Plasma Parameters

As was done with the time and spatially integrated spectra, electron temperatures and electron densities can be deduced from a knowledge of the intensity ratio of a spectral line pair. For the time resolved spectra, we can use the same plasma equations as we used for the time-integrated spectra, with only a modification in the definition of the line intensity ratio. The exposure of a photographic emulsion to a spectral line λ_{pq} is given (eqn 1.57) by

$$Q_{pq} = \int H_{pq} dt \quad (\text{J m}^{-2}) \quad (3.2)$$

where H_{pq} is the irradiance of the spectral line at the film in W m^{-2} .

In time-integrated spectral analysis the exposure time dt is assumed to be constant for all spectral lines. We have seen that in the spectra from QS plasmas this is not the case and that the spectral intensity is a rapidly varying function of time. We can assume that N_p , and hence I_{pq} , is constant for a time interval Δt , determined by the resolution limit for the system (ie 120 ns for the streak spectra). Thus we can write

$$Q_{pq} = H_{pq} \Delta t. \quad (3.3)$$

We can now define the photographically measured intensity as

$$J_{pq} \equiv \frac{Q_{pq}}{\Delta t} = H_{pq} \quad (3.4)$$

and the photographic intensity is related to the line intensity via the constant parameters of the observation system. Thus in terms of a ratio we have

$$\frac{Q_{pq}}{Q_{mn}} = \frac{J_{pq}}{J_{mn}} = \frac{I_{pq}}{I_{mn}} \quad (3.5)$$

This is the same relationship as is given by eqn (1.60), but now the spectral lines are constant during the short time Δt , ie H_{pq} is not a function of time during the short time interval involved. Thus, we can substitute the photographic intensity ratio for the ratio of line radiances in any of the plasma relationships.

Using the Aluminium line pair Al II 623.7/Al II 466.3 the electron temperature can be estimated as a function of plasma lifetime or plume height by applying eqn (1.50). The electron density can be estimated from eqn (1.53) using the line pair Al II 466.3/Al I 395.6 and the values of kT_e calculated as above. The transition probabilities and statistical weights for these lines were taken from Wiese et al (1969).

Figure 3.9a shows the electron temperature (in eV) and electron density (in m^{-3}) as functions of time (at $x = 0.5$ mm) and as functions of height (at $t = 0.1$ μs). The horizontal error bars correspond to the resolution limit Δt , whereas the vertical error bars correspond to the estimated error in the values of kT_e and N_e . Initially (up to $t \sim 0.1$ μs) the plasma temperature (≈ 1.8 eV) is still increasing due to free-free absorption of the laser radiation and high electron densities ($\approx 10^{25} m^{-3}$) are found near the target ($x \approx 0.1$ mm) surface. At a height of 0.7 mm above the target, the vapour has cooled to 0.7 eV and the electron density has fallen to $10^{21} m^{-3}$, which is below that required for LTE to prevail. At later times ($t = 0.2$ μs) in the plasma life, the higher regions of the plume ($x = 0.5$ mm)

have been raised in temperature due to collisional excitation and ionisation of the atoms. LTE conditions may prevail at 0.5 mm above the target in the time range 0.2 to 0.5 μs after irradiation. At times greater than 0.6 μs and at heights greater than 1.6 mm, the line intensities are very small giving a large error in the intensity ratios and a high uncertainty (>60%) in the estimated electron temperatures and densities.

In Fig 3.9a, we have indicated that electron temperature and density decrease with time, even though the plotted points (with a large uncertainty) show an increase. The suggestion that the temperature and density decrease with time can be justified by considering the physical nature and temporal profile of the continuum emission. No radiation with a frequency less than the plasma frequency, ν_p (defined by eqn 1.29) can be emitted from a plasma (see Hughes 1975, p34). If the optical depth of the plasma, d_ν , is much greater than one, the plasma emission will follow a black-body distribution, whereas if the plasma is optically thin ($d_\nu \ll 1$) the continuum emission will be bremsstrahlung. The optical depth is defined (eqn 1.30) by

$$d_\nu = a_\nu L \quad (3.6)$$

where L is the depth of a homogeneous layer of plasma and a_ν is the absorption coefficient, given by eqn (1.31). Thus, setting $a_\nu L$ equal to one, and using eqn (1.31), we obtain the transition frequency, ν_t , at which the continuum emission changes from optically thin bremsstrahlung to optically thick black-body. Applying eqns (3.6) and (1.31) to the data presented in Fig 3.9a for the Al plasma, we see that for times greater than 0.1 μs and at heights greater than 0.1 mm, the plasma can be considered as optically thin (for wavelengths less than about 3.9 μm). So, consequently the continuum emission is bremsstrahlung. It is possible, that, in the early part of the laser-target interaction, (<0.1 μs) a small, high density plasma will be formed which will radiate as a black-body in the wavelength region with which we are interested.

Consider now, the power radiated from the plasma by bremsstrahlung emission. The total power radiated, per unit volume, by bremsstrahlung is given (see Hughes 1975 p44) by

$$P_{Br} \approx 1.4 \times 10^{-40} N_e N_i z^2 (T_e)^{\frac{1}{2}} \text{ W m}^{-3} \quad (3.7)$$

Thus, the power radiated by bremsstrahlung is proportional to the product of N_e and N_i . The time-resolved spectra of the plasma emission (Fig 3.2) show that the continuum emission extinguishes early in the plasma lifetime (by $\approx 0.4 \mu\text{s}$), implying that $N_e N_i$ decays rapidly. Hence we are justified in showing N_e decreasing with time in Fig 3.9a. For typical plasma parameters of $N_e = N_i = 10^{24} \text{ m}^{-3}$, $T_e = 23000\text{K}$ and $z = 1$, we have $P_{Br} \approx 2.1 \times 10^{10} \text{ W m}^{-3}$. For a 2 mm diameter plasma the total power re-radiated by bremsstrahlung is about 900 W, which is less than 0.1% of the power output of a QS laser.

In Fig 3.9b we show temperature-height profiles for Fe plasmas calculated from the spectrograms of Figs 3.6 and 3.7. The temperatures for the QS mode plasmas are higher near the target surface ($\approx 2.4 \text{ eV}$) than for the RO mode plasma ($\approx 1.9 \text{ eV}$). A relatively constant temperature region is obtained for the QS mode plasma between 0.6 and 1.6 mm, whereas the temperature decreases more rapidly for the RO mode plasma. The temperatures at various heights were calculated using three Fe II line pairs (266.6/271.4, 266.4/271.4 and 275.3/271.4) and an average taken. The vertical error bars correspond to \pm one standard deviation, and the horizontal error bars are an estimate of the uncertainty in the height measurement. We did not repeat the time-resolved work with Fe, since the spectral resolution of the time-resolved spectrograms was not high enough to give confident line identification. Transition probabilities, statistical weights, energy levels and wavelengths for Fe were taken from Corliss and Bozmann (1962).

3.2.4 Ejection Velocity and Kinetic Energy

From the position of the intensity peak as a function of plasma time (Fig 3.4) we can estimate the initial ejection velocity of the neutral and singly-ionised species. Assuming that electron-ion recombination is not a dominant mechanism for the production of atomic species (Secs 1.3 and 5.4) we arrive at ejection velocities of $6.3 \times 10^3 \text{ ms}^{-1}$ and $25 \times 10^3 \text{ ms}^{-1}$ respectively for the Al I and Al II species. Thus the corresponding kinetic energies of ejection into the plume are 5.6 eV and 88 eV for the Al I and II species respectively. Thus the presence of the atomic species at later times and greater heights in the plume than the ion species is because the atoms travel through the plume with a lower velocity than the ions.

3.2.5 Spark-assisted Plasmas

Using the same experimental and triggering arrangement as in Sec 3.2.1, streak spectrograms were taken of spark-assisted QS plasmas. The electrodes were positioned 1 mm above the target with a point-to-point spacing of 1 mm. The inductance and capacitance of the discharge circuit were set at 125 μH and 2 μF respectively. The air breakdown voltage for this configuration was 3.1 kV, so the electrode voltage was set to 2.9 kV. The image converter camera was used in the streak mode at a writing speed of $5 \text{ mm } \mu\text{s}^{-1}$ with a sampling mask which selected a 0.4 mm region to give a resolution of 120 ns. The mask could be placed to sample the plume at the electrodes or at the surface.

The photographs shown in Fig 3.10 show two well defined regimes of plasma emission and decay and spark initiation and decay. When the plasma is sampled at the surface, we see that the emission proceeds as it did when no spark was employed, except that Al I 395.5 does not die away completely, but seems to have a much longer tail. At about $t = 5 \mu\text{s}$ the spark lines

appear and increase rapidly in intensity. The spark lines develop strongly and the intensity of the Al lines increase slightly but are never as intense as the spark lines. However, the target lines appear to suffer much less broadening than in the original plume.

When the plasma is sampled at the electrodes, the features are qualitatively similar, but the spark lines appear earlier at about 4 μ s, as would be expected since the centre of action for the spark is at the electrodes. The Al I 395.5 line seems weaker than when sampling is at the surface. This appears to suggest that enough atoms still exist near the target surface 5 μ s after irradiation has ceased for secondary excitation to be at least partly successful. However, it is possible that the spark is acting as a source of secondary vaporisation and is evaporating more atoms from the target. One of the effects of the spark appears to be the introduction of carbon and atmospheric species into the plasma. Some excitation is given to the Al species and the durations of the Al lines are much longer under spark assistance, but the intensity never reaches the maximum attained before the spark is initiated.

Observations of laser-produced plasmas using time-resolved spectroscopy (Archbold et al 1964) showed that when a target is irradiated by a multi-spike laser, the spectral emission from the plasma coincides with the relaxation spikes of the laser. Each laser spike causes vaporisation and ejects target species into the plasma. A substantial amount of excited atoms will be present for most of the laser pulse duration. When the spark is initiated it will be acting on an excited plasma, unlike that for the QS laser when the spark acts on a decaying plasma. Thus spark excitation of RO plasmas is likely to have a greater effect on atom excitation and consequently higher line intensities will be obtained than for spark excitation of QS laser plasmas.

3.3 CONCLUSION

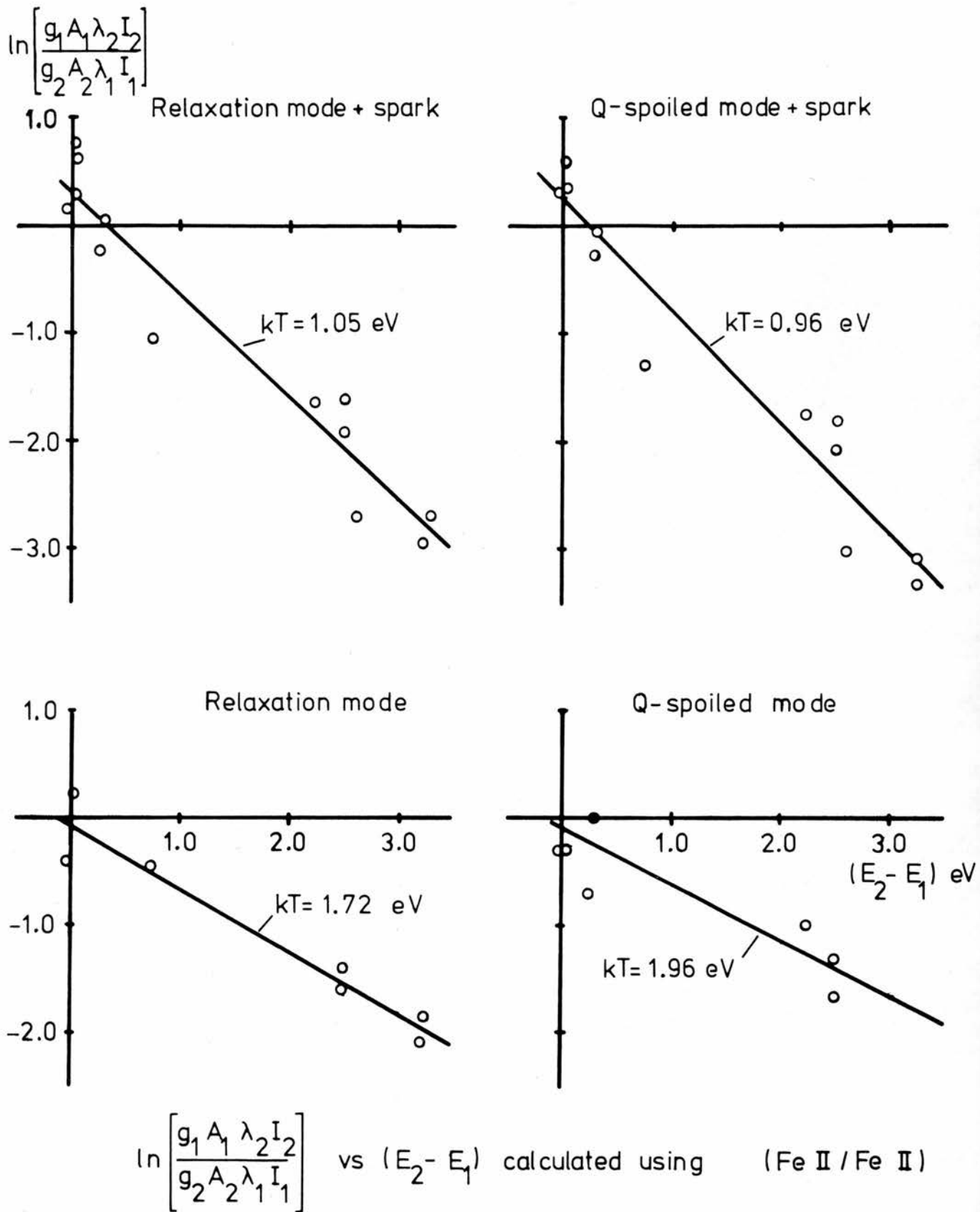
Focused QS laser beams produce a high temperature (1-2 eV), high density

$(10^{24} - 10^{25} \text{ m}^{-3})$ plasma at the surface of metal targets. An intense continuum of bremsstrahlung radiation is emitted early in the life of the plasma (peaking at ≈ 220 ns) and close to the target surface (peaking at ≈ 0.4 mm). Atomic species are ejected from the target at lower velocities than the ion species and hence the atomic lines peak in intensity at later times and at greater heights than the ion lines. The line-to-background ratio of the atomic lines are improved by sampling after the continuum and ionic emission has decayed or by sampling the plume above the continuum region.

The temperature and densities of RO plasmas are generally lower than those produced by QS lasers, and the almost complete absence of a continuum indicates that very little absorption of the laser beam occurs in the plume. The emitted spectrum is composed principally of atomic lines.

We have shown that in plasmas produced by RO and QS mode lasers, T_e and N_e are sufficient to justify the LTE assumption. In the QS mode plasmas T_e and N_e are greatest in the early part of the plume development and close to the target surface. Conditions for the establishment of LTE prevail out to about 0.5 mm from the target and in the time range 0.2 to 0.5 μs . That is, conditions for LTE seem to be most favourable in the presence of the continuum.

Spark excitation has little effect as a means of secondary excitation of the target species in QS plasmas. One of the effects of the spark is to introduce undesirable carbon species into the plume. To obtain more efficient secondary excitation of QS plasmas, the electrodes must be positioned closer to the target, so that the spark will be initiated earlier. In this condition, the spark may act as a secondary source of target sampling, which is also undesirable.



$\ln \left[\frac{g_1 A_1 \lambda_2 I_2}{g_2 A_2 \lambda_1 I_1} \right]$ vs $(E_2 - E_1)$ calculated using (Fe II / Fe II) line pairs, for the four basic sampling modes.

FIG 3.1: ELECTRON TEMPERATURES FOR Fe PLASMAS PRODUCED BY THE FOUR EXCITATION MODES.

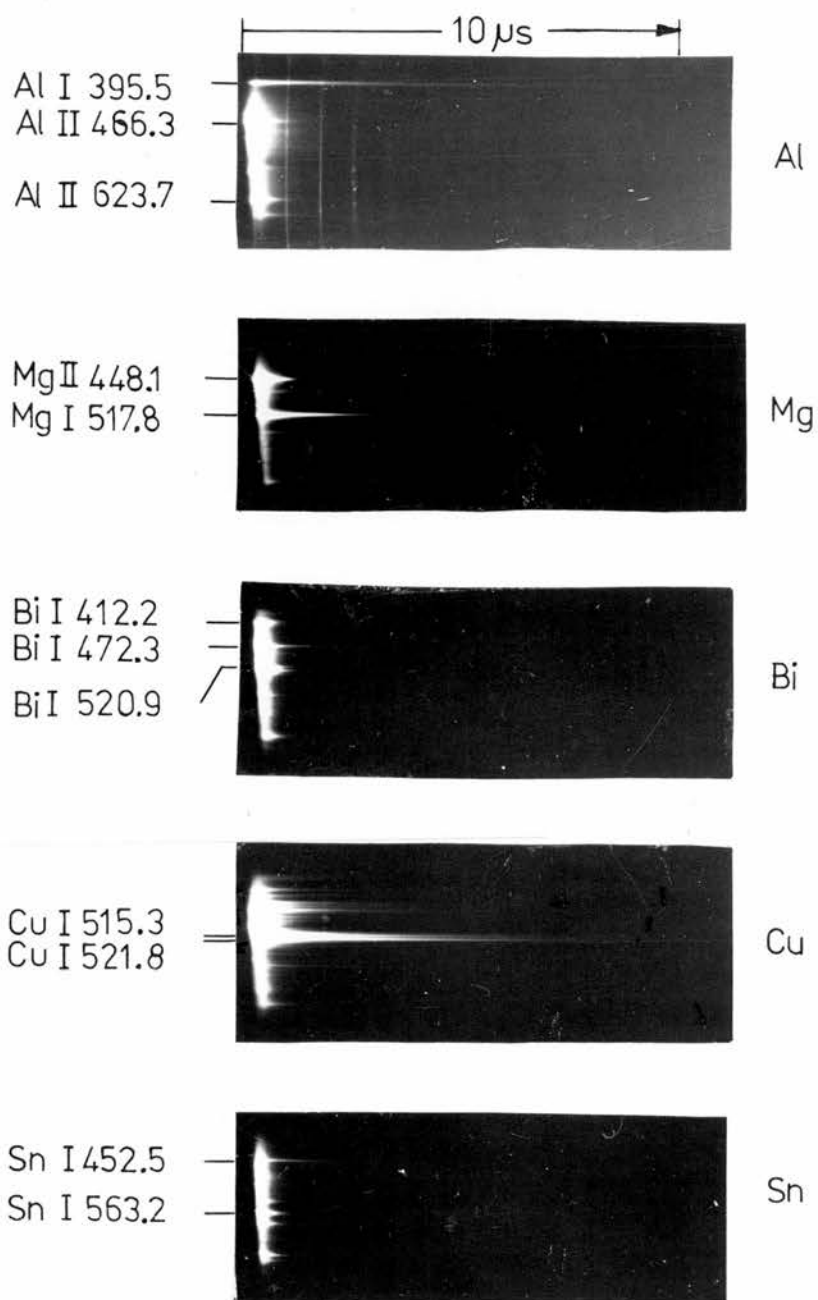


FIG 32: STREAK SPECTROGRAMS.

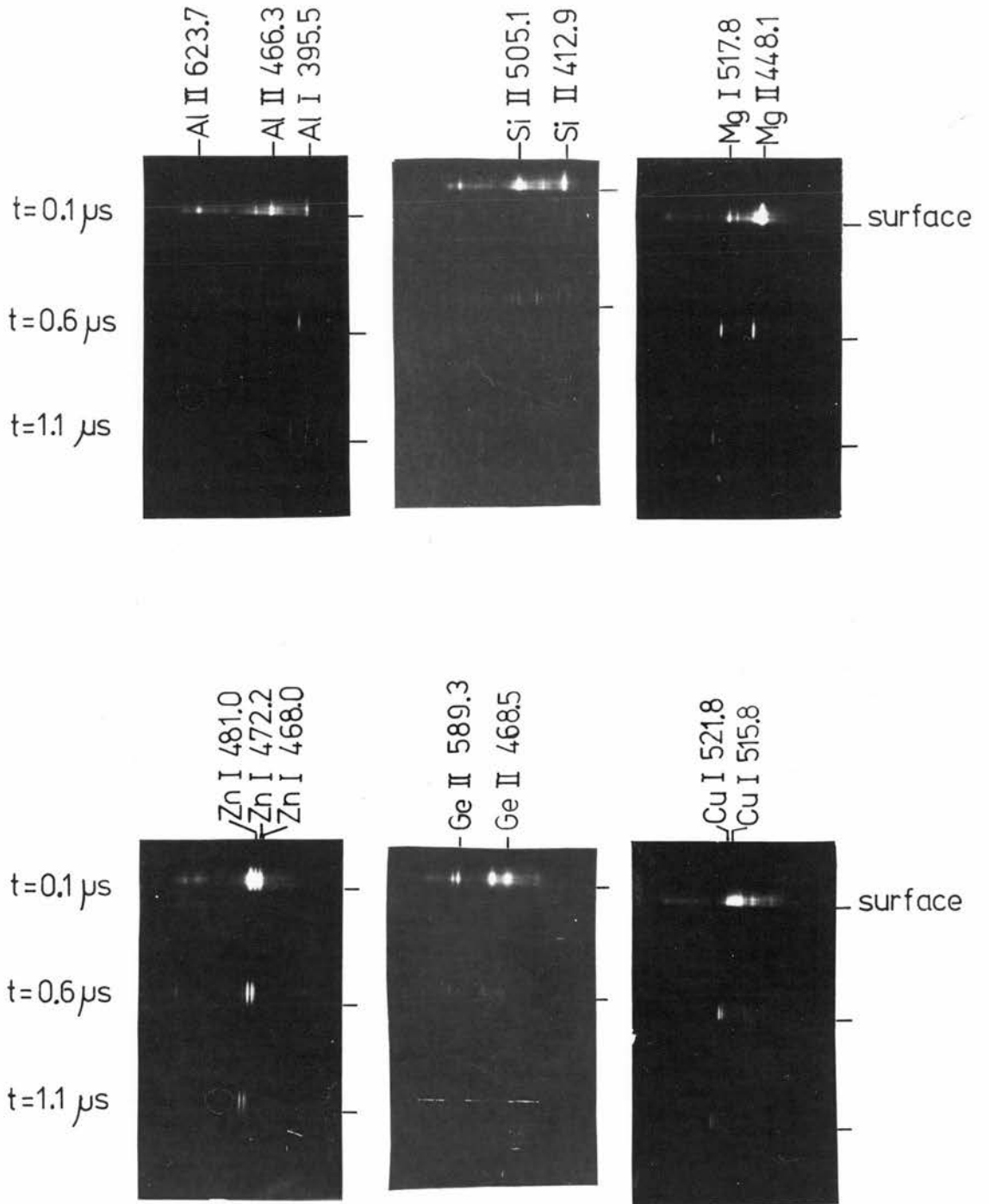


FIG 3.3:FRAMING SPECTROGRAMS.

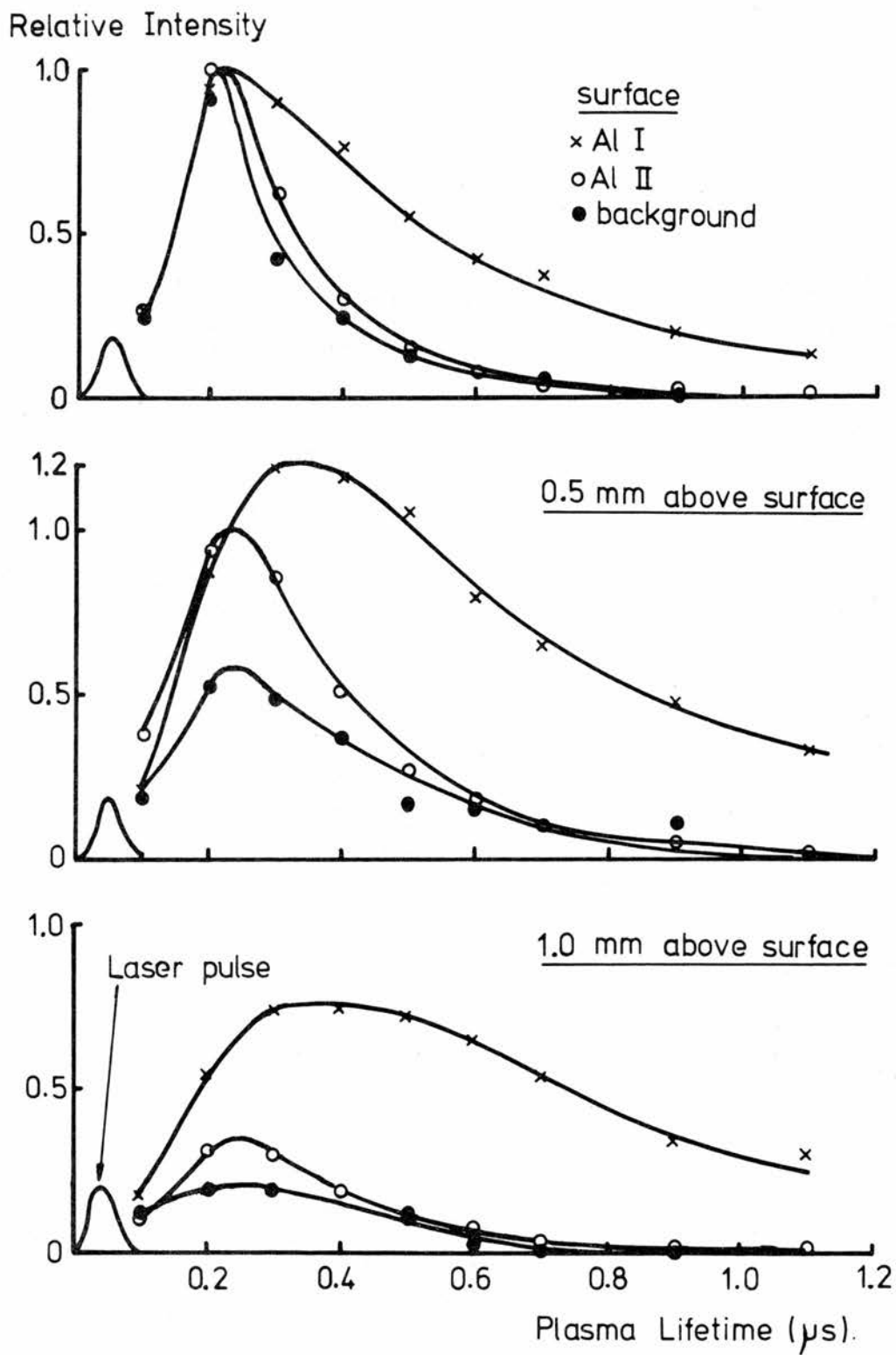
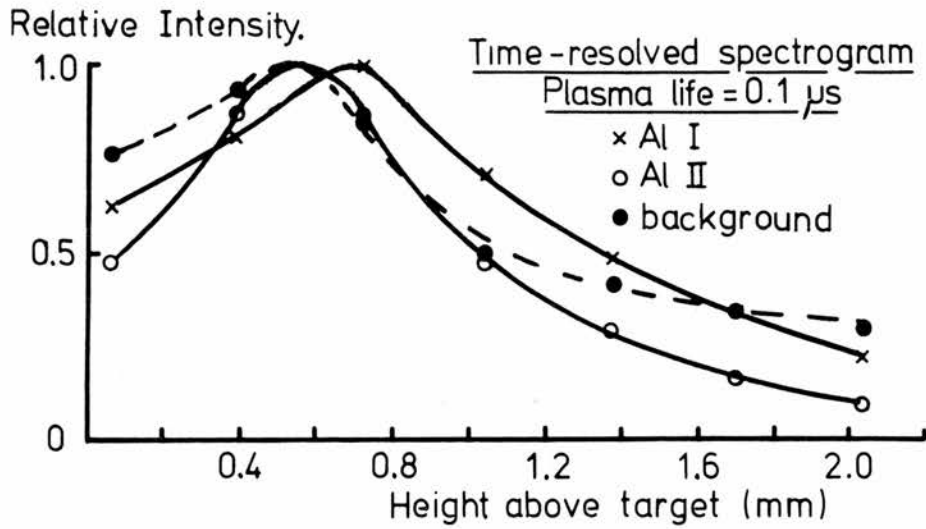
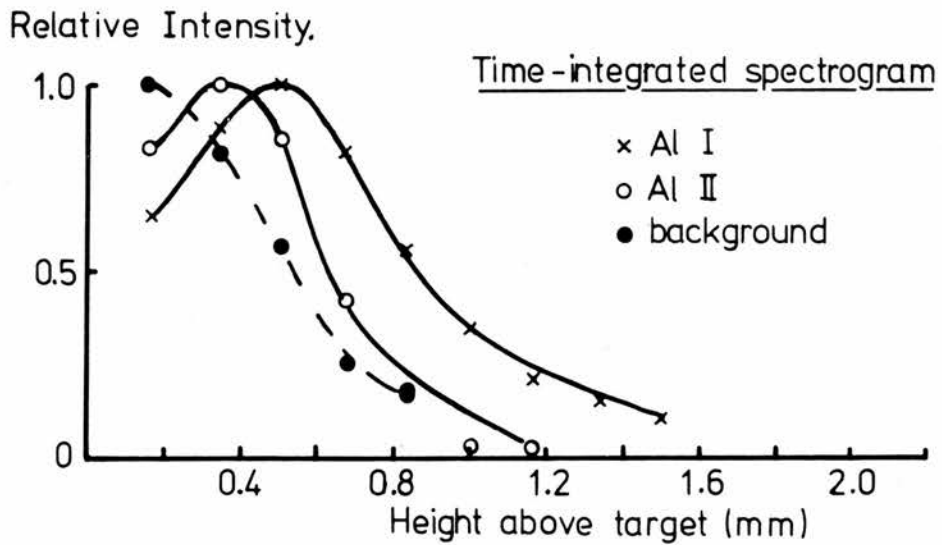


FIG 3.4 : TEMPORAL PROFILES OF Al LINES



(a) Spatial profiles in Q-spoiled plume



(b) Spatial profiles in RO-mode plume

FIG 3.5: SPATIAL PROFILES OF Al LINES

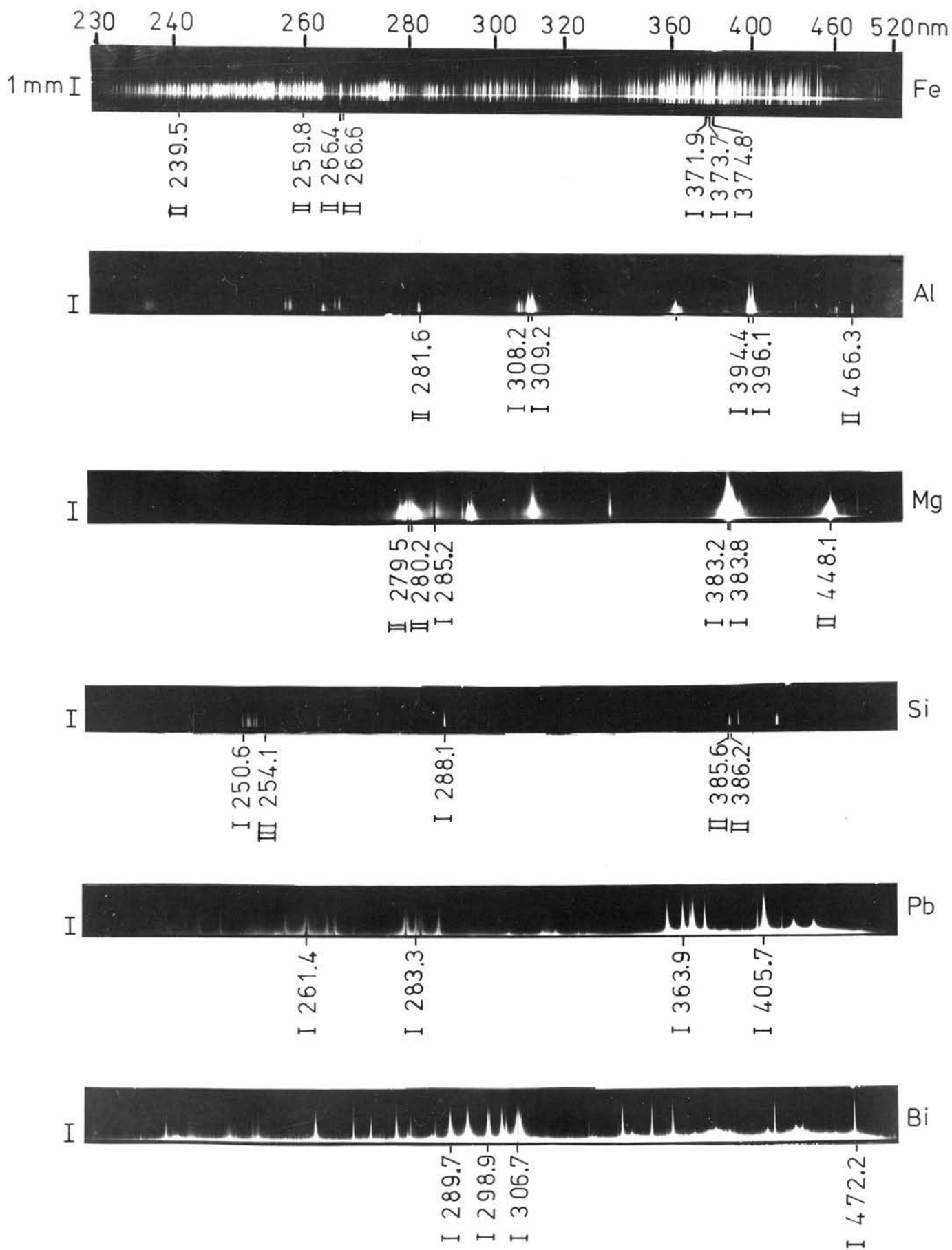


FIG 3.6: SPATIALLY-RESOLVED SPECTRA EMITTED FROM RO - MODE RUBY PRODUCED PLASMAS.

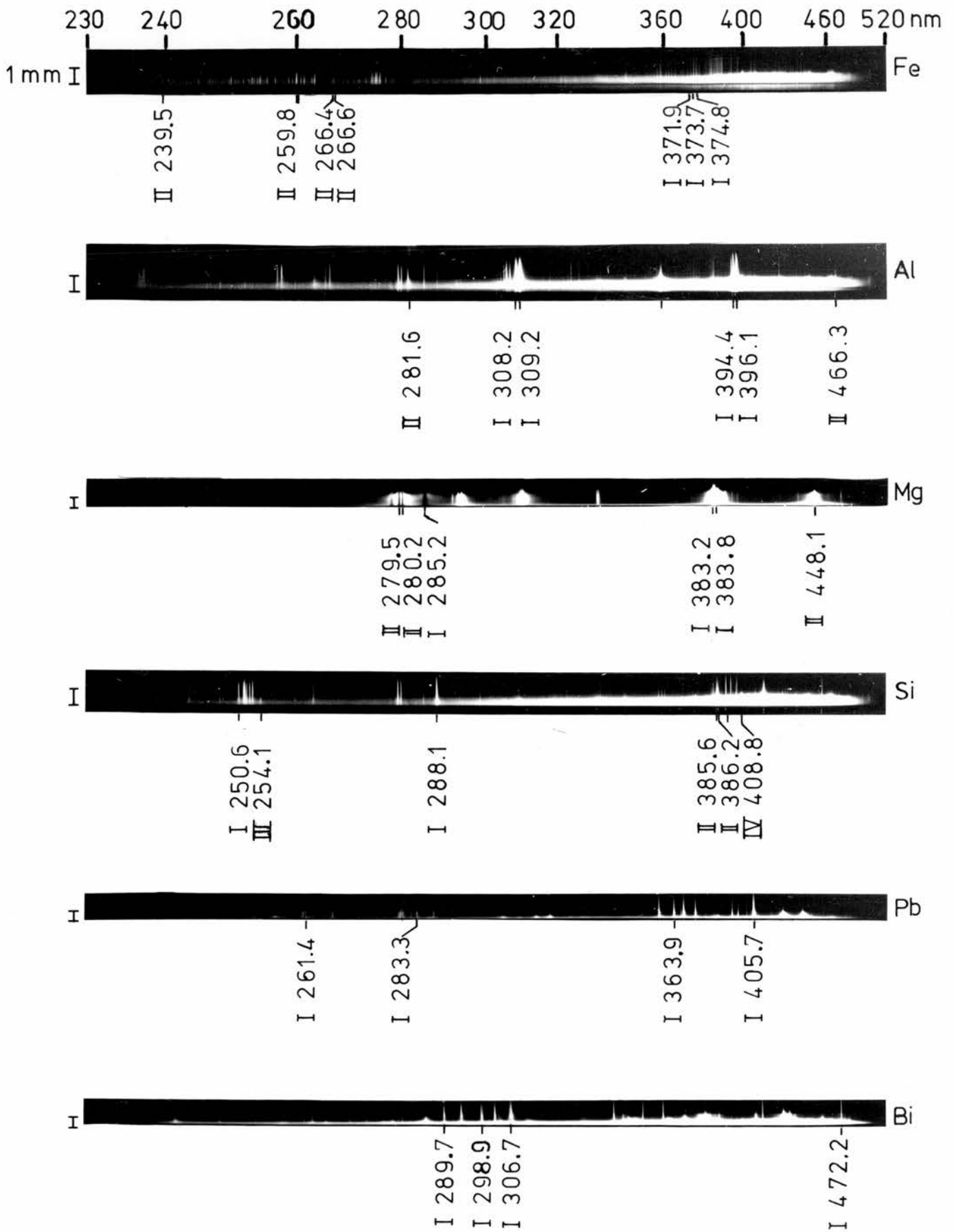
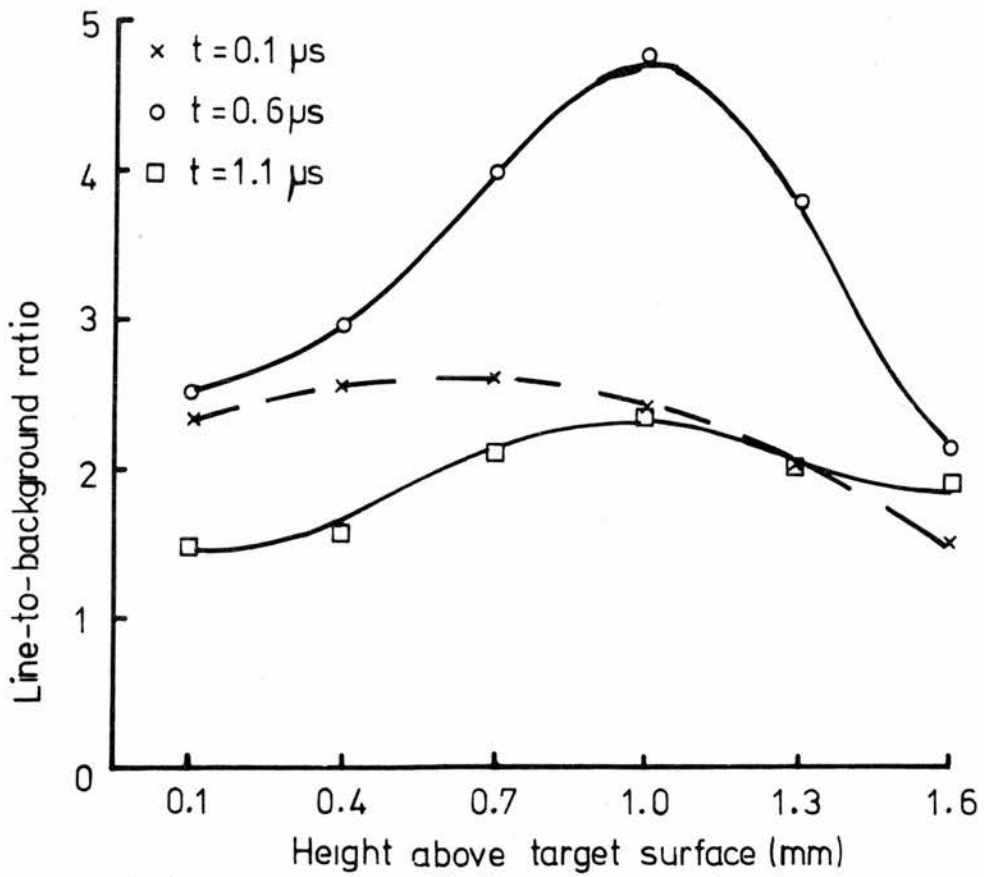
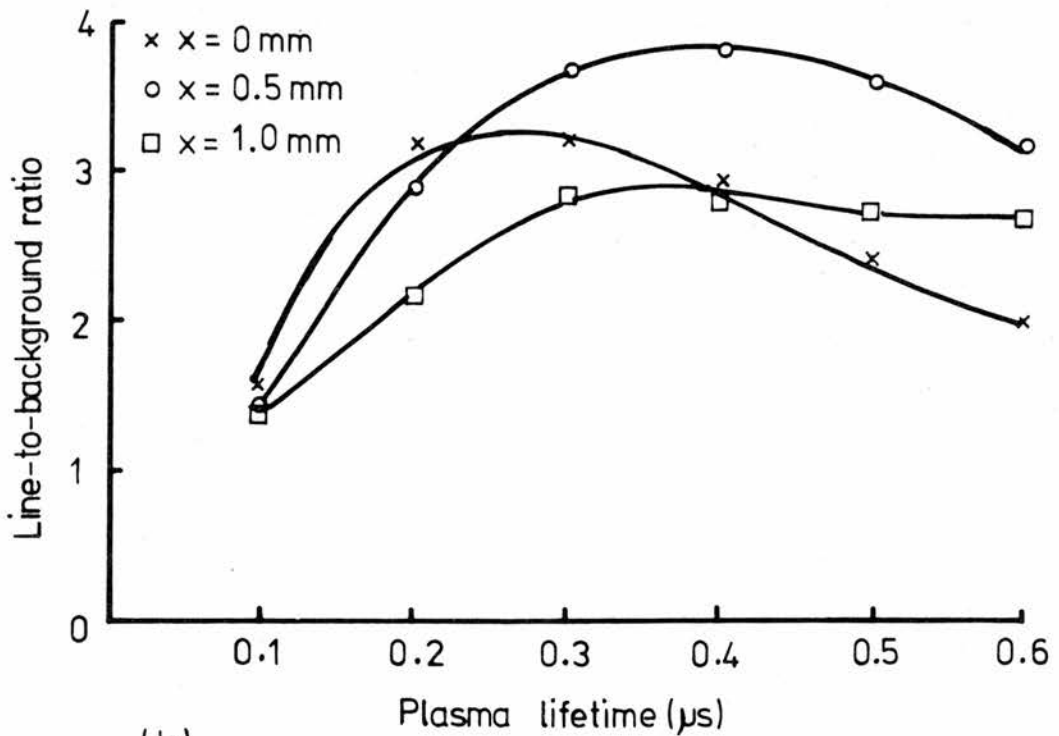


FIG3.7: SPATIALLY-RESOLVED SPECTRA EMITTED FROM Q-SPOILED RUBY PRODUCED PLASMAS.

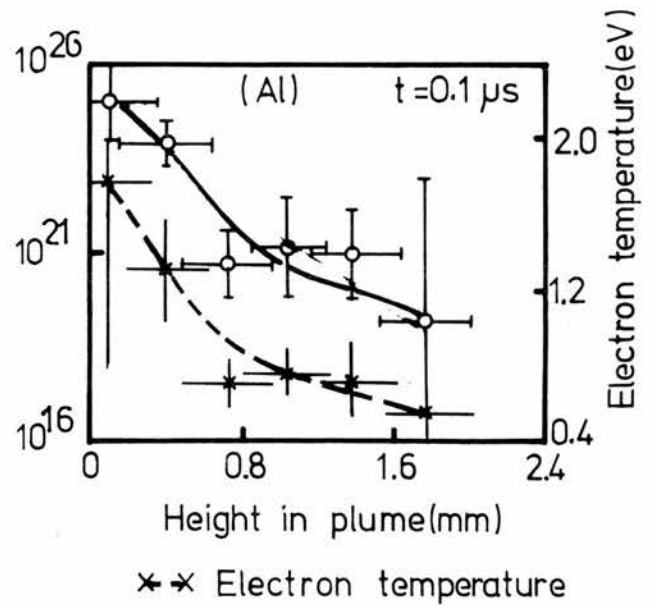
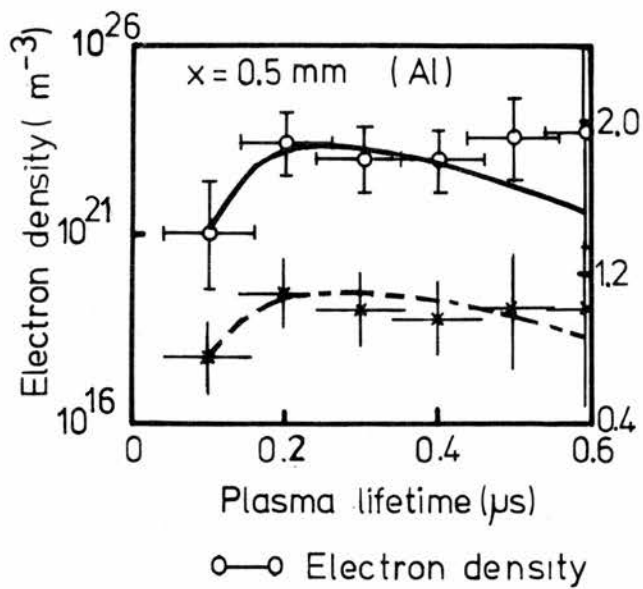


(a).

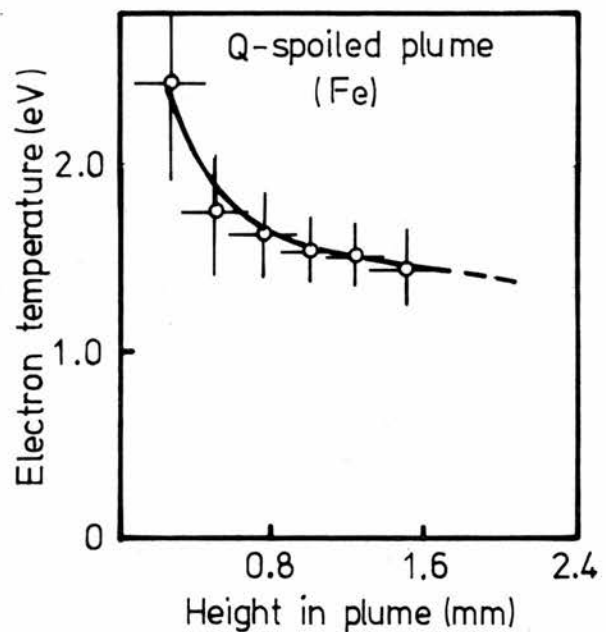
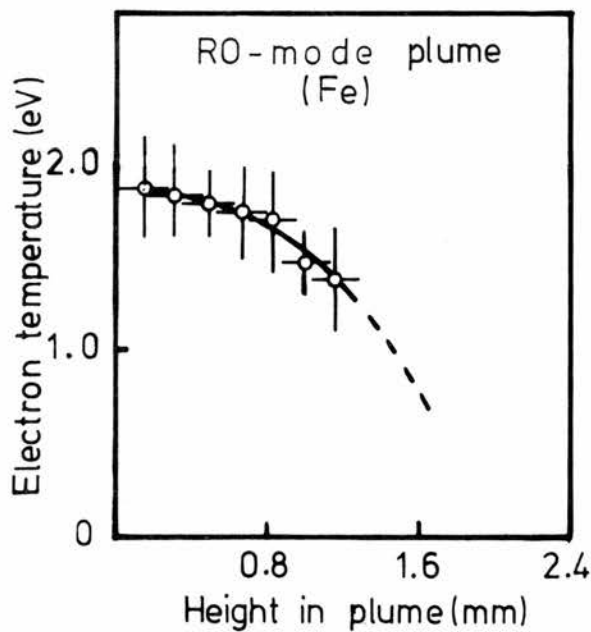


(b).

FIG 3.8 : LINE TO BACKGROUND RATIOS FOR Al I 395.6
vs (a) PLASMA HEIGHT and (b) PLASMA LIFETIME



(a) Time-resolved plasma parameters as a function of lifetime and height.



(b) Spatially-resolved electron temperatures as a function of height.

FIG 3.9 : TIME- AND SPATIALLY-RESOLVED PLASMA PARAMETERS.

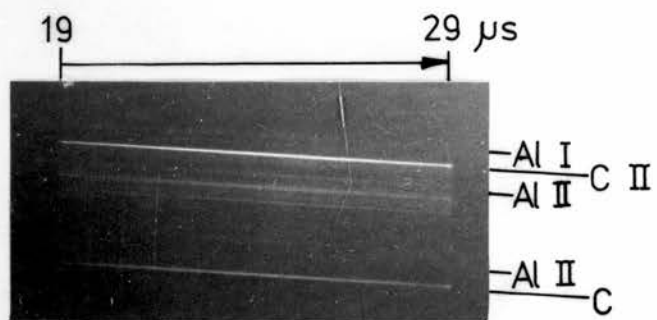
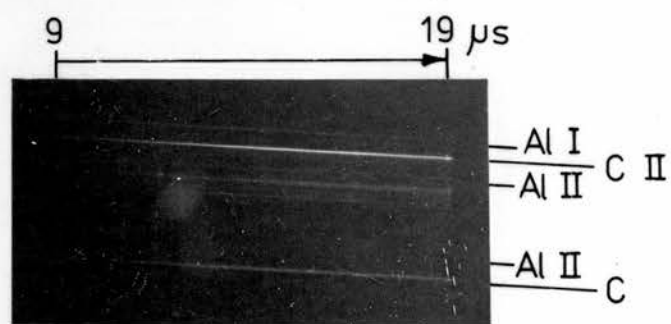
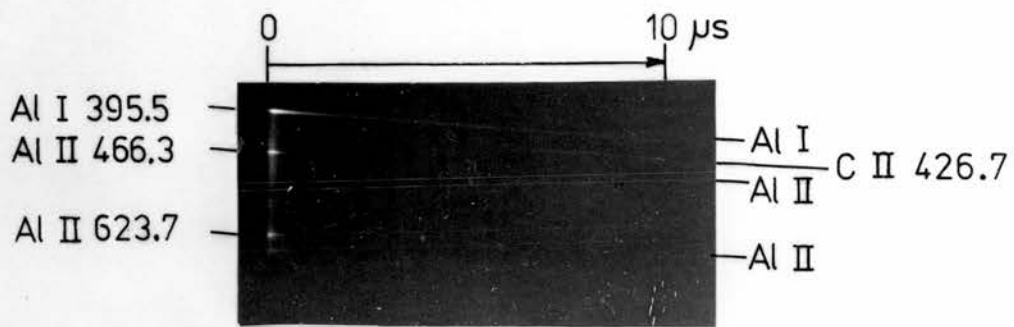


FIG 3.10: STREAK SPECTROGRAMS OF A SPARK-ASSISTED PLASMA.

CHAPTER 4

ELECTRO-OPTIC GATING OF THE RADIANT EMISSION FROM LASER-PRODUCED PLASMAS

4.1 INTRODUCTION

When high power radiation from a QS laser is focused on a solid target an expanding microplasma, with a lifetime of about 20 μs , is produced at the surface. Line radiation which is characteristic of the target is emitted from the plasma, together with a dense continuum. Often highly ionised species as well as atomic species are present in the plasma, resulting in a complex spectrum (see Chapter 3). Time-resolved studies of plasmas produced by Q-switched lasers have shown that spectral lines from the ionic and atomic species are emitted from the plasma in order of decreasing excitation potential (Chapter 3). The background continuum and lines from the multiply-ionised species are emitted early in the plasma lifetime. Singly ionised and atomic spectral lines are emitted and reach peak intensity at progressively later times than the continuum emission, and also have much longer lifetimes. There is also a spatial dependence to the plasma emission, with the continuum and multiply-ionised lines found close to the target surface and the singly-ionised and atomic lines peaking in intensity at respectively greater heights above the target. In Chapter 3 we have discussed measurements made of Al plasmas produced by a laser power density of 10^{13} W m^{-2} . These measurements show that at a height of 0.5 mm above the target the continuum emission peaked at 220 ns with respect to the leading edge of the laser pulse, whereas an Al II line peaked at 230 ns and an Al I line peaked at 330 ns.

The behaviour described above suggested that by temporally or spatially gating the plasma emission the continuum and ionic lines can be separated from the atomic lines, resulting in a simpler spectrum and an improvement in the line-to-background ratio of the atomic lines. This simplification of

the spectrum is often desirable in a spectroscopic study of laser plasmas where the high background and complexity of the spectrum can make line identification difficult.

In this chapter we describe a method of gating the plasma emission by using a Pockels cell operated between two parallel polarisers as an optical shutter. The optical shutter is interposed between the laser plasma and the spectral detector. With the shutter open, the plasma emission can reach the detector (but with some attenuation), with the shutter closed, no light can reach the detector. If the shutter is opened after the continuum and multiply-ionised emission has subsided, a spectrum is obtained which contains only singly-ionised and atomic lines. Gated spectra from Mg, Al and Fe plasmas are shown, and suggestions for future improvements to the technique are given. This work has been summarised by Watson and Maitland (1977).

4.2 THE POCKELS ELECTRO-OPTIC EFFECT

The phenomenon of electrically-induced birefringence in uniaxial crystals is known as the Pockel's electro-optic effect. The theory of the Pockel's effect is outlined here, as far as is required for an understanding of the use of a Pockels cell as an optical shutter. Only those aspects of the effect which apply to our use will be described. A fuller and more general description of the Pockels electro-optic effect can be found in Kaminow and Turner (1966), Adams (1968), and Ley et al (1970).

Some crystals which do not normally exhibit double refraction, can become birefringent when a d.c. potential is applied along one of the crystal axes. Crystals which belong to the tetragonal symmetry class exhibit this phenomenon. A typical example of this class of crystal is deuterated potassium dihydrogen phosphate (KD*P) which is used in the Pockels cell (Electro-Optic Developments, type PC105) used in the experiments described

in this thesis. Light waves which propagate through this type of crystal can only do so in two mutually perpendicular planes of electric vibration, due to the symmetry properties of the crystal. If the crystal is oriented so that the incident wavefront is normal to the principal axis (z-axis) of the crystal, the wave velocity parallel to the axis is the same for both planes of vibration. The principal axis is the only direction in the crystal for which this is true, and crystals of this type are called uniaxial. A uniaxial crystal in this orientation exhibits no double refraction and the orientation is designated as longitudinal z-cut. The crystal in the PC105 is oriented in this fashion (Fig 4.1a).

Light travelling in any direction other than that of the principal axis is polarised into two plane waves of different velocities. An index ellipsoid is defined which describes the refractive index change as the wave propagates through the crystal. The general equation of the index ellipsoid is given by

$$\frac{x^2}{\mu_x^2} + \frac{y^2}{\mu_y^2} + \frac{z^2}{\mu_z^2} = 1 \quad (4.1)$$

where μ_x , μ_y and μ_z are the principal refractive indices. Uniaxial crystals have two equal indices, $\mu_x = \mu_y$ and equation (4.1) becomes

$$\frac{x^2 + y^2}{\mu_x^2} + \frac{z^2}{\mu_z^2} = 1 \quad (4.2)$$

For waves vibrating in the xy plane the intersection of the index ellipsoid and the wavefront is a circle, defined by refractive index μ_x , which is normally referred to as the ordinary wave. When waves vibrate normal to the xy plane, the index is μ_z , and this wave is called the extraordinary wave.

On application of an electric field \vec{E} to the crystal, the index

ellipsoid can be written as

$$\frac{x^2}{\mu_x^2} + \frac{y^2}{\mu_y^2} + \frac{z^2}{\mu_z^2} + 2r_{41}(yz E_x + zx E_y) + 2r_{63} xy E_z = 1 \quad (4.3)$$

where r_{41} and r_{63} are the linear electro-optic coefficients of the crystal.

If this field is directed along the principal axis we have $E = E_z$ and

$E_x = E_y = 0$ and equation (4.3) becomes

$$\frac{x^2}{\mu_x^2} + \frac{y^2}{\mu_y^2} + \frac{z^2}{\mu_z^2} + 2r_{63} E_z xy = 1 \quad (4.4)$$

With light polarised along the x or y axis, the electrically induced birefringence is described by

$$\Delta\mu = \mu_x^3 r_{63} E_z \quad (4.5)$$

and the phase retardation of the incident wave is given by

$$\phi = \frac{2\pi}{\lambda_0} \mu_x^3 r_{63} V_z \quad (4.6)$$

where $\Delta\mu$ is the change in refractive index, λ_0 is the wavelength of the incident wave in free space, and V_z is the voltage applied along the z-axis of the crystal, of known length.

We see that on application of a voltage V_z , the incident light wave is phase retarded by an angle ϕ on travelling along the principal axis. We normally choose V_z that ϕ is 90° for a particular wavelength and crystal length z ; V_z is called the half-wave voltage for that wavelength. When the crystal is placed between parallel polarisers, the incident wave is plane polarised at the first polariser and passes through the crystal with no phase change, to emerge from the analyser in the incident plane of polarisation (Fig 4.1a). When a voltage is applied to the cell, the plane polarised wave is phase retarded through 90° , and can no longer emerge from the analyser (Fig 4.1b).

4.3 EXPERIMENTAL METHODS

The ruby laser was operated in the QS mode giving single output spikes

of 50 ns (FWHM) at a wavelength of 694.3 nm. The power density at the target was $9 \times 10^{13} \text{ W m}^{-2}$.

The active medium of the cell was a longitudinal z-cut crystal of KD*P mounted with ring electrodes at either end (Electro-Optic Developments, PC 105). The crystal was 25 mm long (z-axis) with a 10 mm aperture, the transmission range is 0.3 - 1.2 μm and the half-wave voltage was 6.0 kV at 1.06 μm . In operation the cell was mounted longitudinally (z-axis parallel to the optic axis of the system) between a pair of Glan-Taylor polarisers (Electro-Optic Developments, GTL 3) of 12 mm aperture and 0.3-1.25 μm transmission range. The light output from the plasma was collimated using a 150 mm lens, then passed through the polariser system and imaged onto the entrance slit of the spectral detector with another 150 mm lens.

The cell and polarisers were aligned such that the combined system functioned as an optical shutter. The shutter is normally open when no dc potential (HT) was applied along the cell. This is the condition for maximum transmission of light from the source to the detector. On applying a dc potential along the cell, no light is transmitted at a particular wavelength (which is dependent on the applied voltage) and for a small wavelength range on either side of this. With the system arranged in this manner, no light from the plasma can reach the detector until the dc potential is removed on applying a trigger pulse. By delaying the removal of the potential until a chosen time in the life of the plasma, the light output during the early part of the plume development can be prevented from reaching the detector. Thus a simpler spectrum is obtained in which the high intensity continuum and spectral lines from the multiply-ionised species are absent. For plane polarised light the minimum transmission of a single polariser is 87% and the crystal insertion loss is 4% giving a 27% attenuation of the beam transmitted through the shutter. The light transmitted from the plasma source through the optical

shutter is about 1/3 of that without the shutter. Thus, the effective aperture of the spectral detection system is about f/22. (compare with f/11).

The HT was applied to the cell from a high voltage step generator (Electro-Optic Developments HVP5/B). The dc potential (2-5 kV) was shorted to ground on applying a suitable trigger pulse to the generator. The trigger pulse was derived in the following way: the laser output pulse was monitored by a fast photodiode (EG & G, SD-100) at the laser head and the pulse was displayed on a CRO; a trigger output pulse which can be delayed with respect to the laser pulse can be derived from the CRO; this delayed trigger was fed to the trigger input of the Step Generator, and in this way the Pockels cell could be opened at any time with respect to the laser pulse.

Two different spectral detectors were used in these experiments. The first detector was a grating monochromator (Carl Zeiss Jena, SPM2) fitted with a photomultiplier tube (EMI, 9594 QUB) at the exit slit. The entrance and exit slit widths were both 40 μm . The PM tube was biased to 1.4 kV. The output was monitored across a 40 Ω load and the intensity-time profile of spectral line displayed on the CRO. The second detector was a quartz prism spectrograph (described in Section 2.2), with an entrance slit width of 40 μm . The spectra were recorded on Ilford LN photographic plates which were soaked in a sodium metabisulphite solution prior to developing in Kodak D.19 to effectively double the emulsion speed (Sec 2.3.1).

4.4 ALIGNMENT OF THE POCKELS CELL

The following procedure for the alignment of the Pockels cell and polarisers was adapted from Adams (1968). If anisotropic crystals are placed between polarisers and illuminated by strongly divergent light, patterns of isogyres and isochromatic curves are obtained. These patterns are useful in the alignment of a Pockels cell, but the theory of their occurrence will not be described here, and reference should be made to Adams (1968) or Longhurst (1967).

(1) The LMA is first aligned with respect to the spectrograph (Q24) in accordance with standard practice. A He-Ne laser is used to define the optical path between the LMA and the spectrograph slit.

(2) A ground glass screen is placed in front of the polariser to scatter the laser light, and an observation screen placed at the slit. The polarisers are mounted in the light path and adjusted by reflection until aligned with the optical axis of the laser. The analyser (second polariser) is rotated until the laser beam is extinguished.

(3) The Pockels cell is placed between the polarisers, and aligned with the optical axis of the system. A pattern of a dark cross on a background of concentric circles (Fig 4.1c) should be seen on the screen. This is the normal pattern seen for a uniaxial crystal. Rotation of the cell should not alter the pattern unless the crystal is not purely uniaxial. The dark cross is the isogyre and the concentric circles which may or may not be seen depending on the cell aperture, are the isochromatic curves. The arms of the isogyre indicate the planes of polarisation of the incident and the emergent beams (shown in the diagram) and show that no light will pass through the system in either the polariser or analyser plane. If the cell is properly aligned so that the principal axis of the crystal and optic axis of the system are parallel, the cross will be central in the field of view.

(4) A voltage is applied to the cell, and the patterns that are formed are those obtained with a biaxial crystal. Rotation of the cell will cause a cross shape like that in Fig 4.1d to form in the field of view. This shape is analagous to that for the uniaxial case. Rotating the cell through 45° will cause the isogyres to break up into hyperbolic segments (Fig 4.1e) bounded by the quadrants formed by the crossed polarisers.

(5) The analyser is rotated into alignment with the polariser. If the voltage along the cell is increased to the half-wave voltage for the wavelength of He-Ne light, the transmitted light will decrease in the centre

of the field of view and the final shape will be that shown in Fig 4.1f.

(6) If the voltage is removed, the crystal will revert to its uniaxial state but this time the polarisers are parallel. The final pattern is that shown in Fig 4.1g with an area of maximum transmission on the centre.

(7) The cell is now aligned to transmit light when no voltage is applied to the cell and to prevent transmission when a voltage is applied to the cell.

(8) The ground glass screen and viewing screen are now removed and two 150 mm lenses are placed in the light path. The first lens is positioned in front of the polariser to collimate the light coming from the laser-produced plasma, and the second lens, after the analyser to image the plasma on to the spectrograph-slit.

4.5 EXPERIMENTAL RESULTS

With the optical shutter (ie cell plus polarisers) positioned between the plasma and the detector, several experiments were conducted to characterise the operation of the optical shutter. The minimum delay between the incident laser pulse and shorting the dc potential to ground was measured on the CRO as 370 ns. This is the earliest time at which the optical shutter can be opened to allow light to pass.

Photomultiplier traces of the spectral output from a Mg plasma were recorded using the grating monochromator. Figure 4.2a shows the response of the line Mg I 517.8 nm with and without the optical shutter in operation. The upper trace shows the temporal response with the cell set for full transmission ie with no dc potential applied along the cell. The first peak corresponds to the continuum emission and lasts for about 220 ns (FWHM). The Mg I line (second peak) reaches its peak intensity about 720 ns after the continuum peak. The ratio of line peak to continuum peak is approximately 0.3:1. The lower trace shows the Mg I profile recorded when the shutter

was set to its minimum delay of 370 ns. Optimum extinction was obtained with the dc potential set to 2.95 kV. The continuum is effectively switched out leaving only that part of the profile which corresponds to the line emission.

The monochromator was replaced in the system by the Q24 spectrograph to study the wavelength and voltage dependence of the cell transmission. A white light source was projected through the system onto the spectrograph slit. A series of 1 sec exposures were made with the dc potential off (ie with the shutter closed for the whole exposure) and with it on at 2.0, 2.5, 3.0, 3.5 and 4.0 kV respectively (ie with the shutter open for the whole exposure). Each continuum was scanned in terms of optical density (D) against wavelength using a microdensitometer (Carl Zeiss Jena, GII). These traces are shown in Figure 4.2b. The density peak of the straight through beam (HT off) occurs at about 440 nm. With the HT on (ie shutter open) optimum extinction over the whole wavelength range is obtained at about 2.5 kV. At 4.0 kV maximum transmission is restored. The maximum extinction ratio is about 45:1. The manufacturers quoted maximum extinction ratio of 800:1 can only be obtained with a highly-collimated monochromatic beam.

Spectrograms were then taken of plasmas produced by irradiating nominally pure samples of Fe and Al. A series of spectrograms was recorded with the optical shutter opened at different points in the plasma lifetime between zero and 920 ns. These are shown in Figure 4.3. With the shutter open, the spectrograms show the region of dense continuum close to the target surface with the atomic and ionic lines extending above it. The spectrograms are progressively simplified on increasing the time at which the shutter is opened from 370 ns to 920 ns. For instance at 370 ns the Al continuum is removed entirely and at 520 ns the Al II 358.7 nm line is removed leaving only the Al I lines at 394.4 nm and 396.1 nm.

4.6 DISCUSSION

The Pockels cell (PC) shutter is potentially useful for spectroscopic analysis of plasmas produced by irradiating solid targets with a Q-switched laser. The PC shutter can be applied to qualitative analysis of laser plasmas, however some modification of this system would be necessary before it could be applied to quantitative analysis.

When qualitatively analysing a complex spectrum such as Fe (Figure 4.3), it is easier to identify the atomic species emission by using the PC shutter to simplify the spectrum. Using the PC shutter also removes the possibility of overlapping lines from different ionisation states. We have seen that lines from the higher ionisation states progressively disappear from the spectrum when we increase the time at which the shutter is opened. This behaviour can be used to identify the ionic state of an unknown or unfamiliar spectral line. The ion line Al II 358.7 nm, which appeared consistently in our Al plasmas but is not widely quoted in wavelength tables, was identified in this way.

We have seen that optimum extinction occurs only over a small wavelength range for a particular dc potential. The radiation transmitted by the system is about 1/3 of that entering it. Thus, the limit of detection for weak spectral lines would be worse than for plasma emission recorded without the use of the PC shutter. Therefore, in quantitative analysis, electronic detection of the spectral emission may be needed to compensate for the reduced sensitivity of the system. The intensity of the spectral emission could be increased by increasing the laser irradiation and producing a higher energy plasma. However, this would also enhance emission of lines from highly-ionised species and add to the complexity of the spectrum, thereby increasing the need for a PC shutter. The cell we used allowed the emission to pass after a chosen time, but was not designed to cut-off the emission again after a certain time had elapsed. Using a cell which could be

opened and closed at predetermined times, would allow a transmission "window" of duration Δt to be set at any given time in the plasma life. Thus the detector would be exposed to emission of the same duration Δt occurring at a chosen point in the plasma lifetime. Time-resolved laser microanalysis could then be carried out using spectral intensity ratios calculated for the same point in time and for the same element of time Δt .

4.7 CONCLUSION

A Pockels cell mounted between parallel polarisers can be operated as an optical shutter and used to separate the high intensity background and ionised species emission in laser-produced plasmas from the atomic species emission. The technique has a potential application in the study of Q-switched laser plasmas. We have demonstrated the use of the shutter in qualitative laser microanalysis, where the simplification of the spectrum makes line identification easier. However in quantitative studies of laser produced plasmas some modification of the system we used is required. The large light loss incurred in using the shutter should be compensated for and the Pockels cell which we used substituted for one which would allow a transmission "window" of variable duration to be set at any desired point in the plasma lifetime. Intensity ratios calculated from time-resolved spectra could then be used to calculate element concentrations and electron densities, with an improved confidence in the results.

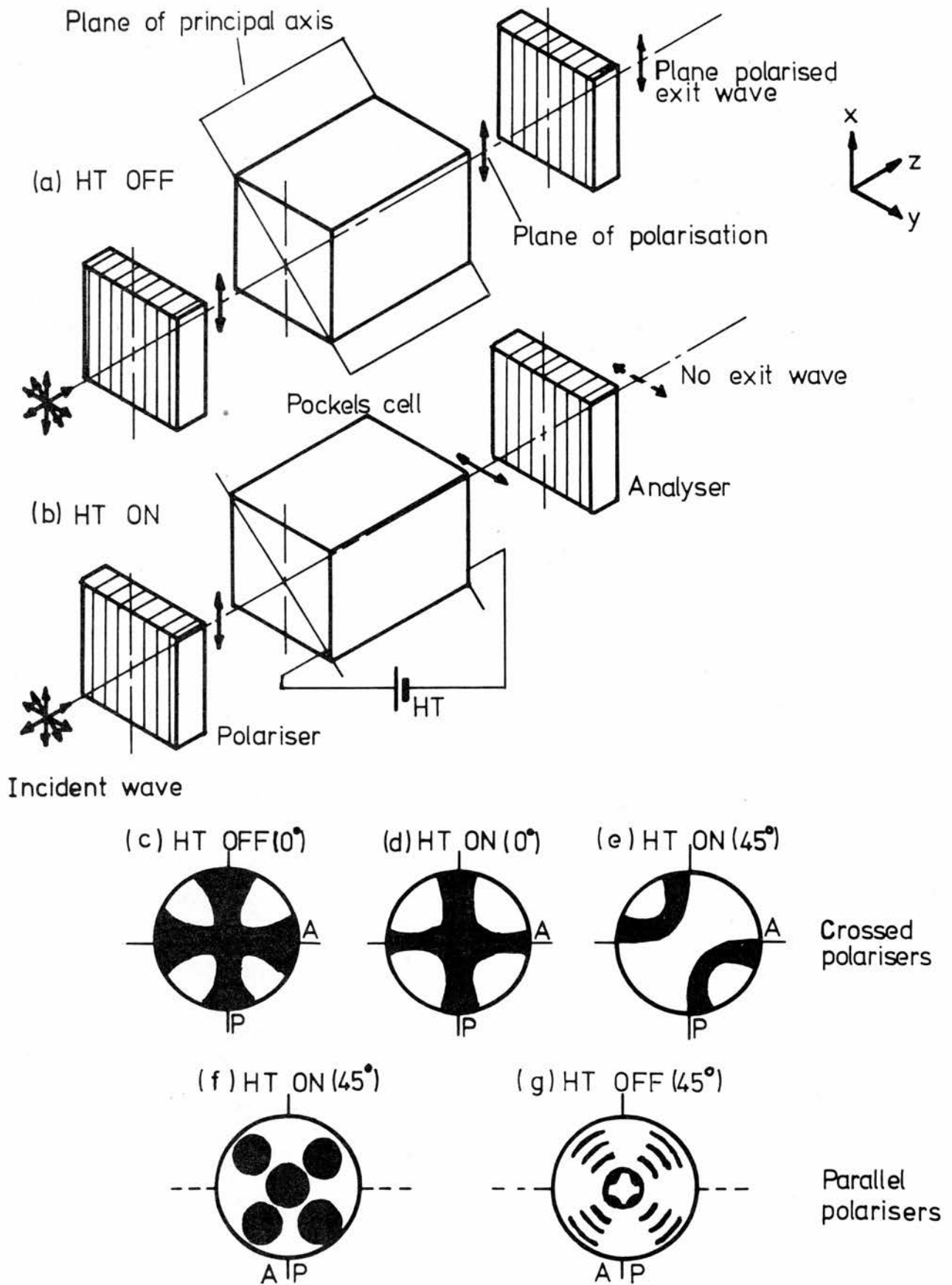
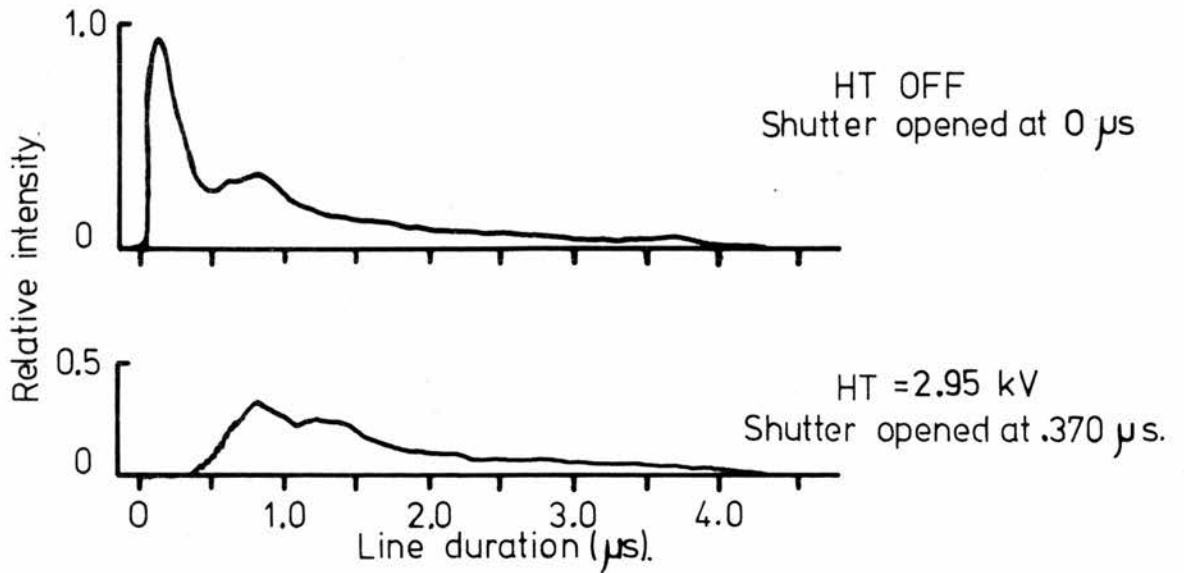
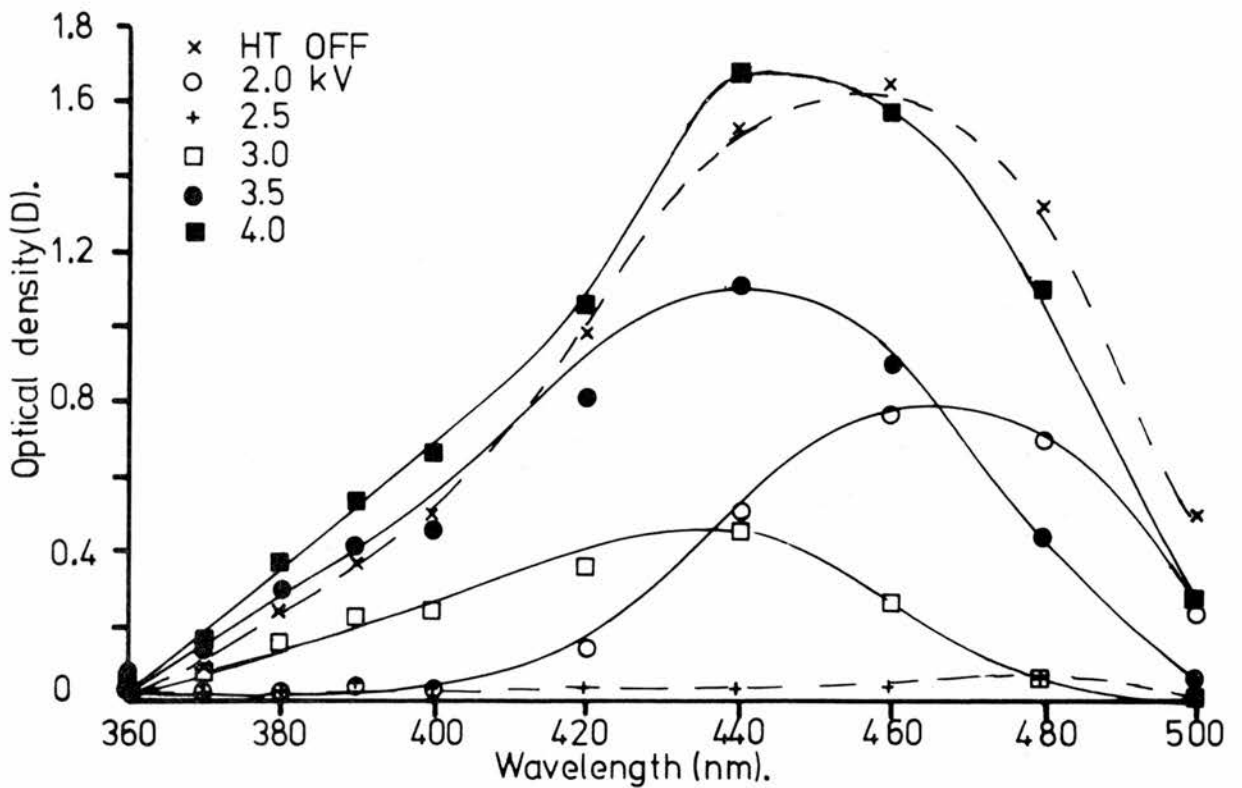


FIG 4.1: DETAILS OF POCKELS CELL OPERATION.



(a). Temporal profile of Mg I 517.8 with & without optical shutter in operation.



(b). Transmission of Pockels cell vs. wavelength for increasing d.c. potential (HT).

FIG 4.2 : CHARACTERISTICS OF POCKELS CELL OPERATION.

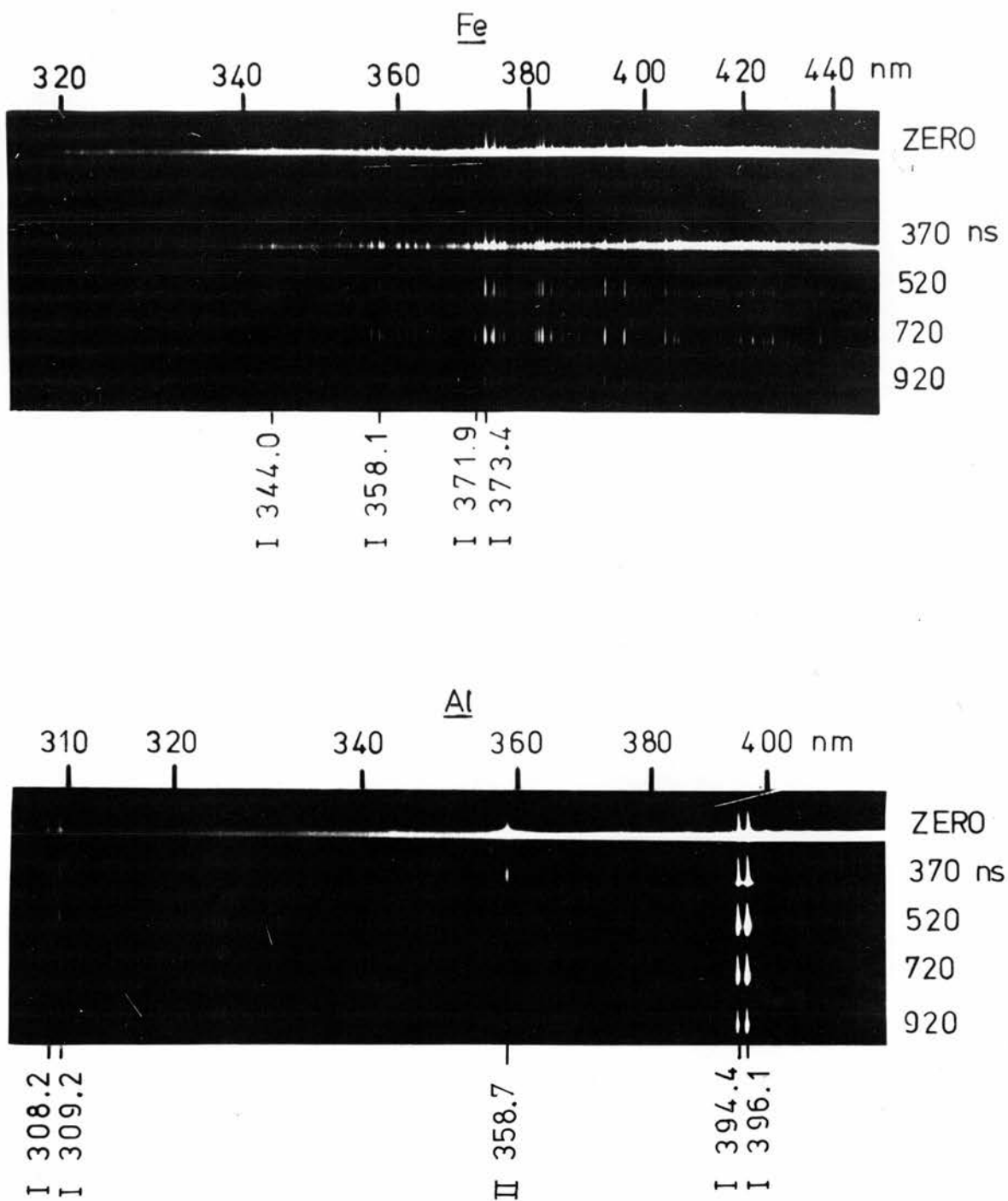


FIG 4 .3 :SPECTROGRAMS OF Fe & Al TAKEN THROUGH THE POCKELS CELL ARRANGEMENT,THE TIMES SHOWN ARE THE DELAYS BETWEEN THE LASER PULSE LEADING EDGE & OPENING THE OPTICAL SHUTTER.

QUANTITATIVE SPECTROCHEMICAL ANALYSIS OF STEEL STANDARDS5.1 INTRODUCTION

Having studied the spectral emission from laser-produced plasmas in some detail (Chapters 3 and 4), we now report on the use of Laser Micro-Spectral Analysis (LMSA) to determine the concentration of minor constituents in steel samples. In particular, we compare the various results obtained using each of the four basic modes of target excitation, viz, relaxation oscillator (RO) mode laser, with and without auxiliary excitation and Q-switched (QS) mode laser, with and without auxiliary excitation. Examination of the spectra produced using the four excitation modes reveals some differences between them. Enlarged portions of steel spectrograms, in the spectral regions around 267 and 426 nm, are shown in Fig 5.1 for each mode. The spectra produced by the spark-assisted modes are sharper and more dense (optical density) than for laser sampling on its own. The spectra from the unsparked plumes are diffuse and very weak in some cases: for instance, the FeI 429.4 line is difficult to detect in the unsparked RO plume, but is strong in the spark-assisted RO plume. A feature of the spark-assisted plumes is the presence of strong molecular bands and lines from the carbon electrode (eg CN388.3 and CII 426.7) which can cause interference problems in some cases. When spark excitation is used a background continuum is present due to black body radiation emitted from the hot electrode tips, and is strongest for wavelengths greater than 300 nm.

From Sec 1.3.5, the log intensity ratio of two spectral lines emitted by different elements (denoted, respectively, by A and R) in a plasma is related to the log ratio of their population densities in the plasma by (eqn 1.64)

$$\log \frac{J_{pq}(A)}{J_{mn}(R)} = \log \frac{N(A)}{N(R)} + K_o, \quad (5.1)$$

where K_0 is a constant for a given pair of spectral lines λ_{pq} (A) and λ_{mn} (R), emitted at a given temperature T. If the log intensity ratio (y) is plotted against the log concentration ratio (x) for a number of spectroscopic standard samples, we can apply linear regression analysis (App C) to the data to obtain a calibration (or working) curve of the form

$$y = ax + b, \quad (5.2)$$

where a is the gradient and b is the intercept. Comparison of eqns (5.1) and (5.2) shows that, in the ideal case, the working curve has an intercept of K_0 and a gradient of one. A gradient of one implies that the spectral intensity ratio is a function only of element concentration and is not influenced by preferential excitation or vaporisation, self-absorption, the presence of background continuum or by the choice of spectral line pair. From the calibration curve, the log concentration ratio (x) can be estimated from a measurement of the log intensity ratio (y).

We should note that an equation of the form of (5.2) is normally used to determine the dependent variable (y) from a measured value of the independent variable (x), and it appears that we should have plotted the regression line of x on y to enable us to estimate the log concentration ratio from the log intensity ratio. However, the regression line given by eqn (5.2) was constructed from known values of x, and it is in this form that it must be used. The alternative regression line of x on y, would not give the same values of a and b as those obtained by the line of y on x (eqn 5.2), unless there were perfect correlation between y and x (ie a coefficient of determination, r^2 , of one).

In the following working curves, the analysis elements are Si and Cr, and the reference element is Fe.

5.2 EXPERIMENTAL DETAILS

The low alloy steel standards (Bureau of Analysed Samples Ltd., Types

SS401 to SS404 and SS406 to SS410) contained Si in the concentration range 0.08 to 1.07% and Cr in the range 0.08 to 3.00%. The range of standards were sampled using each of the four modes of target excitation. The spectra from each excitation mode were recorded on separate photographic plates and a calibration spectrum (using SS410) was included on each plate.

The ruby laser was operated in both the RO and QS modes, at respective power densities of $1.8 \times 10^{11} \text{ W m}^{-2}$ per spike and $9 \times 10^{13} \text{ W m}^{-2}$. With auxiliary excitation, the spark parameters were 2.5 kV, 2.0 μF and 60 μH , the electrodes were set with a point-to-point spacing of 1.0 mm and were positioned 1.2 mm above the target. The two-step method of spectrograph illumination (Sec 2.2.1) was used to image the plasma onto the slit; this method yields spectral lines which are uniformly dense over their entire length. The spectrograph aperture was f/15 and the slit width was 25 μm for all excitation modes except unsparked RO, for which the aperture was f/11 and the slit width was 30 μm . For the spark-assisted modes, the photographic plates (Ilford LN) were developed in Kodak D.19 and for the unsparked modes, the sodium metabisulphite/D.19 combination (Sec 2.3.1) was used.

The experimental arrangement is shown in Fig 5.2, with the slit imaging system represented by only one UV achromat.

5.3 EXPERIMENTAL RESULTS

Working curves for Si and Cr were constructed for the spark-assisted RO and QS modes using the following line pairs: Si I 251.6/Fe I 251.8, Si I 288.1/Fe I 282.3 (Figs 5.3 to 5.6) and Cr I 425.4/Fe I 428.2, Cr I 428.9/Fe I 429.4 (Figs 5.7 to 5.10). A computer graph plotter (Hewlett and Packard type HP 9862A) was used to plot the data and apply a linear regression analysis. A further set of working curves for Cr were plotted for all four excitation modes (Fig 5.11) using a pair of singly

ionised lines (Cr II 267.7/Fe II 266.6). Since the spectra emitted from the unsparked RO mode plasma were so weak, the working curve for this mode was constructed over a reduced concentration range.

All the working curves presented above were derived using intensity ratios for which no allowance was made for the presence of the background continuum. Each point on the working curves is a mean of three estimates of the log intensity ratio, unless stated otherwise. The vertical error bars correspond to \pm one standard deviation from the mean, and the horizontal error bars correspond to the precision on the known concentration ratios. The working curves presented in Figs 5.3 to 5.11 were derived by applying linear regression analysis to the plotted data. Using the general equations of regression summarised in App C, we calculated the regression coefficient (gradient) a , and the regression intercept b , together with their respective standard errors α_a and α_b , the coefficient of determination r^2 , and the standard error α_{yx} , of the regression line of y on x . As a measure of the error in the log concentration ratio \hat{x} determined from the log intensity ratio y , the standard error of the log concentration ratio was estimated from equn (C.16),

$$\text{ie } \alpha_{\hat{x}} = (\alpha_{yx}/a) \{m^{-1} + n^{-1} + (\hat{y}-\bar{y})^2/a^2 [\Sigma x^2 - (\Sigma x)^2/n]\}^{1/2} \quad (5.3)$$

The standard error of \hat{x} estimated by eqn (5.3) is a minimum at $\hat{y}=\bar{y}$ (ie at $\hat{x}=\bar{x}$) and increases towards the extremities of each line. The regression parameters are tabulated in Figs 5.12 and 5.13.

5.4 DISCUSSION

All the working curves which were obtained using LMSA, have gradients of less than one (see Figs 5.12 and 5.13). In all cases the largest gradients were obtained with the spark-assisted RO mode, no matter which line pair and analysis element were used. A gradient of less than one implies that preferential emission of one species in favour of another is occurring in

the plasma. In this case the implication is that the Fe species are emitted in preference to Si or Cr. The QS mode plasma appears to suffer most from this problem. Application of spark-excitation to the RO and QS mode plasmas results in an increase in the gradients of the respective working curves. Since we assume (Chapter 1) that the spark has no effect on target sampling and acts only as a source of secondary excitation, it appears that the spark is effective in increasing the overall light emission from the RO and QS mode plasmas. Spark excitation has the greatest effect on the RO mode plasma (a gradient increase of 0.46 to 0.56) and the least effect on the QS mode plasma (0.28 to 0.30) and the reason for this may lie with the time-scale of the application of the spark. We saw from the time-resolved spectroscopy of QS plasmas (Chapter 3) that, since the spark is applied so late in the laser-target interaction process (about 3 to 5 μ s after the plasma is produced) the plasma plume has decayed to the point where very few atoms of the target species are left. The main effect of the spark, in this case, is to excite carbon atoms from the electrodes and to produce the molecular, cyanogen bands. For the spark to have an effect on the target species of a QS plasma, excitation would need to be applied sooner than is possible with self-initiation. With the RO mode laser, the plasma has a lifetime of about 100 to 200 μ s and the spark has time to act on a plasma which is in the early stages of formation, and hence can effectively excite the target species in the plasma.

Since working curves are normally used to determine the concentration of the minor constituents in analysis samples, the accuracy of the log concentration ratio is a useful parameter by which to compare the various target sampling modes (Figs 5.12 and 5.13). The greatest accuracy of the log concentration ratio (smallest $\alpha_{\hat{x}}$ (min)), the largest coefficients of determination (r^2) and the smallest error on the regression line (α_{yx}) were all obtained using the spark-assisted RO mode of operation, regardless of

choice of line pair and analysis element. The working curves produced using the spark-assisted QS mode were consistently poorer in all of the above aspects. The working curves for Cr (Figs 5.7 to 5.10), although having smaller gradients than those of Si (Figs 5.3 to 5.6), give a better accuracy of the log concentration ratio owing to the smaller spread on the plotted data.

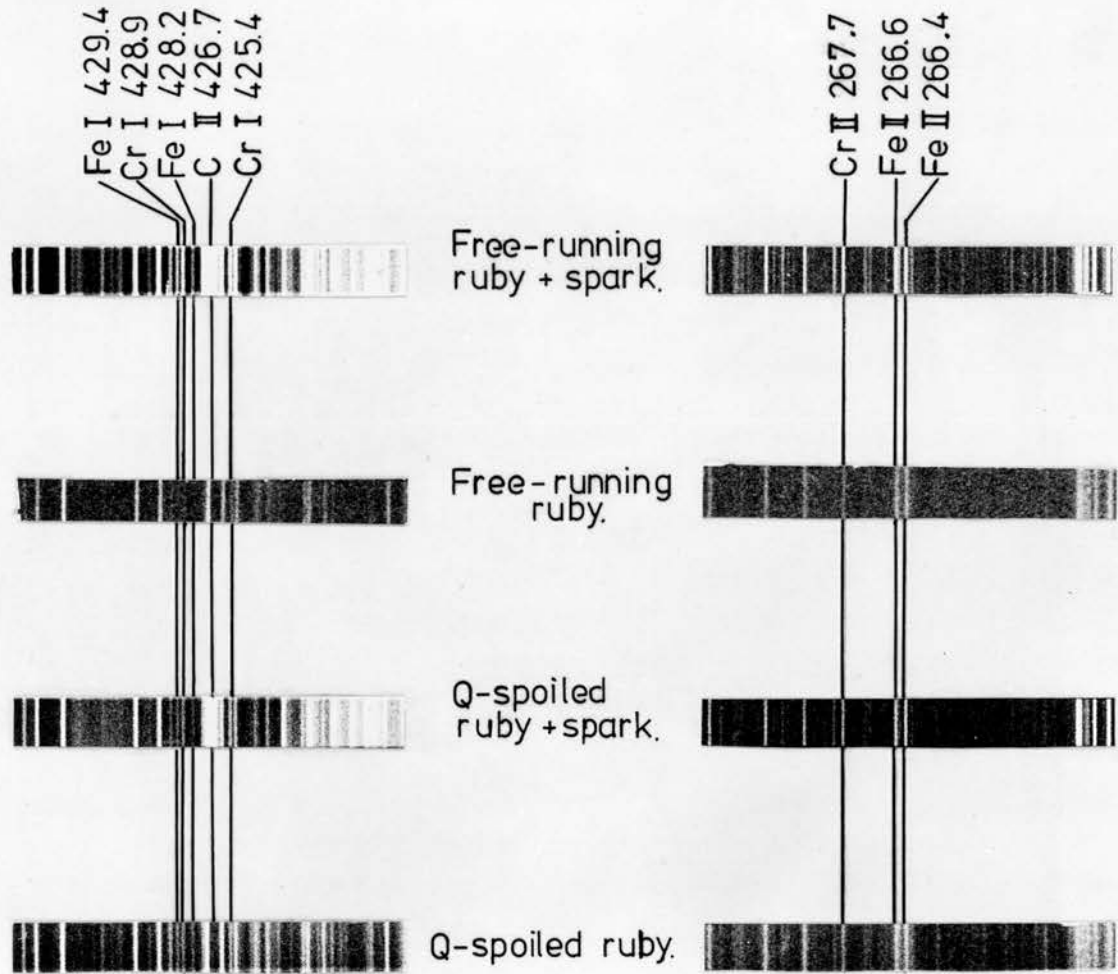


FIG 5.1 :TYPICAL SPECTROGRAMS USED IN THE QUANTITATIVE ANALYSIS OF STEELS.SPECTROGRAMS ARE SHOWN FOR DIFFERENT CONDITIONS OF PLUME EXCITATION.

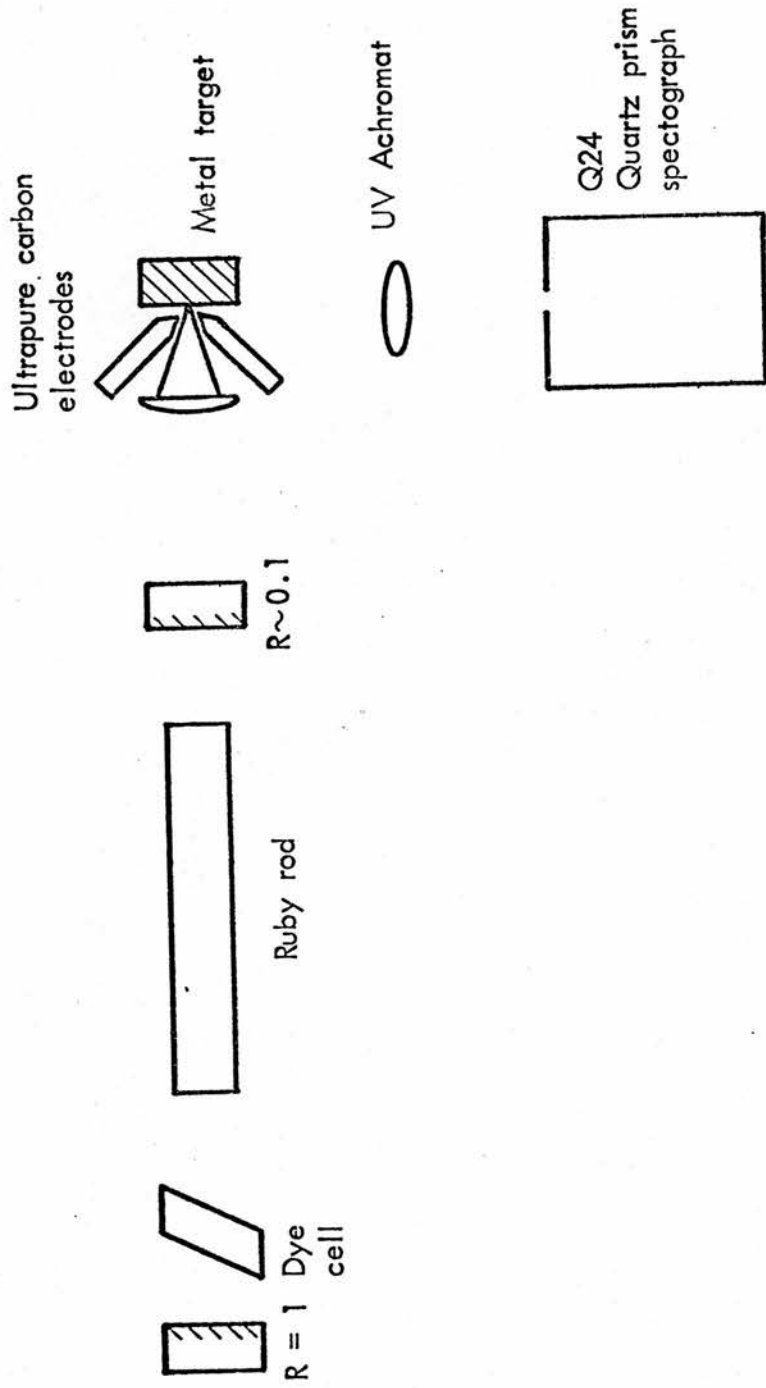


FIGURE 5.2: EXPERIMENTAL ARRANGEMENT

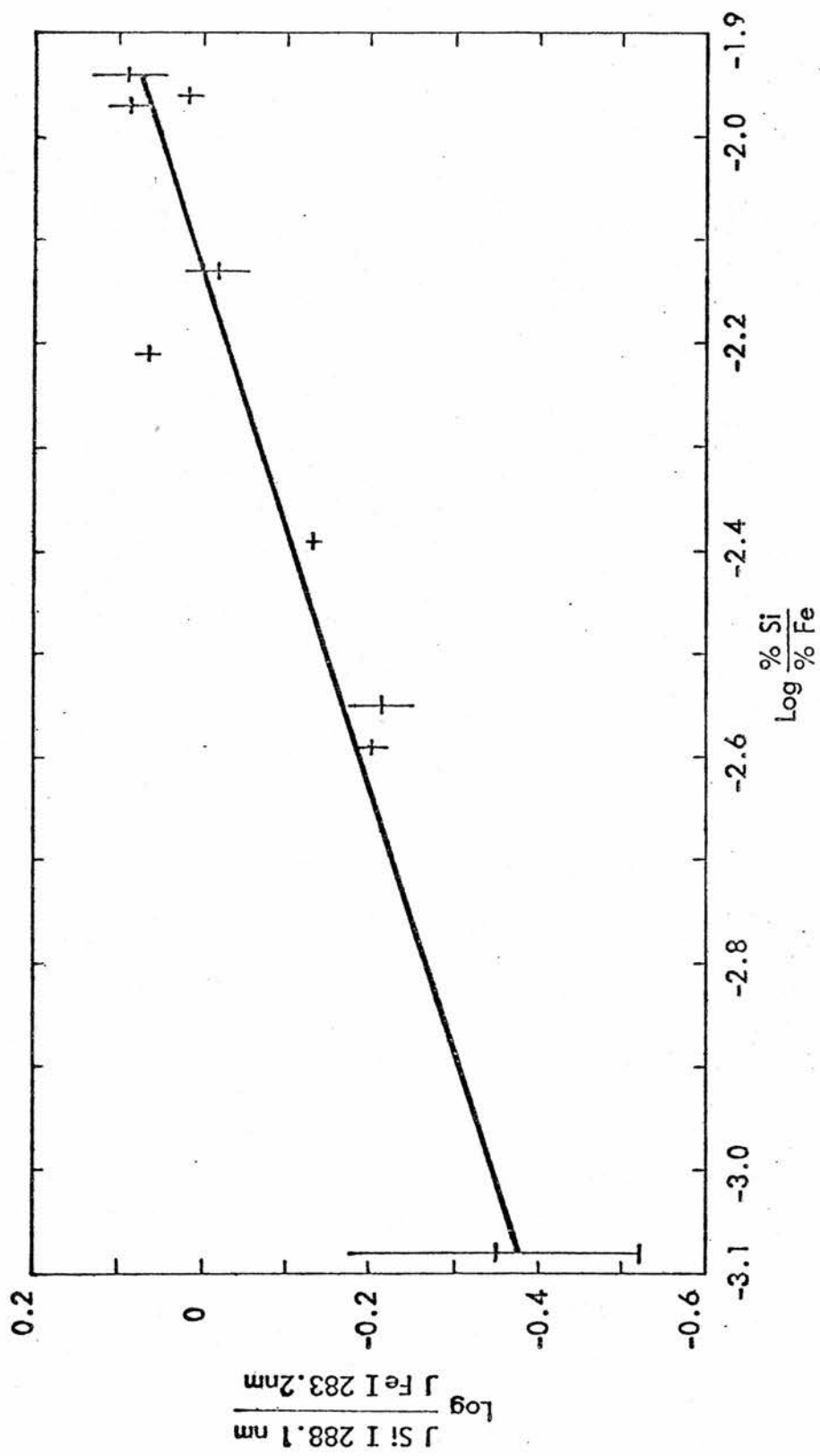
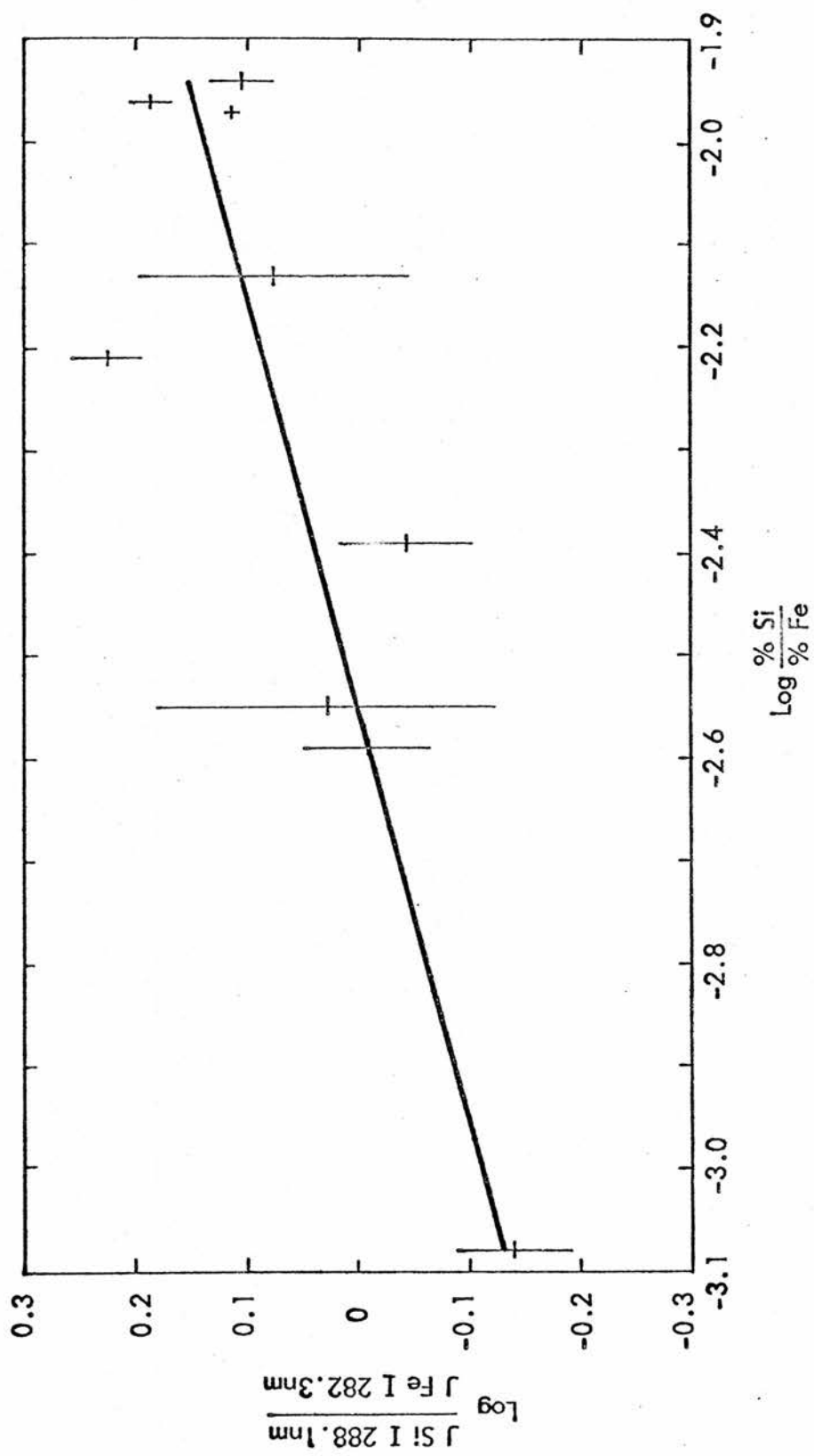
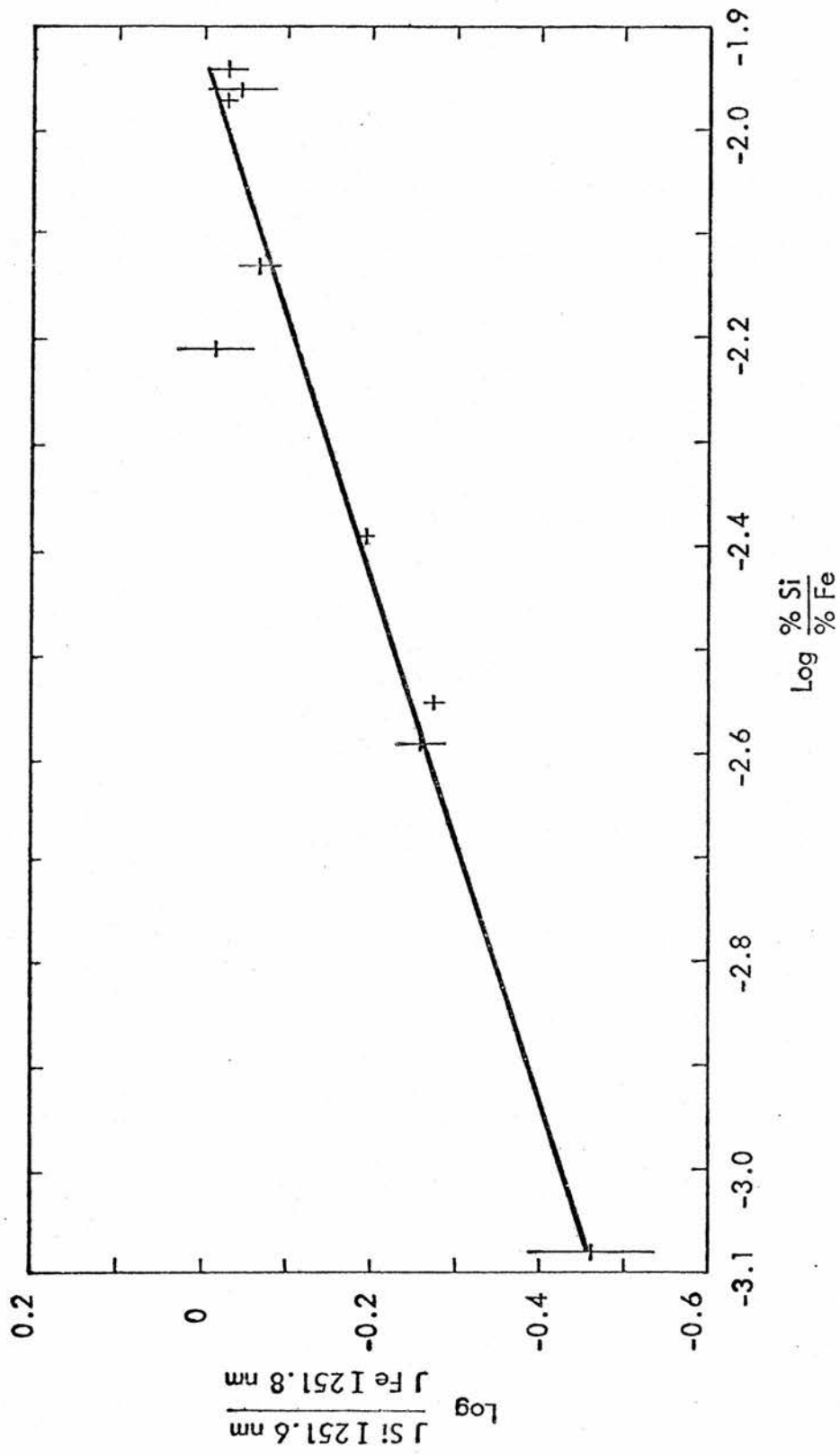


FIGURE 5.3: WORKING CURVE FOR SILICON USING A RUBY LASER OPERATED IN RELAXATION MODE WITH AN ANCILLARY SPARK



**FIGURE 5.4: WORKING CURVE FOR SILICON USING Q-SWITCHED RUBY LASER
 WITH ANCILLARY SPARK**



**FIGURE 5.5: WORKING CURVE FOR SILICON USING A RUBY LASER OPERATED
IN RELAXATION MODE WITH ANCILLARY SPARK**

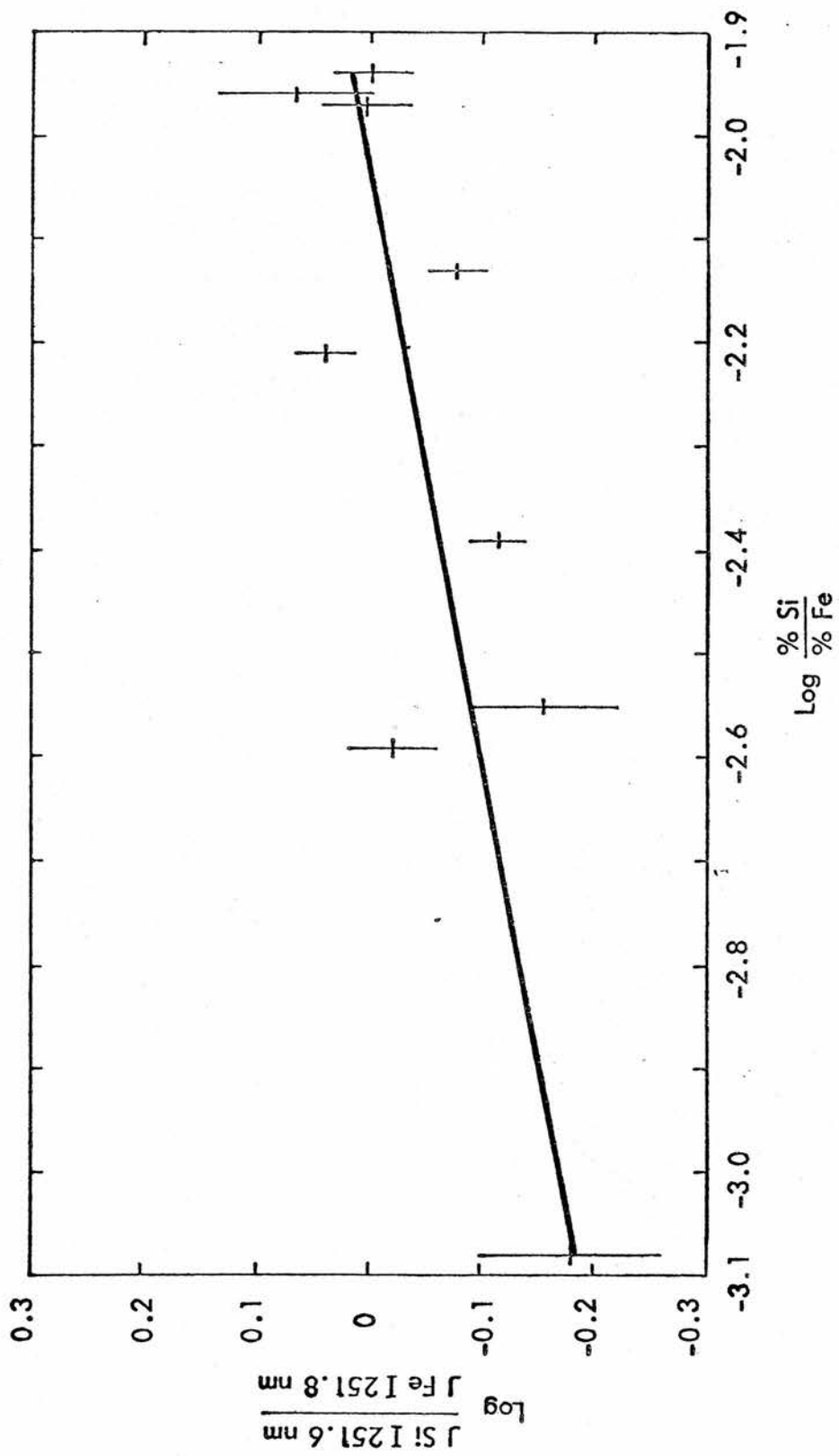


FIGURE 5.6: WORKING CURVE FOR SILICON USING Q-SWITCHED RUBY LASER WITH ANCILLARY SPARK

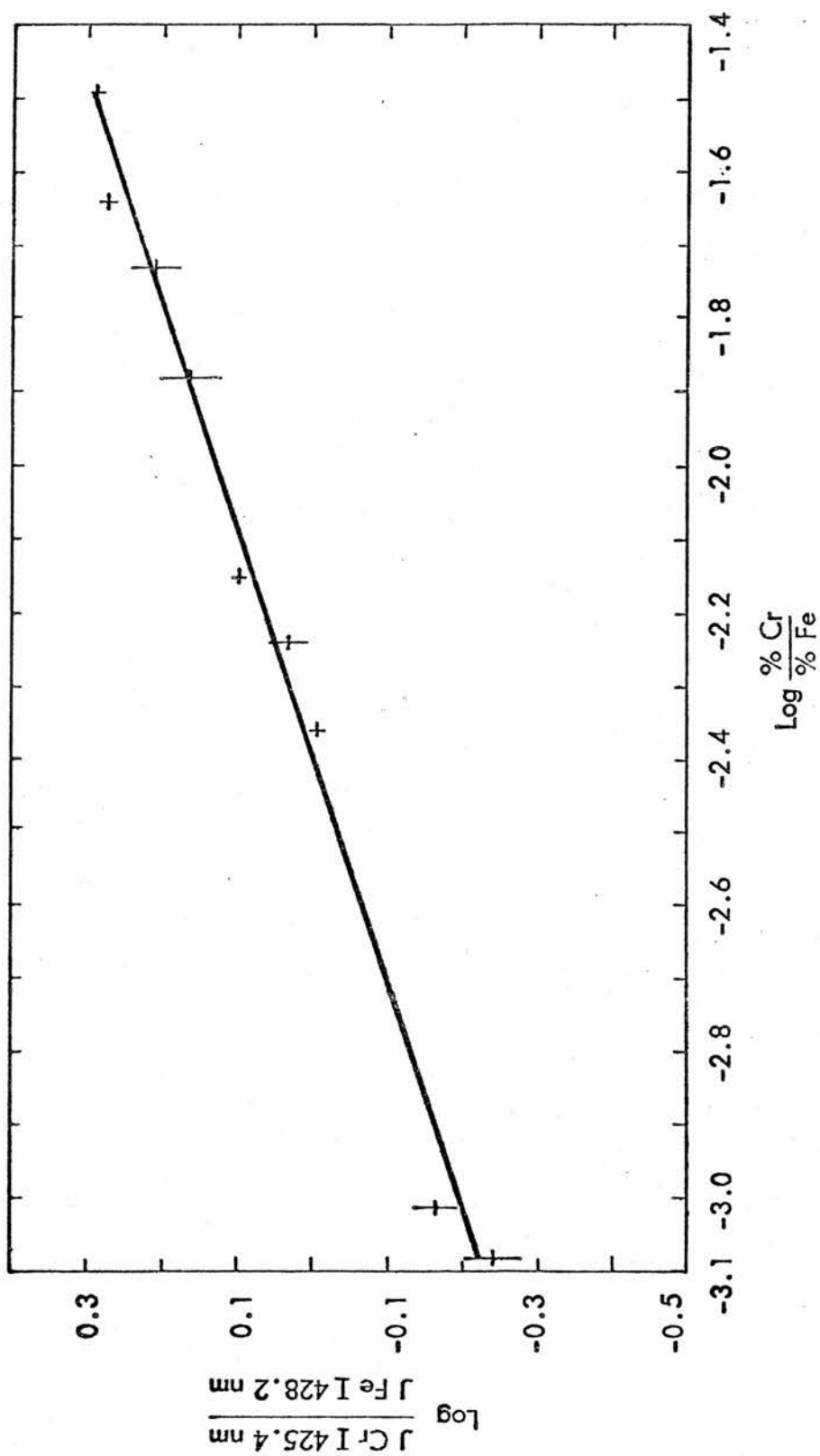


FIGURE 5.7: WORKING CURVE FOR CHROMIUM USING A RUBY LASER OPERATED IN RELAXATION OSCILLATOR MODE WITH ANCILLARY SPARK

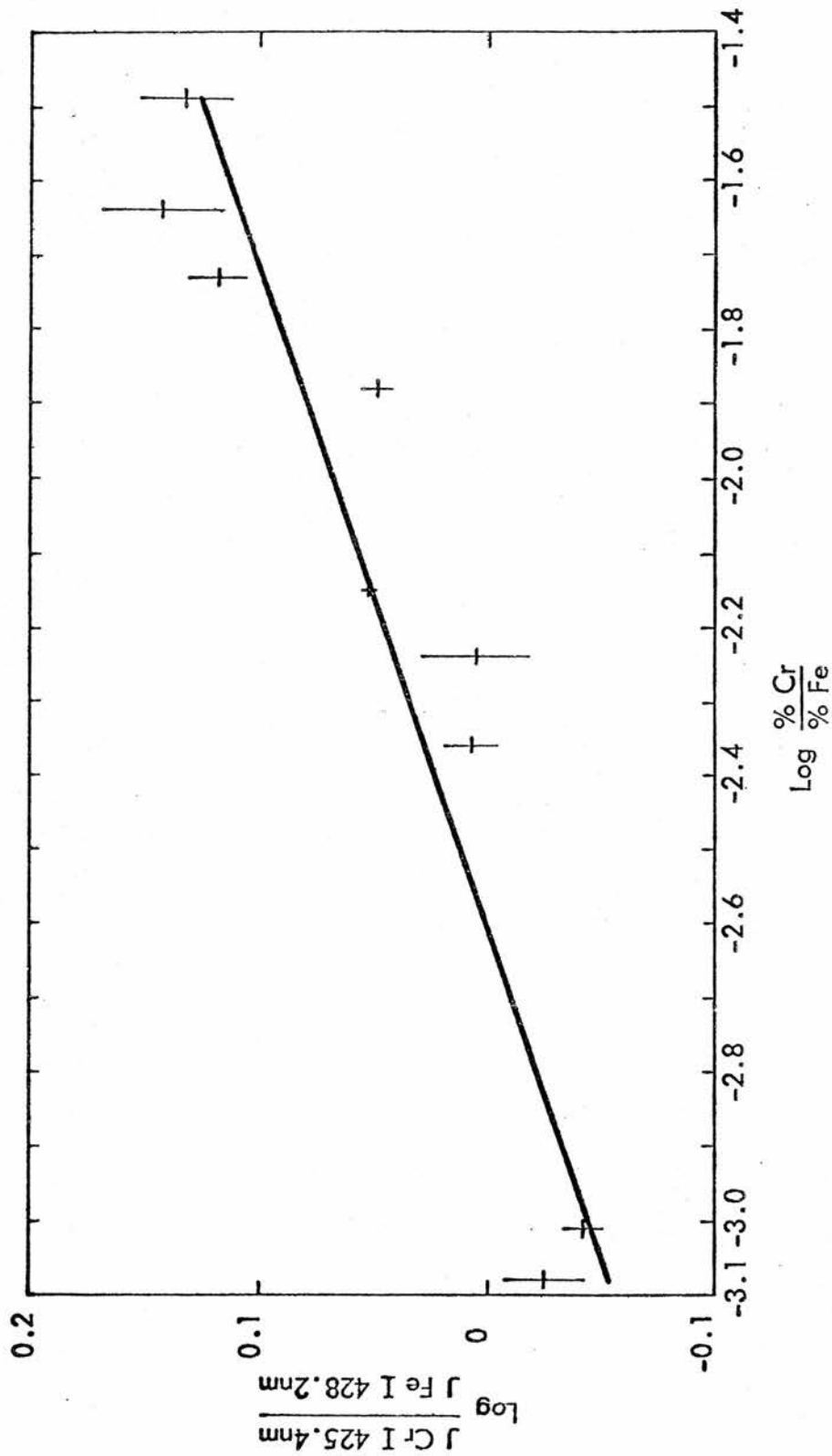


FIGURE 5.8: WORKING CURVE FOR CHROMIUM USING A Q-SWITCHED RUBY LASER WITH ANCILLARY SPARK

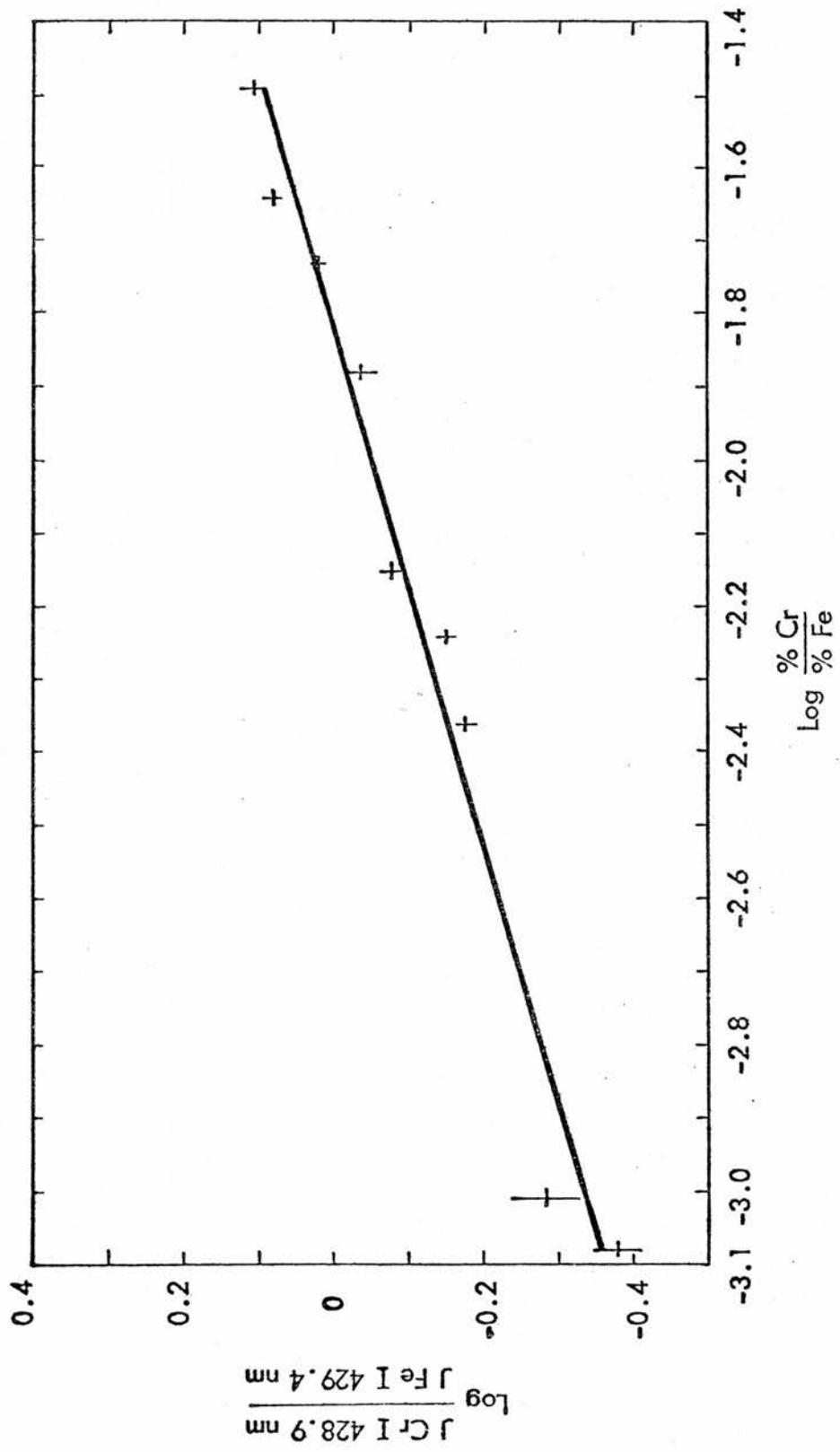


FIGURE 5.9: WORKING CURVE FOR CHROMIUM USING A RUBY LASER OPERATING IN RELAXATION MODE WITH ANCILLARY SPARK

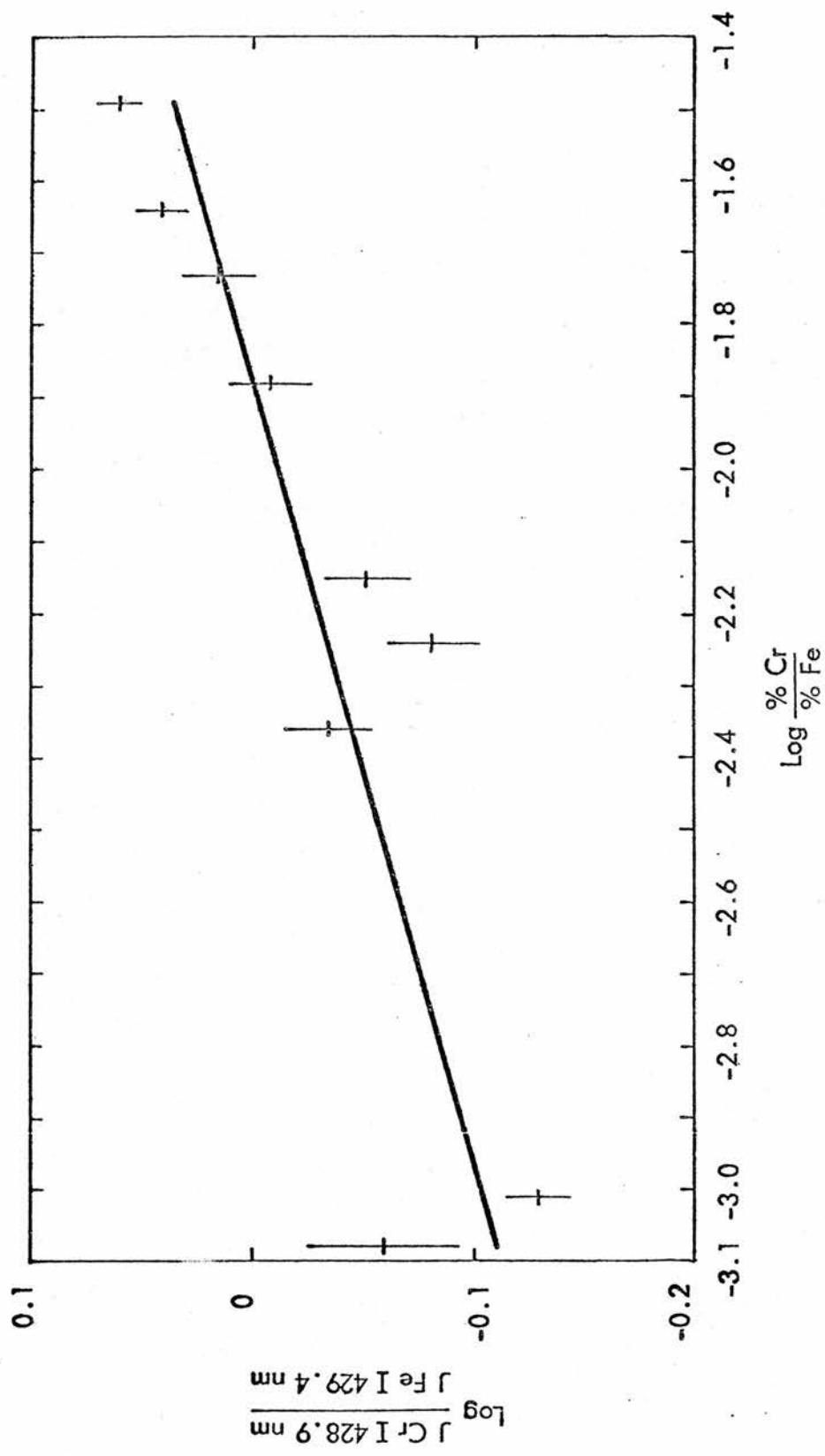
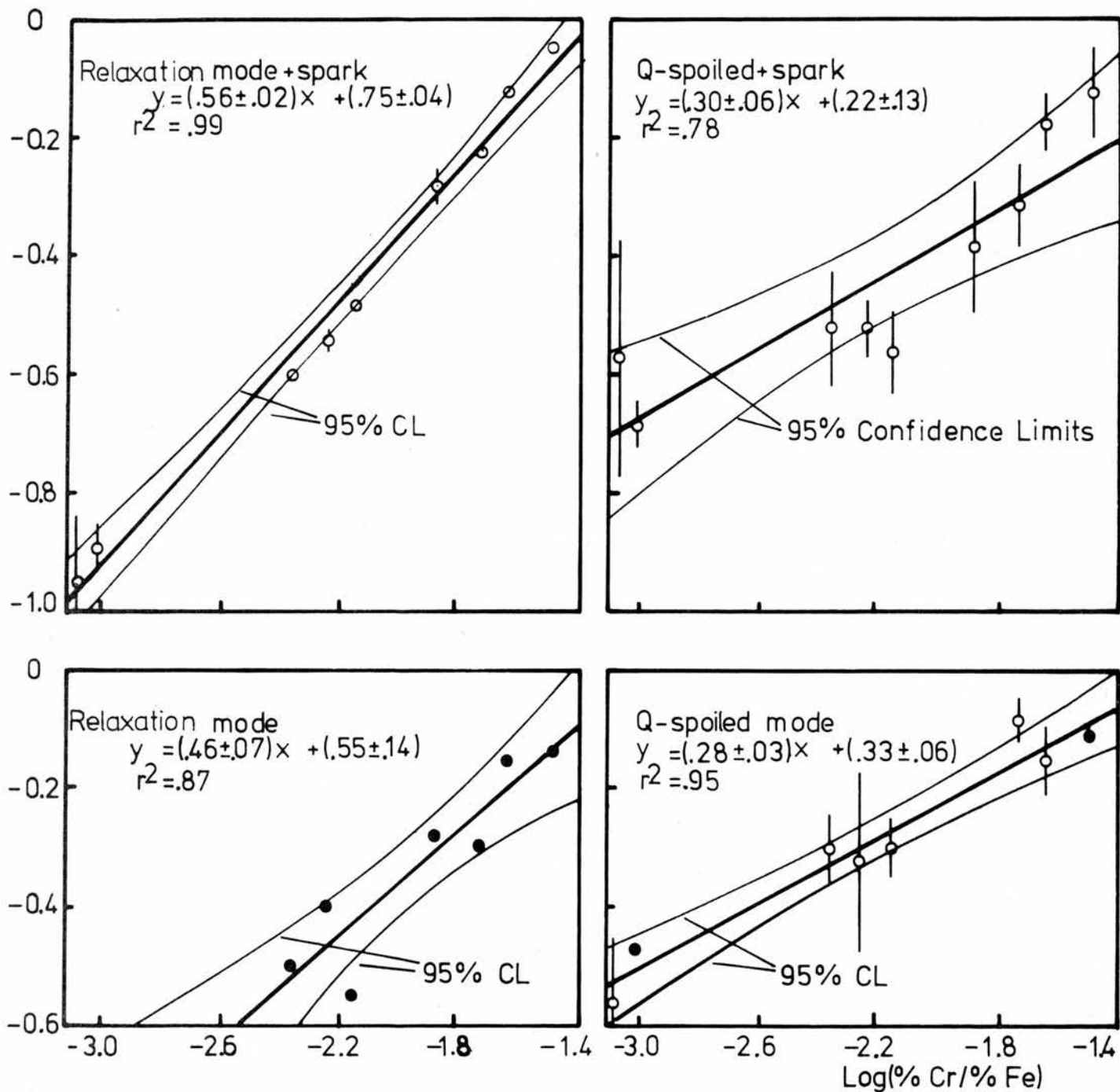


FIGURE 5.10: WORKING CURVE FOR CHROMIUM USING A Q-SWITCHED RUBY LASER WITH ANCILLARY SPARK

Log(J Cr II 267.7/J Fe II 266.6)



Log $\frac{J \text{ Cr II } 267.7}{J \text{ Fe II } 266.6}$ vs Log $\frac{\% \text{ Cr}}{\% \text{ Fe}}$

○ Average of 3 measurements

● Single measurement

FIG 5.11: WORKING CURVES OF Cr CONCENTRATION FOR THE FOUR BASIC EXCITATION MODES.

Line ratio	Excitation mode	Regression coeff. $a \pm \alpha_a$	Regression intercept $b \pm \alpha_b$	Det. coeff. r^2	Std. error of y on x α_{yx}	Mean conc. \bar{x}	Std error of conc $\alpha_{\hat{x}}$ (min)	No. of pts. n	Fig. ref.
$\frac{\text{Cr I } 425.4}{\text{Fe I } 428.2}$	Relaxation + spark	.32 \pm .01	.78 \pm .03	.99	.02	-2.18	.06	9	5.7
	Q-spoiled + spark	.11 \pm .02	.29 \pm .04	.86	.03	"	.27	"	5.8
$\frac{\text{Cr I } 428.9}{\text{Fe I } 429.4}$	Relaxation + spark	.29 \pm .02	.52 \pm .04	.97	.03	"	.10	"	5.9
	Q-spoiled + spark	.09 \pm .02	.17 \pm .04	.75	.03	"	.33	"	5.10
$\frac{\text{Si I } 251.6}{\text{Fe I } 251.8}$	Relaxation + spark	.40 \pm .04	.76 \pm .09	.94	.04	"	.10	"	5.5
	Q-spoiled + spark	.18 \pm .05	.36 \pm .12	.59	.06	"	.33	"	5.6
$\frac{\text{Si I } 288.1}{\text{Fe I } 282.3}$	Relaxation + spark	.40 \pm .04	.84 \pm .10	.91	.05	"	.13	"	5.3
	Q-spoiled + spark	.25 \pm .06	.65 \pm .14	.69	.06	"	.25	"	5.4

FIG.5.12 STATISTICAL DATA OF Si AND Cr WORKING CURVES

Line ratio	Excitation mode	Regression coeff. $a \pm \alpha_a$	Regression intercept $b \pm \alpha_b$	Det. coeff. r^2	Std. error of y on x α_{yx}	Mean conc. \bar{x}	Std. error of conc. $\alpha_{\bar{x}}$ (min)	No. of pts. n	Fig. ref.
$\frac{\text{Cr II } 267.7}{\text{Fe II } 266.6}$	Relaxation + spark	.56±.02	.75±.04	.99	.03	-2.18	.04	9	5.11
	Q spoiled + spark	.30±.06	.22±.13	.78	.09	-2.18	.21	9	"
	Q-spoiled	.28±.03	.33±.06	.95	.04	-2.21	.14	8	"
	Relaxation	.46±.07	.55±.14	.87	.06	-1.93	.10	7	"

FIG 5.13: STATISTICAL DATA OF Cr WORKING CURVES.

CHAPTER 6

DISCUSSION AND CONCLUSION

For quantitative Laser Micro-Spectral Analysis (LMSA), two modes of pulsed laser operation are generally used to produce plasmas at the surface of metal targets, viz relaxation oscillator (RO) mode and Q-switched (QS) mode. Application of a spark discharge across the RO or QS plasmas enhances the spectral emission from them. The plasmas which result from these four modes of excitation differ in a number of physical characteristics which influence their suitability as excitation sources for spectrochemical analysis. In the previous chapters of this thesis, we have presented the results and conclusions of a study of the physical behaviour of the four types of laser produced plasma, with a view to assessing their usefulness in quantitative LMSA. This work developed in two main phases: one associated with time and spatially integrated spectroscopy (Chapters 3 and 5), and the other associated with time and spatially resolved spectroscopy (Chapters 3 and 4). A third phase, dealing with the temporal development of the bulk plasma is reported in Appendix A. From the time and spatially integrated spectroscopy, the physical behaviour of the four plasma types were compared and analytical working curves of log spectral intensity ratio vs log concentration ratio were prepared for minor constituents in steel samples. The temporal and spatial response of the spectral emission from QS plasmas was revealed using time and spatially resolved spectroscopy. Experiments with temporal gating of the spectral emission from QS plasmas using a Pockel's cell, led directly to this work.

The structure of the thesis, outlining the development of the main topics, is shown in Fig 6.1. The principal characteristics of laser-produced plasmas, together with some of the experimental results in this thesis are given in Table 6.1. In the remainder of this chapter, we will summarize and discuss the main points of laser-produced plasmas in

relation to quantitative Laser Micro-spectral Analysis.

TABLE 6.1 Summary of important features of Plasma production by laser irradiation.

	<u>RO mode</u>		<u>QS mode</u>	
	<u>without spark</u>	<u>with spark</u>	<u>without spark</u>	<u>with spark</u>
Power density	$10^{10}-10^{12} \text{ Wm}^{-2} / \text{spike}$	$10^{10}-10^{12} \text{ Wm}^{-2} / \text{spike}$	$10^{13}-10^{15} \text{ Wm}^{-2}$	$10^{13}-10^{15} \text{ Wm}^{-2}$
No of laser spikes	50 - 200	50 - 200	1	1
Pulse duration	200 μs	200 μs	50 ns(FWHM)	50 ns(FWHM)
Spark energy		5 - 20 J		5 - 20 J
Material removal	Vapour + molten metal	Vapour + molten metal	Vapour	Vapour
Crater depth	100-200 μm	100-200 μm	2-3 μm	2-3 μm
Plasma life-time	200 μs	1 ms	20 μs	1 ms
Continuum	bremstrahlung	bremstrahlung + BB from electrodes	bremstrahlung	bremstrahlung + BB from electrodes
Line emission	mainly atomic	mainly atomic	atomic + ionic	atomic + ionic
Electron temperature (FeII lines)	$(1.7 \pm 0.2) \text{ eV}$	$(1.1 \pm 0.1) \text{ eV}$	$(2.0 \pm 0.5) \text{ eV}$	$(0.96 \pm 0.08) \text{ eV}$
Electron density	$4.1 \times 10^{26} \text{ m}^{-3}$	$3.4 \times 10^{24} \text{ m}^{-3}$	$1.1 \times 10^{27} \text{ m}^{-3}$	$1.6 \times 10^{24} \text{ m}^{-3}$
LTE	good approximation in all cases			

A pulsed laser, operating in the power density range $10^{10} - 10^{15} \text{ W m}^{-2}$, will rapidly raise the surface of a metal to its boiling temperature (in a time t_x , given by eqn 1.5) at which point evaporation can occur and material is removed from the target in the form of a vapour plume. Evaporation is assumed to take place from the front surface of a thin layer of molten metal which forms a boundary between the solid and vapour phases. The molten metal layer recedes into the bulk solid at a steady state velocity u (given by eqn 1.3) and penetrates to a depth x_t (given by eqn 1.4). The physical behaviour of the vapour plume can be

described in terms of a mathematical model (Krokhin 1972, see sec 1.2.1) based on the equations of gas dynamics (eqns 1.7 - 1.9), together with the appropriate boundary condition (eqns 1.10 - 1.13). Two regimes of vapour production are distinguished: a low temperature regime produced by power densities of $10^{10} - 10^{12} \text{ W m}^{-2}$ and a high temperature regime produced by power densities of $10^{12} - 10^{15} \text{ W m}^{-2}$.

For power densities in the range $10^{10} - 10^{12} \text{ W m}^{-2}$, the Krokhin model (sec 1.2.2) describes evaporation occurring at the normal boiling point of the metal, with continual removal of vapour from the front surface of the retreating layer. The vapour is assumed to consist mainly of the atomic species and is transparent to the incident radiation. The initial temperature, T_1 , is given by eqn (1.20). The vapour expansion velocity, v_1 (eqn 1.18) is consistent with the thermal expansion velocity of particles evaporated from a surface at the normal boiling point.

Experimental observation of vapour production in the $10^{10} - 10^{12} \text{ W m}^{-2}$ range, indicates a number of features not accounted for by the above model. In the Krokhin model, a rectangular pulse shape of constant power density is assumed. However, power densities in the above range are normally obtained using RO mode lasers, whose output exhibits a series of several hundred random spikes, each of less than $1 \mu\text{s}$ duration (sec 2.1.2). Vapour emission coincides with the arrival of laser spikes at the target, and subsides between spikes, indicating that rapid heating and cooling of the target occurs. After about 10-50 laser spikes (depending on the power per spike and the interval between them) droplets of molten metal are ejected from the target: a feature not accounted for by the Krokhin model. This effect is thought to be due to the ablation pressure exerted on the layer of molten metal (which has penetrated the target to $\approx 100 \mu\text{m}$) by the expanding vapour plume, and gives rise to the characteristic shower of molten metal seen in photographs of the RO laser - metal interaction (Frontispiece). For a power density of 10^{11} W m^{-2} on an Fe target, a vapour expansion velocity of 900 m s^{-1} would produce an ablation

pressure (given by eqn 1.6) of about $13 \times 10^6 \text{ J m}^{-3}$ (130 atmospheres). As subsequent laser spikes become less powerful and the time between them increases, the target cools leaving a deep crater (100 - 200 μm) in the metal. Spectral emission from the vapour (which is also concurrent with the laser spikes) is generally weak and diffuse (Fig 5.1).

Vapour expansion velocities predicted by eqn 1.18 are in good agreement with those estimated from framing photographs of the interaction of an RO mode laser ($F = 1.7 \times 10^9 \text{ W m}^{-2}$) with steel, Fe and Al-silicate targets (Fig A.3). However, as far as vapour temperatures are concerned, there is some discrepancy between those temperatures obtained experimentally and those predicted by eqn 1.20. For an Fe target irradiated by a power density of $1.7 \times 10^{11} \text{ W m}^{-2}$ per spike, an electron temperature (time and spatially averaged) of 1.7 eV was recorded using Fe II line pairs (Fig 3.1). The predicted vapour temperature (by eqn 1.20) is 3214 K (0.29eV). The temperature was also estimated using FeI line pairs (not reported elsewhere in this thesis), and was found to be 0.5 eV. Thus the picture we have of the RO mode vapour is one of a hot core of ions, surrounded by a cooler region of atoms, which is in disagreement with the Krokhin model of a predominantly atomic vapour. Our picture of the vapour is supported by the spatially resolved temperature measurements (Fig 3.9b) obtained from FeII line pairs, which show a temperature of 1.9eV at 0.2 mm above the target surface, falling to 1.3eV at one millimetre. Further confirmation is obtained from the spatially-resolved spectra of Fig 3.6 which show the presence of singly-ionised (and doubly-ionised in the case of Si) species in Fe, Al, Mg and Si vapour plumes. Also shown in some of these spectra is a weak background continuum close to the target surface (Fe, Mg, Pb and Bi) and the occurrence of self-absorption of the resonance lines (Mg and Pb). These observations (together with the electron temperatures) indicate that, in contrast with the Krokhin model, enough of the incident laser energy is absorbed in the vapour to cause ionisation and heat

the vapour to high temperatures. We conclude that the low temperature Krokhin model is not valid for the range of targets and incident power density which we have considered. However, we will return to this topic later.

The ejection of molten metal and weak spectra obtained when working with RO mode lasers are disadvantages in spectrochemical analysis. Since the dominant mode of material removal after about 10-50 laser spikes is molten metal ejection, this represents wasted energy as far as spectral excitation is concerned. The ejection of molten metal makes correlation between vapour mass and mass of material removed from the target difficult, and may also significantly scatter the incident laser radiation and spectral emission from the vapour. Application of a spark discharge to the RO mode plasma appears to vaporise most of the liquid metal, thereby increasing vapour mass and spectral intensity. Although the time and spatially averaged temperature is only 1eV (Fig 3.1), compared with 1.7eV for the unsparked case, the spectral emission is integrated over milliseconds, rather than microseconds and a more intense spectrum results (Fig 5.1). When used with spark excitation, lasers operating in the RO mode are useful when large sampling volumes are required.

For power densities of $10^{12} - 10^{15} \text{ W m}^{-2}$, the Krokhin model describes the formation of a high temperature plasma (sec 1.2.3) in which significant absorption of the laser beam can occur. The target is raised so rapidly to its boiling temperature, that insufficient time exists for an appreciable liquid layer to form, and the phase transition is assumed to be directly from solid to vapour. Initially the vapour plume is small and optically thick (ie the optical path length, d_v , is greater than one) which tends to shield the target from further irradiation, and consequently the rate of evaporation is reduced. As the vapour expands, the optical thickness decreases ($d_v < 1$), which allows more light to reach the surface, thereby increasing the rate of evaporation and producing a denser vapour ($d_v > 1$). This is the so-called "self-regulating plasma" system, which tends to regulate the optical thickness to a value of one. The vapour is heated to

high temperatures by free-free absorption of the laser beam (inverse bremsstrahlung). The initial vapour expansion velocity, v_1 , and temperature, T_1 , are given by eqns 1.35 and 1.37 respectively.

The spectroscopic behaviour of QS laser-produced plasmas is dominated by the early emission of bremsstrahlung radiation. The peak intensity of bremsstrahlung emission occurs at about 220 ns (Al target, $F = 9 \times 10^{13} \text{ W m}^{-2}$) after the target is irradiated, following by the appearance of ion and atom line emission at peak times of 230 and 330 ns respectively (Figs 3.2 and 3.4). Spatial resolution showed that the bremsstrahlung radiation is emitted from a region close to the target surface, while the ion and atom lines are emitted from progressively higher regions of the plume (Figs 3.3 and 3.5). Thus from Fig 3.9 we see that highest electron temperatures are recorded near the target surface (1.8 eV for Al at 0.1 mm) falling appreciably with height (0.5 eV at 1.7 mm). Thus, as with the RO mode, the picture which emerges is one of a hot, dense plasma core of ions close to the target surface surrounded by a cooler mantle of atoms. Again, confirmation of this picture is obtained from time and spatially integrated temperature measurements of an Fe plasma. Using FeII line pairs, the estimated temperature was 2 eV, (Fig 3.1), whereas using FeI lines, the temperature was estimated to be 0.9 eV (not reported elsewhere in thesis).

Expressions 1.34 - 1.37 for the initial vapour density, ρ_1 , velocity v_1 , pressure, p_1 , and temperature T_1 , are evaluated for both the Al and Fe plasmas (using the constants for a finite rise time pulse) and shown in Table 6.2. These parameters are calculated at the time t_v (from eqn 1.5) at which point evaporation is assumed to start. Also shown in Table 6.2 are values for some of the experimentally derived parameters. In all cases, experimental values of kT_e are higher than those predicted by the model. However, we stress that the model gives estimates for the plasma parameters occurring at a time t_v and at the target surface, whereas the earliest time and height for which we have any experimental data is 100 ns and 0.1 - 0.2 mm.

That is, the model considers a plasma which is still being heated and accelerated by laser absorption, while the experimental data is of a plasma which is decaying, since the laser pulse has finished by 100 ns after the start of irradiation.

TABLE 6.2. Comparison between high temperature Krokhin model and experiment. (QS mode ruby, $9 \times 10^{13} \text{ W m}^{-2}$)

Target	Parameter	Theory	Experiment
Al	a_0	$6.9 \times 10^{13} \text{ m}^8 \text{ kg}^{-2} \text{ s}^{-3}$	
	t_v	$335 \times 10^{-15} \text{ s}$	
	ρ_1	598 kg m^{-3}	
	N_e	$1.3 \times 10^{28} \text{ m}^{-3}$	10^{25} m^{-3} (at 100ns, 0.1 mm)
	v_1	3329 m s^{-1}	$6.3 \times 10^3 \text{ ms}^{-1}$ (AlI)) Initial $25 \times 10^3 \text{ ms}^{-1}$ (AlII)
	P_1	$7.1 \times 10^9 \text{ J m}^{-3}$	
	T_1	3.10 eV	1.8 eV (at 100ns, 0.1 mm)
Fe	a_0	$5.4 \times 10^{12} \text{ m}^8 \text{ kg}^{-2} \text{ s}^{-3}$	
	t_v	$245 \times 10^{-15} \text{ s}$	
	ρ_1	1747 kg m^{-3}	
	N_e	$1.9 \times 10^{28} \text{ m}^{-3}$	$1.1 \times 10^{27} \text{ m}^{-3}$ (time and space average)
	v_1	2329 m s^{-1}	2330 m s^{-1} (vertical)) Initial 3670 m s^{-1} (horizontal)
	P_1	$1.02 \times 10^{10} \text{ J m}^{-3}$	
	T_1	3.25 eV	2.4 eV (at 0.2 mm) 2.0 eV (time and space average)

Assuming charge neutrality and that only singly-ionised atoms are present, we can estimate the initial electron density of the plasma from eqn 1.34. These values are also entered in Table 6.2. The values obtained are consistent with the electron density of a bound solid ($N_e \approx 10^{28} \text{ m}^{-3}$)

and indicate that in the early stages of plasma production the laser radiation will be reflected by the plasma. The plasma will radiate as a black-body until such times as the electron density falls below its critical value ($2.1 \times 10^{27} \text{ m}^{-3}$ for ruby laser light). Experimental values of electron density (Fig 3.9a) indicate that the transition from black-body emission to bremsstrahlung emission occurs prior to 100 ns and closer to the target surface than 0.1 mm.

TABLE 6.3. Comparison between high temperature Krokhin model and experiment (RO mode ruby; $1.7 \times 10^{11} \text{ W m}^{-2}$)

<u>Parameter</u>	<u>Theory</u>	<u>Experiment</u>
a_0	$5.4 \times 10^{12} \text{ m}^8 \text{ kg}^{-2} \text{ s}^{-3}$	
t_v	58 ns	
ρ_1	3.52 kg m^{-3}	
N_e	$3.8 \times 10^{25} \text{ m}^{-3}$	$4.1 \times 10^{26} \text{ m}^{-3}$
v_1	2280 m s^{-1}	time and space average
p_1	$19.6 \times 10^6 \text{ J m}^{-3}$	
T_1	3.12 eV	1.9 eV (at 0.2 mm) 1.7 eV (time and space average)

Returning briefly to the case of RO laser plasmas, we find that by treating these plasmas on the same theoretical basis as QS plasmas, better agreement is reached between theoretical and experimental temperature (Table 6.3). That is we assume that, like QS mode plasmas, RO mode plasmas are dense enough to absorb some of the incident laser radiation and so be heated to higher temperatures than are predicted by eqn 1.20. On the basis of this model, the initial electron density is less than the critical electron density and a weak bremsstrahlung will be emitted. We should note that the initial expansion velocity is not a strong function of the power density ($v_1 \propto F_1^{\frac{1}{4}}$) and hence expansion velocities for the same target are

similar regardless of whether QS or RO mode laser irradiation is used (see Tables 6.2 and 6.3).

Like RO mode plasmas, the spectral emission from QS plasmas is weak and diffuse (Fig 5.1) due to the small mass of vapour which is produced. The shallow craters which are obtained make QS lasers suitable for depth probing and surface layer analysis. The overall intensity of the spectrum can be increased by the application of a spark discharge (Fig 5.1). As with the RO mode, the population averaged temperature apparently decrease on application of the spark from 2eV to 1eV (Fig 3.1), but this is due to averaging over milliseconds rather than microseconds. Since the spectral lines emitted from QS plasmas reach peak intensity in the order of 200 - 400 ns, the time scale of the application of the spark is important. In some cases the spark is more effective in introducing the carbon species into the plasma than in increasing the excitation of the target species.

The use of laser-produced plasmas as excitation sources in spectrochemical analysis, relies on the fact that the intensity of a spectral line emitted from an element in the plasma, is a single-value function of the concentration of that element in the bulk target. Spectral intensity, however, is a measure of the concentration of a species in the plasma only, and this concentration is assumed to equal the concentration of the species in the target. Equations 5.1 and 5.2 show that a working curve of log spectral intensity ratio in the plasma against log concentration ratio in the target will have a gradient of one, provided that the plasma and target concentrations are equal, and that the atom and ion populations in the plasma (and hence spectral intensity) are functions only of the plasma temperature. This brings us to the concept of local thermodynamic equilibrium (LTE) which is crucial to the successful application of laser-produced plasmas for spectrochemical analysis, We have seen (Fig. 3.9) that the temperatures of RO and QS mode plasmas are rapidly varying functions of time and position, and we expect

the atomic populations to follow this distribution. Thus we must define a local temperature for a given species and a given point in space and time at which thermodynamic equilibrium prevails (sec 1.3.1). At this point a single temperature, the electron temperature, defines the excitation and ionisation state of the plasma. Only if LTE prevails can we relate spectral intensities to plasma concentrations. We have shown (sec 3.2.3) that for an Al plasma produced by QS mode laser, LTE conditions will prevail in the time range 200-500 ns and out to about 0.5 mm from the target, ie in the presence of the background continuum. From the time and spatially integrated measurements (sec 3.1) we have shown that all four excitation modes produce plasmas at Fe targets which satisfy the LTE criterion (eqn 3.1) for FeII line pairs.

All the working curves presented in this thesis (Figs 5.3 - 5.11) have gradients of less than one, regardless of which excitation mode, minor constituent or spectral line pair is used. Provided we can neglect the effects of self-absorption (which should not be a problem for the target concentrations and spectral line pairs involved) and assuming that LTE prevails, we must conclude that the plasma concentration ratio is less than the target concentration ratio. This fact implies that the major constituent (Fe) is being vaporised preferentially over the minor constituents (Si or Cr). If this were the case we would not expect spark excitation to improve the situation, unless the spark were functioning as a secondary source of vaporisation. However, the working curve gradients for both the RO and QS modes show an increase on application of spark excitation (Figs 5.11 and 5.12). In the RO mode case, the spark effectively vaporises most of the material removed in the molten state and thus the gradient increase is not surprising, however, the possibility of secondary vaporisation cannot be ruled out. In the QS mode, the gradient increase is small ($0.28 \pm 0.03 - 0.30 \pm 0.06$), and is possibly not significant, but some amount of secondary vaporisation is indicated. We should also point out that since peak spectral line intensities occur at 200 - 400 ns in QS plasmas and the spark is not

initiated until after about 3-5 μ s, the main effect of the spark is to introduce carbon species into the plasma (Fig 3.10). Even though spark excitation increases the working curve gradients for both the RO and QS modes, the increased gradients are still much less than one and some form of preferential vaporisation could be indicated.

Departures from unity gradient are greatest for the QS mode (with or without spark) but as we have seen, QS mode plasmas contain energy level populations which vary rapidly with time and height above the target. Thus estimating element concentrations by measuring line pair ratios from time-integrated spectrograms is unlikely to yield accurate results. The only sensible comparison is a point-to-point comparison at specific plasma times and heights. We should also note that line-to-background ratios are improved when sampling times and positions are carefully chosen (Fig 3.8). This behaviour suggested that a simplified spectrum containing only atomic lines, with an improved line-to-background ratio could be obtained by adopting some form of temporal resolution. This reasoning led us to experiment with a Pockel's cell used as an optical shutter to prevent the continuum emission and ion emission from reaching the spectrograph. The Pockel's cell was successfully applied to the qualitative/^{analysis}of a complex spectrum such as Fe, and by using the cell atomic line identification was easier. Use of the cell also reduced the possibility of interference from overlapping lines. Use of the cell for quantitative analysis was not so successful. The Pockel's cell system results in about a 75% attenuation of the plasma emission, thereby reducing the sensitivity of the system. Some form of electronic detection of the signal is desirable to compensate for the reduced sensitivity. Increasing the laser power density would increase the plasma temperature and hence the spectral intensity, however, ion line emission and background emission would also be increased, hence increasing the need for spectral gating. One further improvement to

the system would be to use a Pockel's cell which could be opened and closed at specific times, thus allowing a "transmission window" of variable duration Δt to be set at any point in the plasma life. In this way, spectral line intensities could be measured at the same point in time, and each would have the same integration time Δt , thus removing the restriction imposed by the rapidly varying populations.

In conclusion, we have seen that the interaction of high power lasers is complex, and that the plasmas produced possess characteristics which depend on the nature and power density of the laser output. These characteristics influence the suitability of the plasmas for use as excitation sources for the sources for the spectrochemical analysis of steels. If spectral intensities are to be correlated with sample concentrations, then the plasma must exist in a state of LTE, and this has been shown to be the case for the plasmas produced by the four excitation modes which we have considered. All of the working curves obtained using the four excitation modes have gradients which are less than one indicating that the concentration ratio in the plasma does not equal that in the bulk target. Further work is necessary, in this area, to establish the causes of the apparent preferential vaporisation of Fe, and an understanding of this process is essential if spectral intensities are to be related directly to concentrations by calculating the amount of metal evaporated. Of the four excitation modes, the spark-assisted RO mode is the most generally useful, and provides the greatest accuracy in the determination of minor constituents in the target. If QS mode lasers are to be used for quantitative micro-analysis, then some form of temporal and spatial resolution is desirable. We have shown that energy level populations in QS plasmas of nominally pure samples are rapidly varying functions of time and position, and this work should be extended to cover the behaviour of metal alloys.

Correlation between the (high-temperature) Krokhin model of plasma

production and experimentally observed behaviour of QS plasmas is reasonably good. We have also shown that treatment of the R0 mode plasmas in terms of the high-temperature model is reasonably successful. Further comparison of the model with experiment is desirable for both the R0 and QS modes. In particular an independent measurement of electron density (non-spectroscopic if possible) would help to confirm the plasma density. Time resolved photography of QS plasmas in the 0 - 100 ns time range would enable point-to-point estimations of plasma velocity to be made while the plasma is still being heated by the laser pulse. This would also give a double-check on the plasma temperatures. While on the topic of plasma temperatures, we should point out that atomic transition probabilities quoted in the literature are often given in the spirit of $\pm 100\%$ accuracy, and this should be borne in mind when estimating plasma temperatures spectroscopically.

Finally, a few points concerning time resolution and spectral detection. We have suggested that for time-resolved Laser Microanalysis, some system should be adopted, whereby a "transmission window" of time Δt can be set at any desired time in the plasma lifetime. Although this can be achieved using a Pockel's cell, this system has the disadvantages of high attenuation of the plasma emission and a non-linear wavelength response. A better system would be based on optical multichannel analysis of the spectral emission. In this system a Si Vidicon tube or a Si diode array replaces the photographic plate as the spectral detector. A wide wavelength band is scanned electronically and an intensity wavelength response displayed on an oscilloscope. The technique can be adapted for time-integrated or time-resolved spectroscopy with computer link-up for data processing. This brings us to our final point. The future of Laser Micro-spectral Analysis lies with the development of a fully-automatic system with electronic detection and display of the spectrum and computer link-up for data processing. In this way Laser Micro-analysis could become an indispensable technique for instantaneous local spectral analysis.

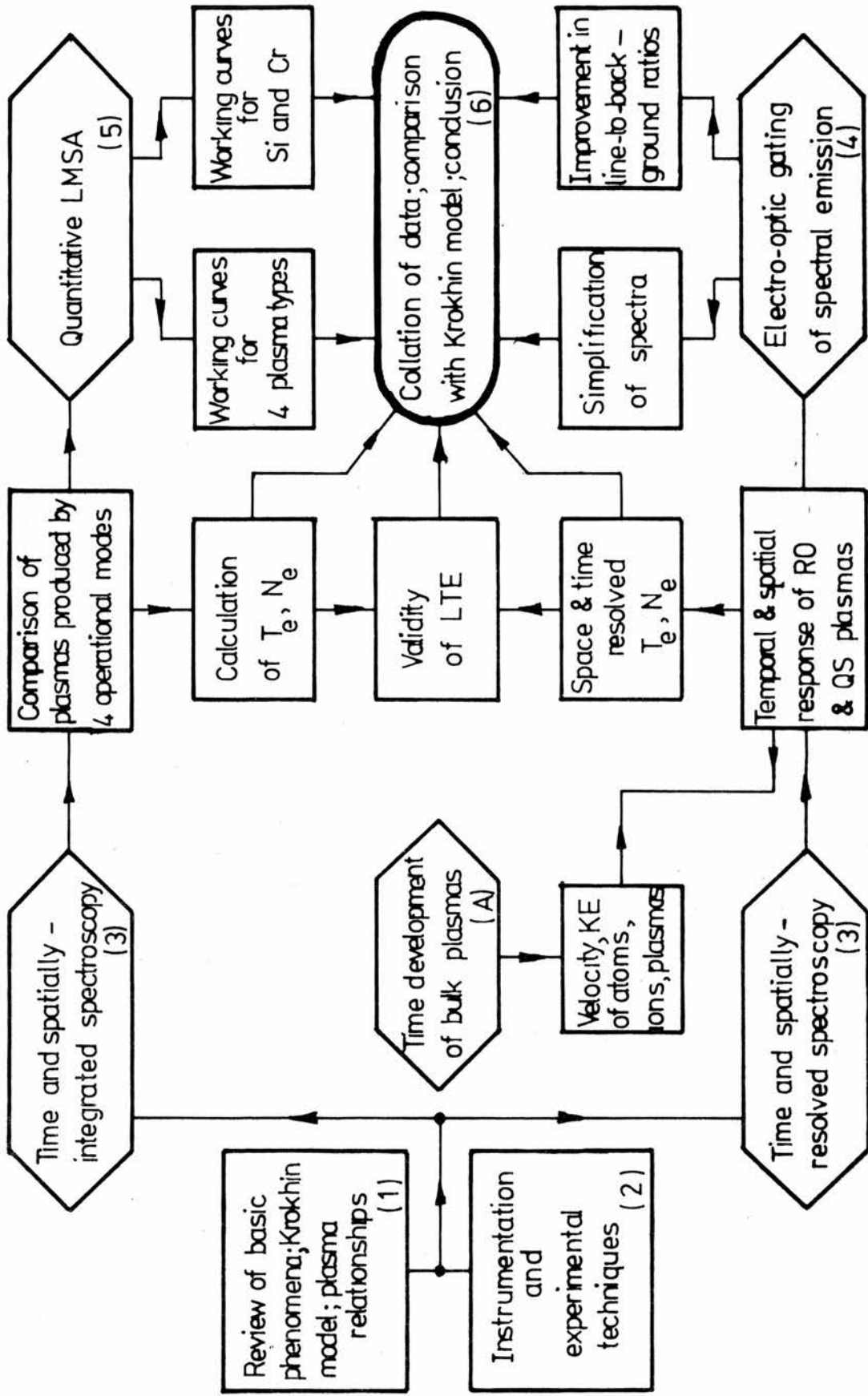


FIG 6.1: STRUCTURE OF THESIS, OUTLINING DEVELOPMENT OF MAIN TOPICS. Figures in brackets refer to chapters of thesis.

CHAPTER 7
FUTURE DEVELOPMENTS

In the preceding chapters, the potential of laser micro-spectral analysis as a technique for the rapid, local, quantitative analysis of solid samples has been demonstrated. However, a number of areas exist where further development is clearly necessary in order to fully understand the complex physical processes involved and to transform LMSA into a routine laboratory technique. Some of the areas where further work may be carried out are outlined below.

The working curves presented in Chapter 5 were constructed using steel standards of known composition. Preferably, these samples should also be analysed by another technique (eg X-ray fluorescence or electron microprobe) for comparison with LMSA. Of particular importance here is the influence of the sample matrix on the predicted concentrations and the apparent selective volatilisation of some elemental species into the plasma plume. The study of matrix effects is essential if a reliable, reproducible technique is to result. To this end the time resolved spectroscopic work should be extended to include alloy plasmas. This work would reveal if particular spectral lines were being emitted from the plasma in preference to others. In some alloys there is a possibility of migration of species to the surface of the metal, which would mean that the composition at the surface layer was not representative of the bulk solid. An investigation of this problem should be considered in a study of matrix effects.

Another area of major importance is the measurement of the electron density of plasmas. Electron densities quoted in this thesis were estimated using spectral lines from different temperature regions of the plasma and can only be regarded as approximate. An independent measurement of electron density is recommended, such as can be obtained from the Stark broadening profile of spectral lines or by optical interferometry.

In all of the work reported here, the laser was used entirely in the RO and QS modes, with and without spark excitation. It has been shown that an area of operation exists between the single spike QS mode and the several-hundred spike RO mode, which may offer some advantages over the other modes. In this mode (known as semi-QS mode), the laser output pulse consists of about 5-50 spikes and it is possible to select the optimum number of spikes such that material removal is by vaporisation only and no molten material is ejected. In this way, it may be possible to evaporate sufficient amounts of material from the target such that satisfactory detection limits are obtained, while still remaining outside the regime where sampling of the molten droplets by spark excitation is significant. Instead of using the laser in the semi-QS mode it may also be possible to shape the output pulse such that a square wave of about 1 μ s duration is obtained.

While considering spark excitation, it should be remembered that cross-excitation of the QS mode plasma has been shown to be ineffective as a source of secondary excitation in the form used in this work. For the spark to show a real improvement in working curve gradients, it may be necessary to electrically initiate the spark discharge prior to that which can be obtained by self initiation. Thus, the timing of the spark could be chosen so as to coincide with the maximum spectral output of the plasma, thereby providing the maximum enhancement of the plume intensity.

Consideration should also be given to conducting LMSA in an inert gas atmosphere, or operating under an external magnetic field. Some earlier work (Moenke-Blankenburg, 1972) has shown that spectral intensities are enhanced and the effects of background and CN emission are reduced if sample is vaporised under an inert gas atmosphere such

as Argon. Furthermore, if a partial vacuum of about 10^4 J m^{-3} to 10^5 J m^{-3} is used, self-absorption is eliminated and working curve gradients are improved. A similar increase in spectral intensity has also been observed by placing a sample in the field of an electro-magnet (Petkov et al 1969).

When considering developments such as those described above, it should be borne in mind, that any modification which requires special preparation or mounting of the sample reduces the simplicity of the technique. One of the principle advantages of LMSA is the possibility of on-line or in-situ analysis with the minimum of target preparation. Any modification of the instrument which removes this advantage must also reduce the effectiveness and usefulness of the instrument.

As has been stated earlier, the future of laser micro-spectral analysis lies with the development of a fully automated portable system, with data processing facilities, for on-line or in-situ analysis of solid targets. With this end in mind, it is recommended that all future experiments be carried out in conjunction with an optical multi-channel analyser (such as the Princeton Applied Research OMA). These instruments offer the features of wide wavelength range, permanent storage of spectra and good sensitivity; in essence they can be considered as electronic photographic plates but without possessing many of the disadvantages associated with the photographic medium.

In addition, the input to the multichannel analyser can be electronically gated thereby offering the possibility of time-resolved spectroscopy with good spectral resolution. The optical multi-channel analyser is also portable and can be linked to a computer for high speed data processing. In conclusion therefore the laser micro-analyser

in conjunction with an optical multi-channel analyser offers the possibility of rapid, local, in-situ analysis of solid samples and can be considered as the first step towards a portable fully-automated laser micro-spectral analyser.

APPENDIX A

TEMPORAL DEVELOPMENT OF LASER-PRODUCED PLASMAS

A study of the temporal development of laser-produced plasmas was undertaken using an Image Converter (IC) Camera (TRW/STL Type 1D). The camera can be operated in two modes, streak or framing, to give high speed photographs of self-luminous transients. In the framing mode three spatially resolved photographs (frames) are obtained at pre-determined intervals of 0.5 μ s. While, in the streak mode a continuous trace is obtained of a strip of the plasma parallel to the target surface. The camera, its operation and the associated Trigger Delay Generator are described in greater detail in Sec 2.4.

We studied the temporal development of the plasmas produced by both the Q-switched (QS) and Relaxation Oscillator (RO) mode lasers, with and without spark excitation.

A.1 Laser Plasmas (Q-switched mode)

The image converter camera, fitted with a close-up lens was focused on the target to give a X4 magnified image of the plume at the film plane. An iron target was irradiated by radiation from the ruby laser operated in the QS mode. The power density at the target was approximately 10^{14} W m⁻². The camera was triggered from the first light radiated from the plasma. A fibre optic light guide positioned close to the target, fed the first light to the the optic input of the Trigger Delay Generator which, in turn, supplied the appropriate trigger pulse to the camera. The photographs were recorded on Polaroid Type 107 film.

Framing photographs of the plume development occurring at the surface of an iron target are shown in Fig A1.b. Each frame was exposed for 50 ns and the interframe delay was 0.5 μ s. The first (uppermost) frame records the

first light to reach the camera and corresponds to a point in the plasma lifetime $0.1 \mu\text{s}$ after the leading edge of the laser pulse. The streak photographs (Fig A1.a) show the continuous development of a 0.5 mm segment of the plume, parallel to the target surface. The plume was sampled at the surface and at 2 mm above it. With a writing speed of $5 \text{ mm } \mu\text{s}^{-1}$, the temporal resolution at the film is $0.4 \mu\text{s}$.

The streak and framing photographs (Fig A1) show a small ($\sim 1 \text{ mm}$ diameter) intense plasma is well established at the target surface by the time the camera begins to record the event (100 ns after the start of the laser pulse). As expansion proceeds, the intensity decreases and the plasma becomes more cloud-like in appearance. At a height of 2 mm , the plume is weak and the radial expansion is much slower than at the surface. Traces of the vapour at this height, are still visible $10 \mu\text{s}$ after the start of irradiation. Studying Fig A1.b in conjunction with the time-resolved spectrograms of Fig 3.3, we see that frame 1 shows the plasma when it is emitting both continuous and line spectra, in frame 2 only atom lines are being emitted and frame 3 corresponds to the cool vapour phase with very little spectral emission.

A.2 Laser Plasmas (QS) with Auxiliary Excitation

We present some streak photographs of the QS laser produced plasma with auxiliary excitation. The electrode separation was 2 mm and they were positioned 2 mm above the target. The electrode capacitance was $2 \mu\text{F}$ and the inductance was $125 \mu\text{H}$. Two sets of photographs were taken, one with the discharge voltage near to breakdown ($V_E = 3.6 \text{ kV}$) and the other with the voltage well below breakdown ($V_E = 2.0 \text{ kV}$). For each voltage two streaks were taken, one sampling the plasma region near the surface and the other sampling across the electrodes. All four streaks are shown in Fig A2).

The centre of action of a spark discharge is in the gap between the electrodes and we should focus our attention on the plasma development in this region. The streak photographs in Fig A2.a show the temporal development

of the segment of the plume across the electrodes ie at 2 mm above the target surface. For the case of the higher spark potential, excitation and ionisation of the species close to each electrode starts before the laser produced plume has expanded into the gap, namely 800 ns for this particular instance. The excited species will therefore, at this time, be predominantly from the carbon electrodes and the atmosphere. It is a further 4.5 μ s before we can consider a homogeneous spark plasma to be established across the 2 mm gap, and as we see the original metallic plasma has decayed considerably by this time. In fact at this height and time very little of the original metallic species can be present in the spark plasma. This agrees with the time-resolved spectra presented in sec 3.2. From the length of the spark we can deduce that the irradiation at the target occurred 600 ns prior to the initiation of the spark. The photograph corresponding to the lower spark potential is qualitatively similar although the spark seems to start 800 ns after the target irradiation and about 600 ns prior to the arrival of the laser plume in the gap.

The lower two photographs in Fig A2 show the temporal development at the target surface for the two discharge voltages. Each photograph shows the two distinct regimes of plasma development followed by spark development. For this higher spark potential, the plasma development proceeds as for the unsparked QS plume until about 1.4 μ s after the start of the laser pulse. At this point the plume re-expands radially in the form of two strongly radiating channels visible above the general background emission. The central core expands from 0.5 mm to 2 mm diameter in about 3 μ s, and a homogeneous plasma is now established across the whole space between the target and the electrodes. When the lower spark potential is applied the initial laser produced plume has time to decay much further than in the previous case before the spark begins to develop after about 5 μ s.

Once the spark discharge is established, the excitation and decay of the

spark plasma proceeds in accordance with the time constant of the LC circuit.

A.3 Framing Photographs of RO Ruby Laser Plasmas

A series of photographs of the plumes produced at the surface of metal targets by RO-mode ruby radiation are shown in Fig A3 (Adrain 1977, private communication). The output of the ruby was about 450 mJ in a pulse train of about 300 spikes over a total duration of 340 μ s. This corresponds to a power per spike of about 1.3 kW. A 10 cm lens was used to produce a power density at the surface of about $1.7 \times 10^9 \text{ W m}^{-2}$. The interframe delay in the photographs is 40 μ s.

The photographs show the following sequence of events for the aluminium-silicate and mild steel targets. An intensely radiating plasma core forms close to the target surface and expands rapidly during the first 80 μ s (2nd and 3rd frames). In the early stages of the plasma, material removal is principally by vaporisation, but by about 120 μ s, droplets of molten metal are being ejected from the crater. At the sixth or seventh frame the core and vapour have completely separated. This separation of the core and vapour is most obvious for the Al-Si target and there also appears to be more molten metal ejected from this target.

The plume development of the lead target is different from that of the other two targets in that the vapour cloud does not form. As far as spectral emission is concerned, the most dense plasma cores appear to be those of the lead, followed by the mild steel targets and we would expect these materials to show the most intense continuum. This is confirmed by the spatially-resolved spectrograms shown in Fig 3.6, which also show that the lead plume is susceptible to self-absorption of the resonance lines.

Some time-integrated photographs were taken of the vapour plumes produced

at an Fe target by focused laser radiation containing a different number of spikes in the output. We used the Zeiss laser (Sec 2.1) and the number of output spikes was altered between one and 50 by changing the path length of the Q-switching dye (Sec 2.1.1). This showed that about 10-20 pulses over a total duration of about 200 μ s were needed before ejection of molten metal occurred. It is at this point that we begin to observe deep craters being formed in the target.

A.4 Framing Photographs of the Nd-Laser Plasma with Auxiliary Excitation

A Nd-glass laser was used in the RO mode to irradiate an iron target. The laser induced plume was subjected to secondary excitation by a spark discharge. The spark development was photographed using the IC Camera in the framing mode.

The camera was again triggered by the first light from the target. The laser output energy was 0.13 J over a total pulse duration*of 380 μ s corresponding to a focused power density at the target of about $2 \times 10^{10} \text{ W m}^{-2}$. The electrodes were spaced 2 mm apart and were 1.4 mm above the target; the spark parameters were 2 μ F, 125 μ H and electrode breakdown voltage of 4.4 kV. Two sets of framing photographs are shown: one with electrode voltage at 4.2 kV and the other with the electrode voltage at 3.0 kV. The camera only has 3 frames per triggering operation available, so only 3 frames could be taken for each laser shot, thus the photographs showing the interaction in the range 0 to 55 μ s and 0 to 60 μ s are composite photographs constructed from a number of different laser shots (Fig A4).

The essential differences between the spark development for a voltage just below breakdown and for one far below breakdown are in the initiation of the discharge. For a voltage just below breakdown, the first signs of the discharge are of a channel forming between the electrodes, which rapidly

expands into the space between the lens and the target. When the voltage is set far below breakdown an emission plume is seen rising from the target at the same time as ionisation spreads in from the electrodes. After the initiation of the spark, the discharges proceed in a similar fashion, rising and falling according to the time constant of the LCR circuit. During the periods of low intensity of the discharge, further vaporisation and ejection of molten material can be seen at the target surface, as the laser radiation is once again able to reach the target.

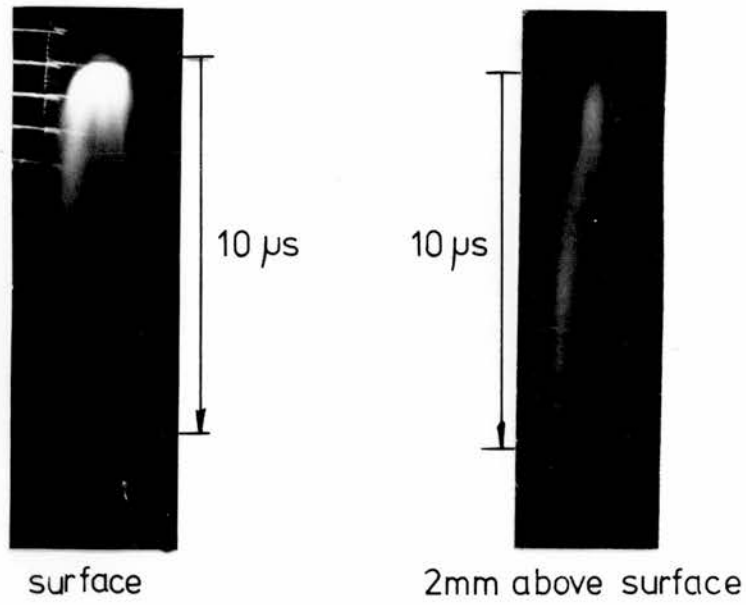
A.5 Discussion

The horizontal expansion velocity of the luminous front of QS plasmas can be estimated from the streak photographs (Fig A1.a). plotting a curve of distance travelled against time, and fitting a quadratic curve, we obtain an initial vertical expansion velocity of 2330 m s^{-1} , and an initial horizontal expansion velocity of 3670 m s^{-1} . This corresponds to an initial vertical kinetic energy of about 1.6 eV for an Fe plasma. Because of the temporal resolution of the photographs (Fig A1.a) and the fact that the first 200 ns of the plasma development is not recorded, we could not obtain a more reliable estimate of the velocity and the energy.

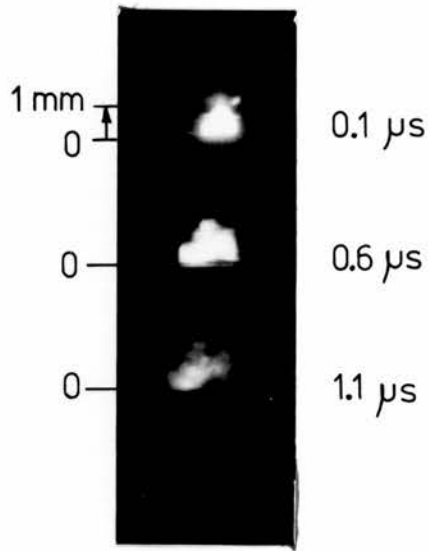
The framing photographs of the RO plasmas (Fig A3) show an initial expansion velocity in the vertical direction of about 1000 ms^{-1} (Adrain 1977, private communication). Thus the kinetic energy of expansion for a steel plasma produced by RO laser irradiation is $\approx 0.29 \text{ eV}$. The respective laser power densities used to produce these plasmas were 10^{14} W m^{-2} and 10^9 W m^{-2} , thus we would expect the Nd laser ($F \approx 10^{10} \text{ W m}^{-2}$) to produce plasmas with expansion velocities and kinetic energies between those obtained by the other two plasma modes used.

The main difference between RO and QS mode plasmas is in the mode of material ejection. In the QS mode, material is ejected from the target principally as a dense vapour which is heated to temperatures of about 2 eV by absorption of the incoming laser beam. With RO mode lasers, the target material is initially ejected as a low density vapour which is transparent to the remaining part of the laser beam. Vapour emission is coincident with the laser spikes, ie the target is continually being heated to vaporisation and then cooling between spikes. After about 20 spikes (sec A3) heat is deposited faster than it can be conducted away and a layer of molten metal is formed which is blasted out of the crater by each subsequent laser spike. Deeper craters than those produced by QS lasers are formed.

Photographic evidence (Sec 3.2.6) showed that positioning of the electrodes and their potential are important in obtaining efficient spark excitation of QS plasmas. Setting too low a potential (\ll breakdown voltage) causes the spark to be initiated too late to have any effect on the target species, and thus a significant increase in spectral intensity of the target species is not obtained. Spark excitation has a much greater effect on RO mode plasmas due to the longer duration of the laser-target interaction.

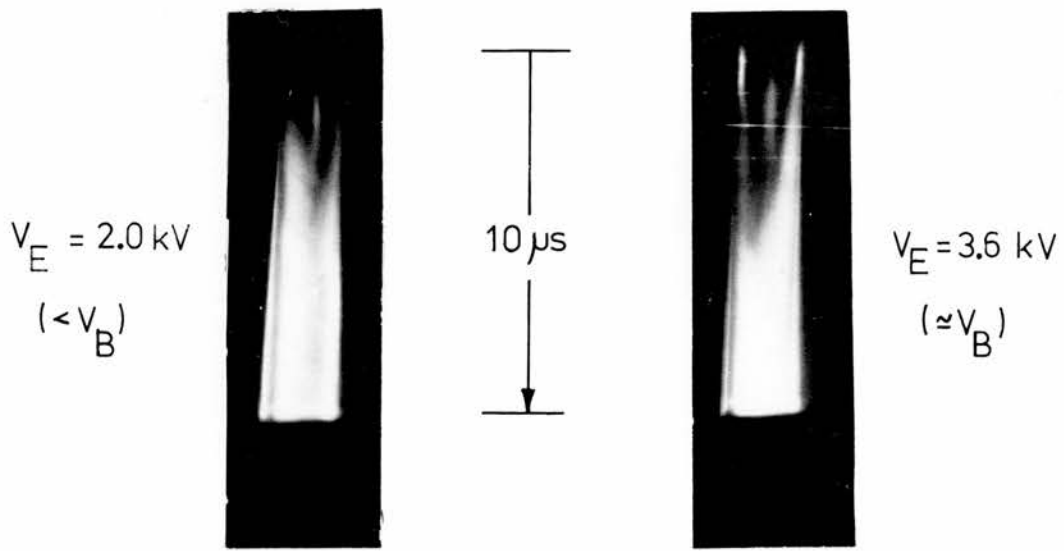


(a) Streak photographs

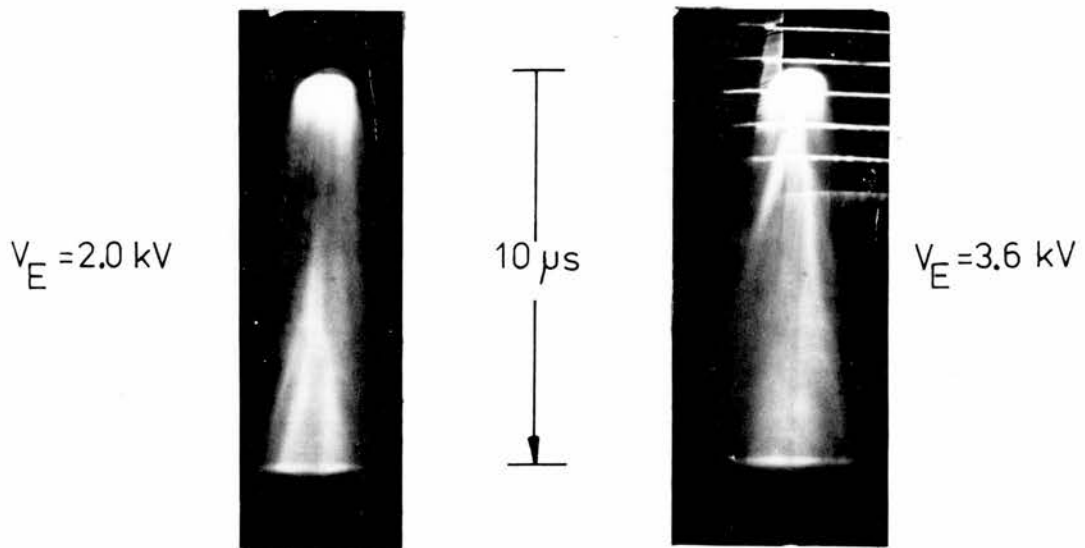


(b) Framing photograph

FIG A.1: HIGH SPEED PHOTOGRAPHS OF Q-SWITCHED LASER PRODUCED PLASMAS IN IRON.

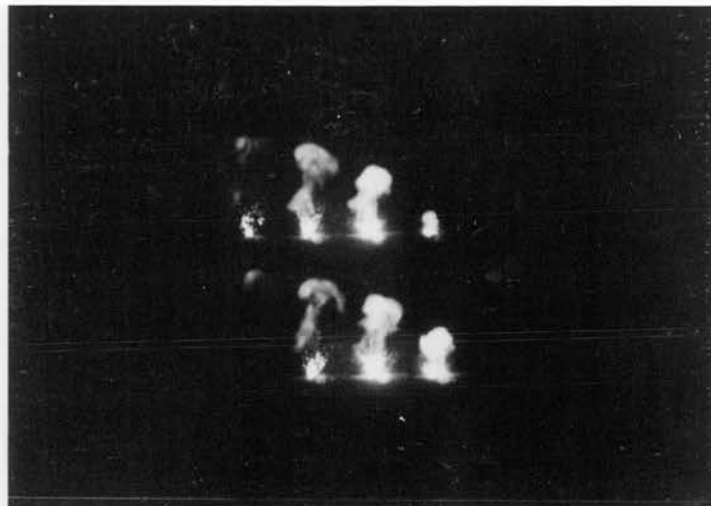


(a) at electrodes

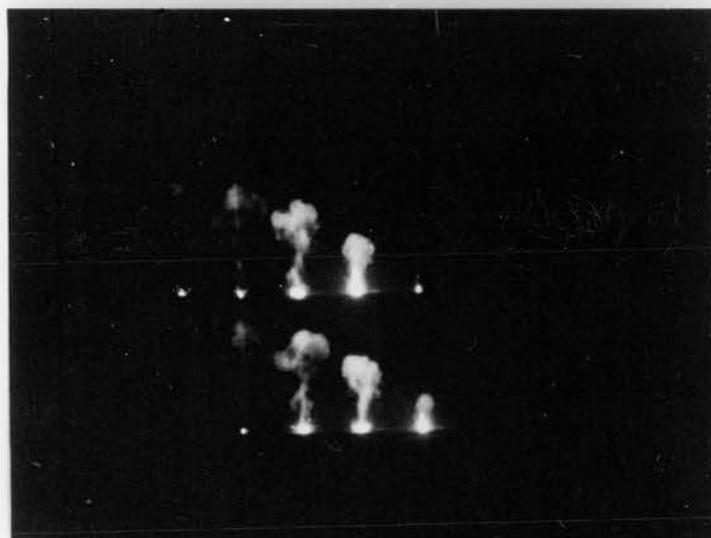


(b) at surface

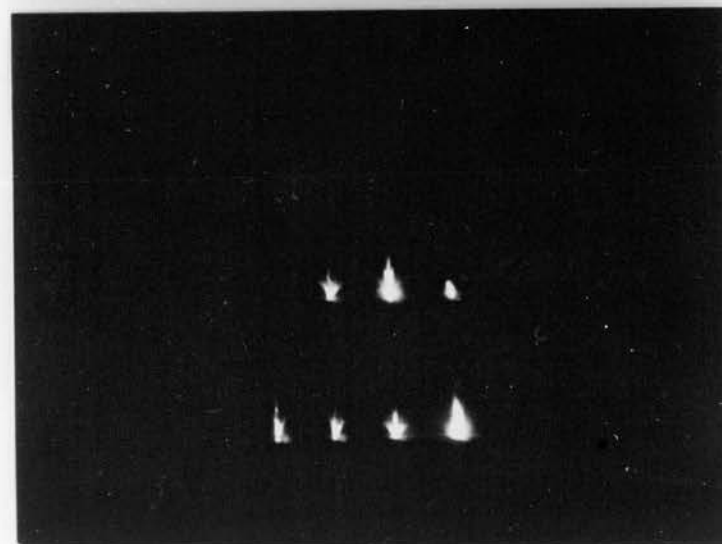
FIG A2: STREAK PHOTOGRAPHS OF QS-LASER PRODUCED PLASMAS IN IRON.



A



B



C

FIGURE A.3: LASER PRODUCED PLUMES IN
A. ALUMINIUM-SILICATE TARGET
B. MILD STEEL TARGET
C. LEAD TARGET

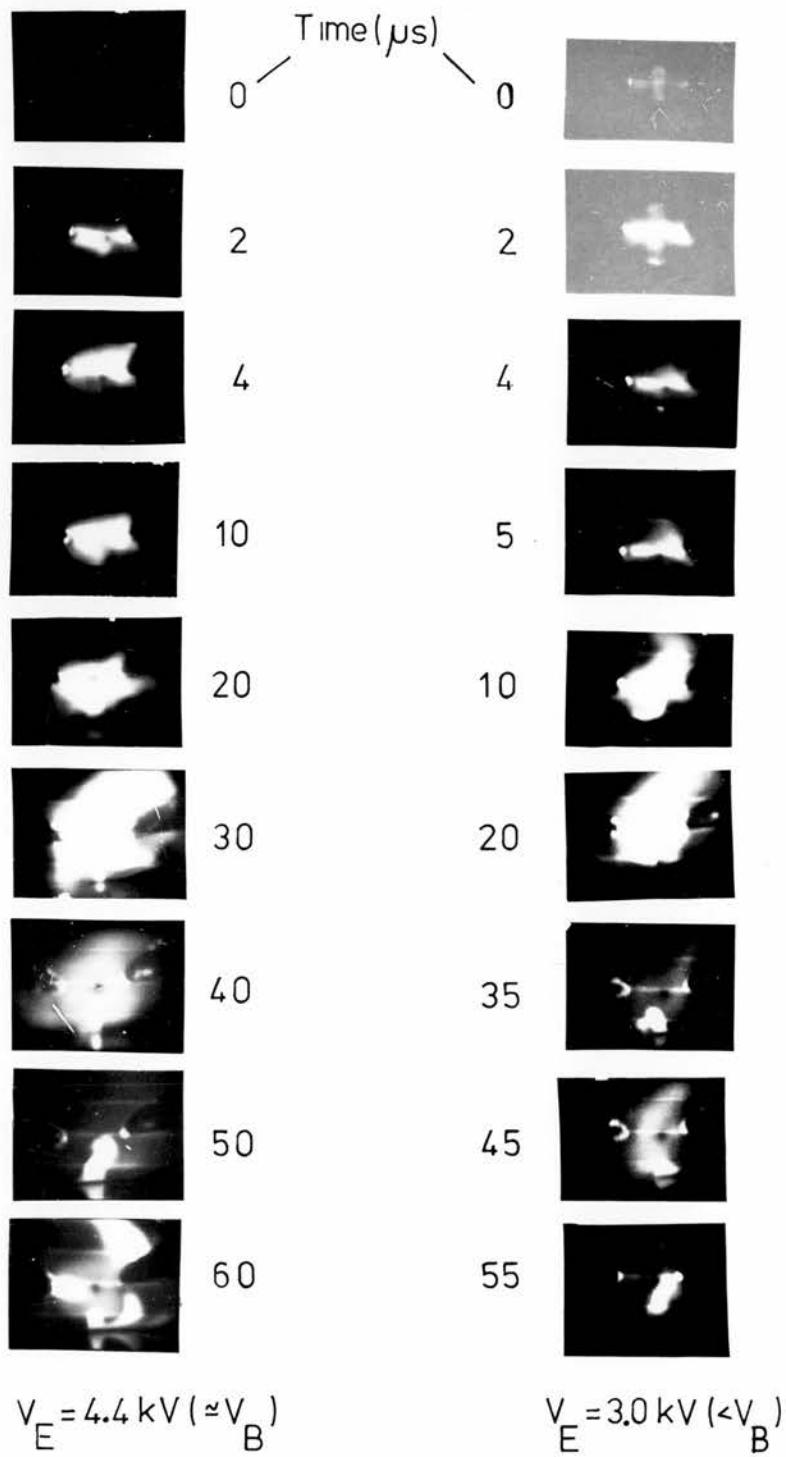


FIG A.4 : FRAMING PHOTOGRAPHS OF RO LASER PRODUCED PLASMAS IN IRON, WITH AUXILIARY EXCITATION.

APPENDIX B

RAT'S NEST CALORIMETER

A "rat's nest" calorimeter (Baker 1963) was used to measure the energy output of the Nd-glass and ruby lasers. The calorimeter was previously constructed in this department (Paul, 1972) and details of the construction together with Baker's analysis are given below.

In essence, the laser beam is fired into a bundle of fine copper wire packet into a silvered glass beaker. The beaker is sealed with a protective glass (or quartz) entrance window to prevent air disturbances. The laser beam is successively scattered and absorbed by the copper wire, resulting in a rise in temperature and electrical resistance of the wire. It is not necessary to wait for temperature equalization in this type of system, since the resistance change does not depend on the volume distribution of the wire. Two calorimeters are normally used in a Wheatstone bridge configuration, one as the measurement arm and one as the reference arm.

B.1 Construction

Figure B.1a shows the construction of the calorimeter. Two silvered beakers are mounted back-to-back within a metal tube and separated from the tube by a foam cushion. Approximately 1000 ft ($1 \Omega \text{ ft}^{-1}$) of fine insulated copper wire is packed loosely and randomly into each beaker. The wires from each beaker are joined at one end and a common terminal brought out for connection to a galvanometer. The free ends of the wire serve as terminals for connection into a measurement circuit. One beaker is sealed with a glass entrance window and the other with a quartz window, thus the calorimeter can be used to measure the energy of a wide range of pulsed lasers.

B.2 Baker's Analysis

The rat's nest is used in a conventional Wheatstone bridge circuit

(Fig B.1b). When a laser pulse is fired into the measurement arm of the calorimeter, the rise in resistance of an element of wire R'_0 will be given by

$$R_0 = R'_0 (1 + \alpha \Delta\theta), \quad (\Omega) \quad (B.1)$$

where α is the temperature coefficient of resistance and $\Delta\theta$ is the temperature rise. Thus the resistance change is

$$\Delta R' = R'_0 \alpha \Delta\theta \quad (\Omega) \quad (B.2)$$

If the element of wire absorbs energy E' joules, has a mass M' , and specific heat capacity C , then the temperature rise is

$$\Delta\theta = \frac{E'}{4.2 M' C} \quad (^\circ\text{C}) \quad (B.3)$$

Thus we have

$$\Delta R' = \frac{R'_0 E'}{4.2 M' C} \quad (\Omega) \quad (B.4)$$

Summing over the whole length of wire, we have

$$\Delta R = \frac{\alpha R_0}{4.2 M C} E' \quad (B.5)$$

$$= \frac{\alpha R_0}{4.2 M C} E \quad (\Omega) \quad (B.6)$$

where $R'_0/M' = R_0/M$ for wire of uniform cross section, R_0 , M and E are the total resistance, mass and absorbed energy, respectively.

The energy absorbed by the wire is given by

$$E = \frac{4.2 M C}{\alpha R_0} \Delta R \quad (\text{J}) \quad (B.7)$$

The term in brackets must be ascertained either experimentally by calibration with some source of known energy or by substitution of the correct values into the formula. In the latter case corrections must be applied for the losses due to backscatter of energy from the wire and for reflections in the window. An estimation is also required for the specific heat of the wire insulation. Applying these corrections Baker arrives at the following expression for the output energy of a laser pulse:

$$E = 2.38 \Delta R \text{ Joules.} \quad (B.8)$$

We have chosen to estimate the term in brackets experimentally.

B.3 "Rat's Nest" in Wheatstone Bridge Configuration

The rat's nest is normally used in a Wheatstone bridge configuration and the general circuit is shown in Fig B.1b. Initially the circuit is at balance, where we have

$$R_1 r_2 - R_2 r_1 = 0, \quad (\text{B.9})$$

When a laser pulse enters the measurement arm (say R_1) there is a resistance rise of ΔR in this arm and a current i flows through the galvanometer. Solving Kirkchoff's equations for the current loops, we find that the current is given by (eg Bleaney and Bleaney, 1957, p69)

$$i = \frac{V[(R_1 + \Delta R)r_2 - R_2 r_1]}{P + G \{[(R_1 + \Delta R) + R_2](r_1 + r_2)\}} \quad (\text{B.10})$$

where

$$P = [(R_1 + \Delta R)R_2 r_1] + (R_2 r_1 r_2) + r_1 r_2 (R_1 + \Delta R) + r_2 R_2 (R_1 + \Delta R)$$

and G is the galvanometer impedance, and i is in Amps.

The current i can be rewritten as

$$i = \frac{V [R_1 r_2 - R_2 r_1] + V r_2 \Delta R}{\Delta R (r R_2 G + r_1 r_2) + r_1 r_2 R + r R_1 r_2 + r R G} \quad (\text{A}) \quad (\text{B.11})$$

where $r = r_1 + r_2$ and $R = R_1 + R_2$

But from (B.9) we have $R_1 r_2 - R_2 r_1 = 0$, so we obtain

$$\Delta R = \frac{i(r_1 r_2 R + r R_1 R_2 + r R G)}{i(r R_2 G + r_1 r_2) - V r_2} \quad (\Omega) \quad (\text{B.12})$$

Since i is normally hundreds of nA for the energies we consider, we have

$$|i(r R_2 G + r_1 r_2)| \ll |V r_2|$$

and
$$\Delta R \approx \frac{(r_1 r_2 R + r R_1 R_2 + r R G)}{V r_2} \quad (\Omega) \quad (\text{B.13})$$

With the following circuit parameters, $R_1 = 999 \Omega$, $R_2 = 1009 \Omega$, $r_1 = 1189 \Omega$, $r_2 = 1201 \Omega$, $V = 18.63V$ and $G = 196 \Omega$, we get

$$\Delta R \approx (278 \times 10^3) i \quad (\Omega) \quad (\text{B.14})$$

or when i is measured in nA,

$$\Delta R = (278 \times 10^{-6})i \quad (\Omega) \quad (B.15)$$

B.4 "Rat's Nest" Calibration

The rat's nest was set up in the Wheatstone bridge circuit using the components shown above. The whole unit was calibrated using a cw 300A Argon-ion laser which operates with equal power output at 488 nm and 514.5 nm. The laser was fired into the rat's nest and the time taken for the galvanometer needle to reach a given deflection (ie a fixed value of current) was measured. The Argon-ion laser power output was measured on a power meter (accuracy $\pm 20\%$) before and after every measurement. The time taken for a given deflection was measured a number of times, and the average energy estimated for a given galvanometer current. This was repeated for various galvanometer deflections (ie current values). Thus a calibration curve of galvanometer current vs. laser energy was constructed (Fig B.2).

Applying a linear regression analysis to the data gave the following straight line,

$$E = 0.74 i - 3.13 \quad (\text{mJ}) \quad (B.16)$$

with i measured in nA. A coefficient of determination (goodness of fit) was estimated to be 0.99. In theory, the line should pass through the origin and the presence of this intercept value suggests that the rat's nest was not given enough cooling time between readings. In any case, in the range of energies with which we are interested (30-300 mJ), the maximum error in neglecting the intercept (at 30 mJ) is 10%. Thus for most purposes the value of

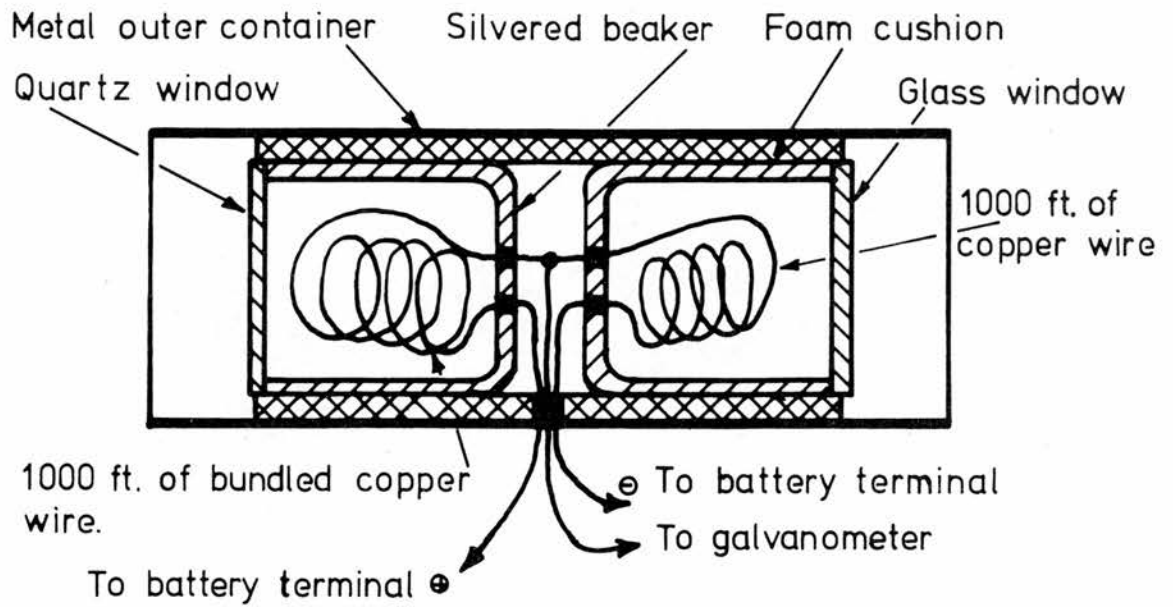
$$E \approx 0.74 i \quad (\text{mJ}) \quad (B.17)$$

with i in nA, will suffice.

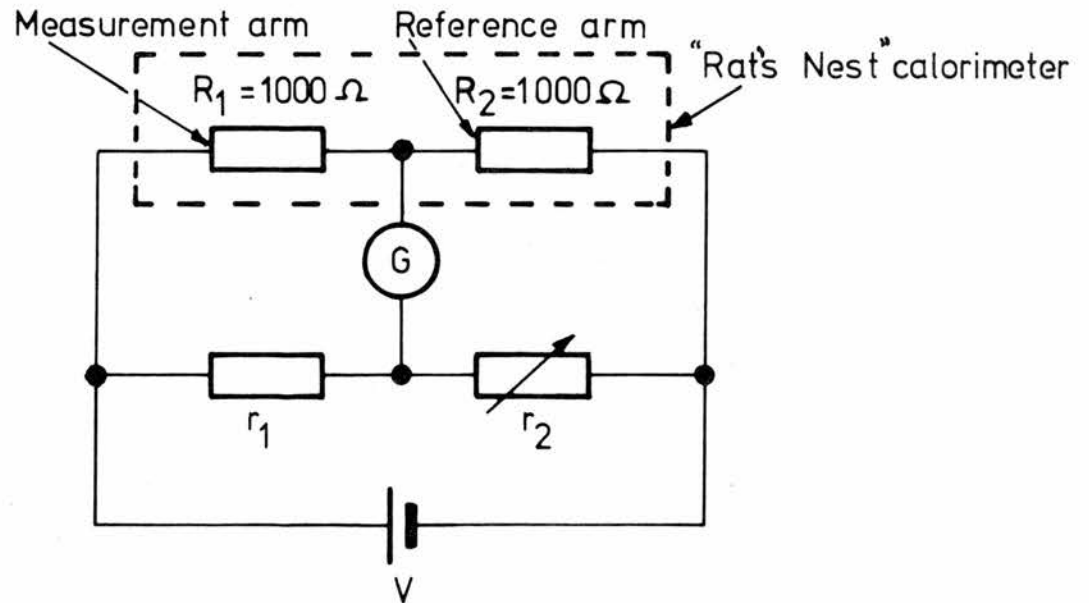
Returning to our value of ΔR (eqn B.15), we can substitute this in equation (B.17) and get

$$E = 2.66 \Delta R \quad (\text{mJ}) \quad (B.18)$$

The factor, 0.74 refers only to the circuit used .



(a). Construction of "Rat's Nest" calorimeter.



(b). "Rat's Nest" in Wheatstone bridge configuration.

FIG B.1: RAT'S NEST CALORIMETER: CONSTRUCTION AND CIRCUITRY.

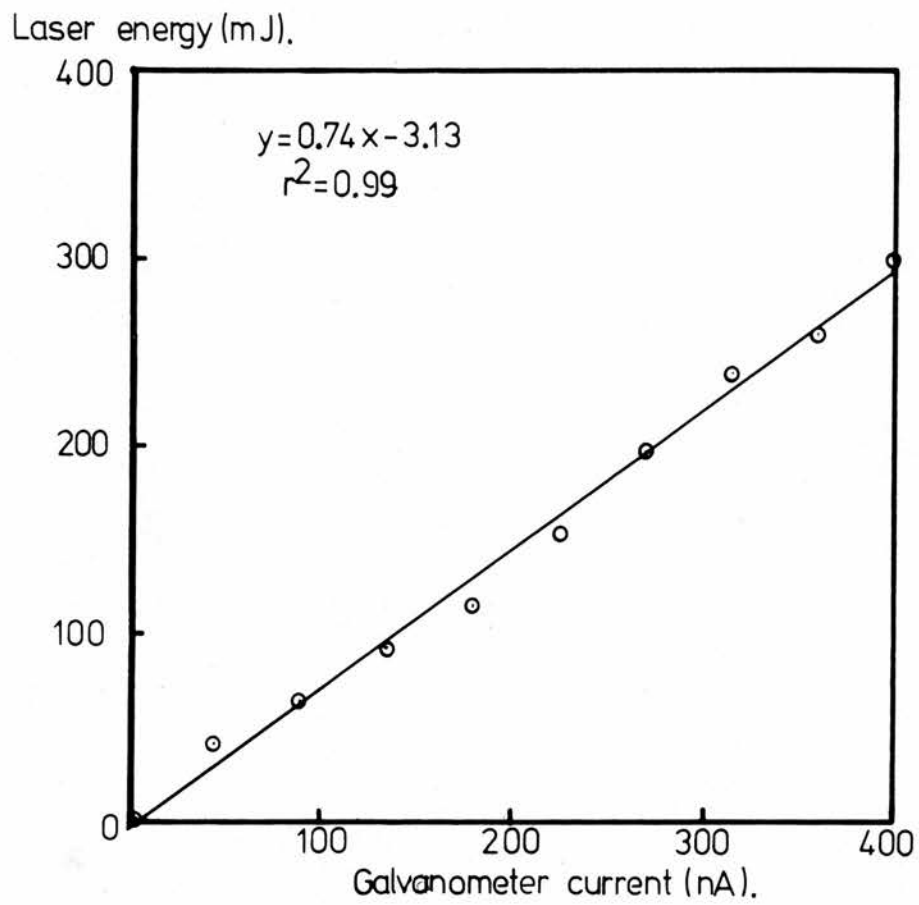


FIG B.2: CALIBRATION CURVE FOR 'RAT'S NEST' CALORIMETER.

APPENDIX C

SUMMARY OF STATISTICAL FORMULAE

Statistical techniques have been employed in the analysis of some of the data reported in the thesis. For reference, the formulae used are listed below. Nearly all of the statistical analysis was carried out on a Hewlett-Packard HP-25 Programmable Calculator, and some of the following functions are obtained directly from it.

C.1 Basic Definitions

(i) Mean

The mean of a set of data points $x_1, x_2 \dots x_n$ is given by

$$\bar{x} = \frac{1}{n} \sum_{i=1}^n x_i \quad (C.1)$$

(ii) Sample standard deviation (unbiased)

The unbiased estimate of the standard deviation of an infinite population for a sample of size n is given by

$$s = \left[\frac{\sum x_i^2 - (\sum x_i)^2/n}{n-1} \right]^{1/2} \quad (C.2)$$

Both these functions, \bar{x} and s are available directly on the HP-25.

(iii) Standard error of the mean

$$\alpha_m = s/n^{1/2} \quad (C.3)$$

Measurements are generally quoted as

$$x = \bar{x} \pm \alpha_m \quad (C.4)$$

(iv) Standard error of the standard deviation

$$\alpha_s = s/(2n)^{1/2} \quad (C.5)$$

C.2 Linear Regression

Linear regression techniques are used when we need to fit the best

straight line to a set of correlated data points x_i, y_i . We applied linear regression to the working curves in spectrochemical analysis and also to the determination of the electron temperature of laser produced plasmas.

We usually want to fit the straight line

$$y = ax + b \quad (C.6)$$

to a collection of data. In eqn (C.6), a is the regression coefficient (gradient) and b is the intercept. The HP-25 can be programmed to apply a linear regression using the following definitions:

(i) Regression coefficient (gradient)

$$a = \frac{\Sigma xy - (\Sigma x \Sigma y)/n}{\Sigma x^2 - (\Sigma x)^2/n} \quad (C.7)$$

(ii) Regression intercept

$$b = \bar{y} - a\bar{x} \quad (C.8)$$

(iii) Coefficient of determination

A measure of the goodness of fit of the data to the straight line can be estimated using the following definition

$$r^2 = \frac{[\Sigma xy - (\Sigma x \Sigma y)/n]^2}{[\Sigma x^2 - (\Sigma x)^2/n][\Sigma y^2 - (\Sigma y)^2/n]} \quad (C.9)$$

If $r^2 = 1$, perfect correlation exists between the sets of data x_i and y_i and if $r^2 = 0$ there is no correlation.

(iv) The Standard error of y on x

This is the standard error of the regression line of y on x and can be calculated from

$$\alpha_{yx} = \left[\frac{\Sigma y^2 - b\Sigma y - a\Sigma xy}{n-2} \right]^{1/2} \quad (C.10)$$

Confidence limits of $\pm (1-\beta)\%$ for all the y_i around the regression line is expressed for $(n-2)$ degrees of freedom by

$$\pm t_{n-2, \beta} \alpha_{yx} \left[\frac{1}{n} + \frac{(x_i - \bar{x})^2}{(n-1) s^2} \right]^{1/2} \quad (C.11)$$

where $t_{n-2,\beta}$ is Student's t-coefficient.

(v) Standard error of the gradient

$$\alpha_a = \alpha_{yx} / [s(n-1)^{\frac{1}{2}}] \quad (C.12)$$

The confidence limits of the gradient are given by

$$\pm t_{n-2,\beta} \alpha_a$$

(vi) Standard error of the intercept

$$\alpha_b = \alpha_a [\Sigma x^2/n]^{\frac{1}{2}} \quad (C.13)$$

The confidence limits of the intercept are given by

$$\pm t_{n-2,\beta} \alpha_{yx} \left[\frac{\Sigma x^2/n}{\Sigma x^2 - (\Sigma x)^2/n} \right]^{\frac{1}{2}} \quad (C.14)$$

(vii) Estimate of x from y

If it is desired to estimate the independent variable x from a measured value of dependent variable y, using a regression line of y on x, the following definitions are used

$$x = (y - b)/a \quad (C.15)$$

and the standard error of the estimated value is

$$\alpha_x = \frac{\alpha_{yx}}{a} \left[\frac{1}{m} + \frac{1}{n} + \frac{(y - \bar{y})^2}{a^2 [\Sigma x^2 - (\Sigma x)^2/n]} \right]^{\frac{1}{2}} \quad (C.16)$$

where y is an average of m measurements (Bennett and Franklin, 1954).

This is the case met in spectrochemical analysis when the element concentration (independent variable) is estimated from measured spectral intensity ratios (dependent variable).

APPENDIX D

TERMINOLOGY, UNITS AND SYMBOLS

D.1 Terminology and Units

SI units are used throughout this thesis with one exception, where molar quantities are involved we use the kilogram-mole (kmol) instead of the gram-mole (mol). Energy levels, electron temperatures and ion temperatures are always quoted in electron-volts (eV). (Note: $1\text{eV} \equiv 11605\text{ K}$).

In the mathematical analysis of Chapter 1, the term "log" denotes logarithms to the base 10 and the term " \ln " denotes logarithms to the base e.

Unless stated otherwise, wavelengths of spectral lines are given in nanometres (nm). In accordance with standard practice, the symbol "I" when accompanied by a spectral line wavelength denotes that the line belongs to the atomic species, "II" denotes first ionisation state, "III" denotes second ionisation state etc.

The following terms occur frequently in the thesis:

BB : black body emission.

RO : Relaxation oscillator mode of laser operation.

QS : Q-Switched mode of laser operation.

LTE: Local thermodynamic equilibrium.

LMSA: Laser Micro-spectral Analysis.

Radiance : Energy emitted by an atomic transition per unit area, per second per steradian. Denoted by the symbol "I" and often referred to as line intensity in the literature.

Intensity: used in this thesis to denote the magnitude of a photographically or photometrically recorded spectral line.
Denoted by the symbol "J".

Working curve: Curve of log spectral intensity ratio of plasma vs log concentration ratio of target.

D.2 Symbols

The following symbols are used in this thesis.

A_o	:	kg atomic weight.
A_{mn}	:	Atomic transition probability (s^{-1}) of a spectral line λ_{mn} .
A_{pq}^z	:	Atomic transition probability (s^{-1}) of a spectral line λ_{pq} .
A_{mn}	:	Atomic transition probability of spectral line λ_{mn} of atom in ionisation state z .
A_{pq}^{z+1}	:	Atomic transition probability of spectral line λ_{pq} of atom in ionisation state $z+1$.
a	:	thermal diffusivity ($m^2 s^{-1}$).
a	:	regression coefficient (gradient).
a_o	:	dimensional constant related to a_v ($m^8 kg^{-2} s^{-3}$).
a_v	:	plasma absorption coefficient (m^{-1}).
B	:	dimensional constant ($kg m^{-3}$) related to saturated vapour density.
b	:	regression intercept.
C	:	specific heat capacity ($J kg^{-1} K^{-1}$).
c	:	velocity of light ($m s^{-1}$).
c_1	:	adiabatic sound velocity ($m s^{-1}$).
D	:	diameter of aperture.
D	:	optical density.
d	:	diffraction limited laser spot diameter.
d_v	:	optical depth (dimensionless).
E	:	total energy absorbed by copper wire (J).
E'	:	energy absorbed in short element of copper wire (J).
E_m	:	Excitation energy of m 'th atomic energy level (eV).
E_p	:	Excitation energy of p 'th atomic energy level (eV).
E_m^z	:	Excitation energy of m 'th atomic energy level of atom in ionisation state z .
E_p^{z+1}	:	Excitation energy of p 'th atomic energy level of atom in ionisation state $z+1$.
E_q	:	Excitation energy of q 'th atomic energy level.
\vec{E}	:	Electric field vector.
E_x	}	Electric field components.
E_y		
E_z		
e	:	electron charge (C)
F	:	power density ($W m^{-2}$).
F_a	:	absorbed power density ($W m^{-2}$).
F_{min}	:	minimum power density required for evaporation to take place.
f	:	focal length.

G	:	Gaunt factor.
G	:	Galvanometer impedance (Ω).
g_m	:	statistical weight of m'th energy level.
g_p	:	statistical weight of p'th energy level.
g_m^z	:	statistical weight of m'th energy level of atom in ionisation state z.
g_p^{z+1}	:	statistical weight of p'th energy level of atom in ionisation state z+1.
H_{pq}	:	Irradiance at photographic emulsion ($W m^{-2}$) due to spectral line λ_{pq} .
H_{mn}	:	Irradiance at photographic emulsion ($W m^{-2}$) due to spectral line λ_{mn} .
h	:	Planck's Constant.
I_{mn}	:	Radiance emitted from plasma by spectral line λ_{mn} ($J m^{-2} s^{-1} sr^{-1}$).
I_{pq}	:	Radiance emitted from plasma by spectral line λ_{pq} ($J m^{-2} s^{-1} sr^{-1}$).
I_{pq}^{z+1}	:	Radiance emitted from plasma by spectral line λ_{pq} of atom in ionisation state z+1.
I_{mn}^z	:	Radiance emitted from plasma by spectral line λ_{mn} of atom in ionisation state z.
i	:	current through galvanometer (A).
J_{mn}	:	Photographically measured intensity of spectral line λ_{mn} .
J_{mn}^R	:	Photographically measured intensity of spectral line λ_{mn} of element R.
J_{pq}	:	Photographically measured intensity of spectral line λ_{pq} .
J_{pq}^A	:	Photographically measured intensity of spectral line λ_{pq} of element A.
K	:	thermal conductivity ($W m^{-1} K^{-1}$).
K_o	:	constant for a given pair of spectral lines at a given temperature.
k	:	Boltzmann's constant.
L	:	homogeneous layer of plasma.
L_s	:	latent heat of sublimation ($J kg^{-1}$).
L_v	:	latent heat of vaporisation ($J kg^{-1}$).
ℓ	:	plasma depth.
M	:	mass of target evaporated per unit area and converted into plasma.
M	:	total mass of copper wire.
M'	:	mass of element of copper wire.
m_e	:	electron mass (kg).
N	:	total number density of particles in plasma (m^{-3}).
N(A)	:	number density of particles of element A. (m^{-3}).
N(R)	:	number density of particles of element R. (m^{-3}).
N_e	:	electron density (m^{-3}).
$N_e(\min)$:	minimum electron density required for LTE conditions to hold in plasma.
N_i	:	ion density (m^{-3}).

N_p	:	particle density in level p (m^{-3}).
N_p^{z+1}	:	particle density in level p of atom in ionisation state z+1 (m^{-3}).
N_m^z	:	particle density in level m of atom in ionisation state z (m^{-3}).
n	:	number of data points.
P	:	resistance (Ω).
P_{Br}	:	power radiated due bremsstrahlung emission ($W m^{-3}$).
p	:	pressure ($J m^{-3}$).
p_o	:	pressure of solid phase ($J m^{-3}$).
p_1	:	pressure of vapour phase ($J m^{-3}$).
p_A	:	ablation pressure ($J m^{-3}$).
p_{sat}	:	saturated vapour pressure ($J m^{-3}$).
Q	:	exposure of photographic emulsion ($J m^{-2}$).
Q_{pq}	:	exposure due to spectral line λ_{pq} ($J m^{-2}$).
Q_{mn}	:	exposure due to spectral line λ_{mn} ($J m^{-2}$).
R	}	: resistance (Ω).
R_1		
R_2		
R'_o	:	initial resistance of element of copper wire.
R_o	:	resistance of copper wire.
R_g	:	general gas constant ($J K^{-1} k mol^{-1}$).
r	}	: resistance
r_1		
r_2		
r_{41}	}	: electro-optic coefficients.
r_{63}		
r^2	:	coefficient of determination.
s	:	sample standard deviation.
T_o	:	temperature at surface of metal (K)
T	:	temperature.
T_e	:	electron temperature (eV).
T_i	:	ion temperature (eV).
T_a	:	ambient temperature.
T_v	:	vaporisation temperature.
T_1	:	temperature of vapour (eV).
t	:	time
t_ℓ	:	laser pulse duration
$t_{n-2,\beta}$:	the Student's t-coefficienc, for n data points and confidence limits of (1- β)%.

t_v	:	time at which vaporisation occurs.
u	:	velocity at which molten metal layer recedes into bulk metal.
V	:	voltage.
V_E	:	electrode voltage.
V_B	:	breakdown voltage of free space.
V_z	:	z-component of voltage (half-wave voltage).
v	:	velocity.
v_1	:	expansion velocity of vapour.
x	:	rectangular coordinate.
x_t	:	depth vaporised after time t .
\bar{x}	:	mean of x_i , where $i = 1, 2, 3, \dots, n$.
\hat{x}	:	measured (or estimated) value of x .
x_i	:	i 'th data point.
y	:	rectangular coordinate.
\bar{y}	:	mean of y_i , where $i = 1, 2, 3, \dots, n$.
\hat{y}	:	measured value of y .
Z	:	partition function.
$Z(A)$:	partition function of element A.
$Z(R)$:	partition function of element R.
z	:	rectangular coordinate.
z	:	effective charge of ion.
α	:	temperature coefficient.
α_a	:	standard error of gradient of regression line.
α_b	:	standard error of intercept of regression line.
α_m	:	standard error of mean.
α_s	:	standard error of standard deviation.
$\alpha_{\hat{x}}$:	standard error of value of \hat{x} , estimated from measured \hat{y} via a regression line.
$\alpha_{\hat{x}}(\min)$:	minimum value of $\alpha_{\hat{x}}$ obtained at (\bar{x}, \bar{y}) .
α_{yx}	:	standard error of regression line of y on x .
β	:	confidence limits, specified as $(1-\beta)\%$.
γ	:	specific heat ratio.
γ	:	slope of linear position of characteristic curve of photographic emulsion.
$\Delta\mu$:	change in refractive index.
ΔR	:	resistance change.
$\Delta R'$:	resistance change of element of copper wire.
Δt	:	increment of time.
$\Delta\theta$:	increment of temperature.
ϵ	:	internal energy.
ϵ_1	:	internal energy of vapour.
ϵ_0	:	permittivity of free space.

η	:	dimensionless parameter.
θ	:	beam divergence.
λ	}	dimensionless constants.,
λ_1		
λ_2		
λ	:	wavelength.
λ_0	:	wavelength in free space.
λ_{pq}	:	wavelength of line emitted between energy levels p and q.
λ_{mn}	:	wavelength of line emitted between energy levels m and n.
λ_{pq}^{z+1}	:	wavelength of line emitted between energy levels p and q of atom in ionisation state z+1.
λ_{mn}^z	:	wavelength of line emitted between energy levels m and n of atom ionisation state z.
μ	:	refractive index.
μ_x	}	rectangular components of refractive index.
μ_y		
μ_z		
ν	:	frequency.
ν_p	:	plasma frequency.
ν_t	:	frequency of transition between black body and bremsstrahlung emission.
ρ	:	density (kg m^{-3}).
ρ_0	:	density of solid (kg m^{-3}).
ρ_1	:	density of vapour.
ρ_{sat}	:	saturated vapour density.
τ	:	light loss factor.
\emptyset	:	phase retardation.
ω	:	solid angle.

APPENDIX E
PUBLISHED PAPERS

APPENDIX F

NOTE ADDED IN PROOF

RECALCULATION OF ELECTRON TEMPERATURES USING REVISED TRANSITION PROBABILITIES

Recently revised spontaneous transition probabilities (A-coefficients) have become available for Fe I and Fe II lines which are regarded as being more accurate than those calculated by Corliss and Bozmann (1962). The electron temperatures quoted in Sec 3.1 of this thesis have been re-calculated using these revised transition probabilities.

Figure F1 shows plots of $\ln(g_1 A_{12} \lambda_{21} I_2 / g_2 A_{21} \lambda_{12} I_1)$ vs $(E_2 - E_1)$ for each of the modes of excitation used in this thesis. The transition probabilities were taken from the compilation by Fuhr (to be published) and are accurate to $\pm 25\%$. The error bars shown in Fig F1 show the typical uncertainty (one standard deviation) associated with a 25% error in transition probability and a 10% error in measured spectral intensity. The estimated electron temperatures are shown in Table F1 together with the error (one standard error) associated with the uncertainty in the gradient (calculated using eqn C12).

Temperatures estimated using Fe I lines pairs are also shown in Table F1. The transition probabilities for Fe I lines were taken from Blackwell et al (1976, 1978), Banfield and Hooper (1973), Hooper and Parkinson (1972) and Bridges and Kornblith (1974) and are 3-25% accurate.

References

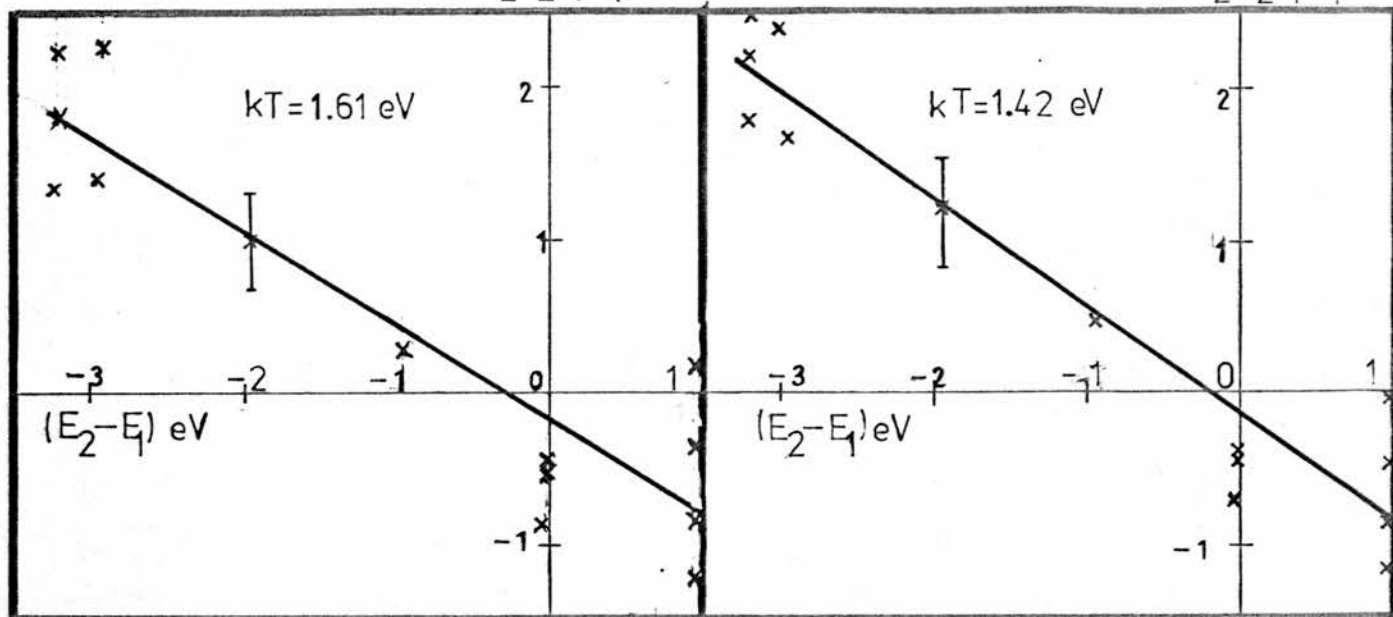
1. Banfield F P, Hooper M C E (1973), *Astrophys J* 186, 335-346.
2. Bridges J M, Kornblith R L (1974), *Astrophys J* 192, 793-812.
3. Blackwell D E, Ibbotson P A, Petford A D, Shallis M J (1978) *Monthly Notices Royal Astr Soc* 186.
4. Blackwell D E, Petford A D, Shallis M J (1978) *Monthly Notices Royal Astr Soc* 186.
5. Blackwell D E, Ibbotson P A, Petford A D, Shallis M J (1976) *Monthly Notices Royal Astro Soc* 177.
6. Fuhr J R (to be published - NBS).
7. Hooper M C E, Parkinson W H (1972), *Astrophys J*, 172, 229-247.

TABLE F1

<u>Excitation mode</u>	Fe II				Fe I		
	<u>kT(eV)</u>	<u>SE</u>	<u>r²</u>	<u>n</u>	<u>kT(eV)</u>	<u>r²</u>	<u>n</u>
Spark-assisted RO	1.61	+ .24	0.84	14	0.90	0.91	8
		- .18					
Spark-assisted QS	1.42	+ .12	0.91	14	0.84	0.89	5
		- .12					
Unsparked RO	1.69	+ .25	0.88	10	1.01	0.76	11
		- .20					
Unsparked QS	1.61	+ .31	0.84	10	0.91	0.65	9
		- .22					

$$\ln \frac{g_1 A_1 I_2 \lambda_2}{g_2 A_2 I_1 \lambda_1}$$

$$\ln \frac{g_1 A_1 I_2 \lambda_2}{g_2 A_2 I_1 \lambda_1}$$

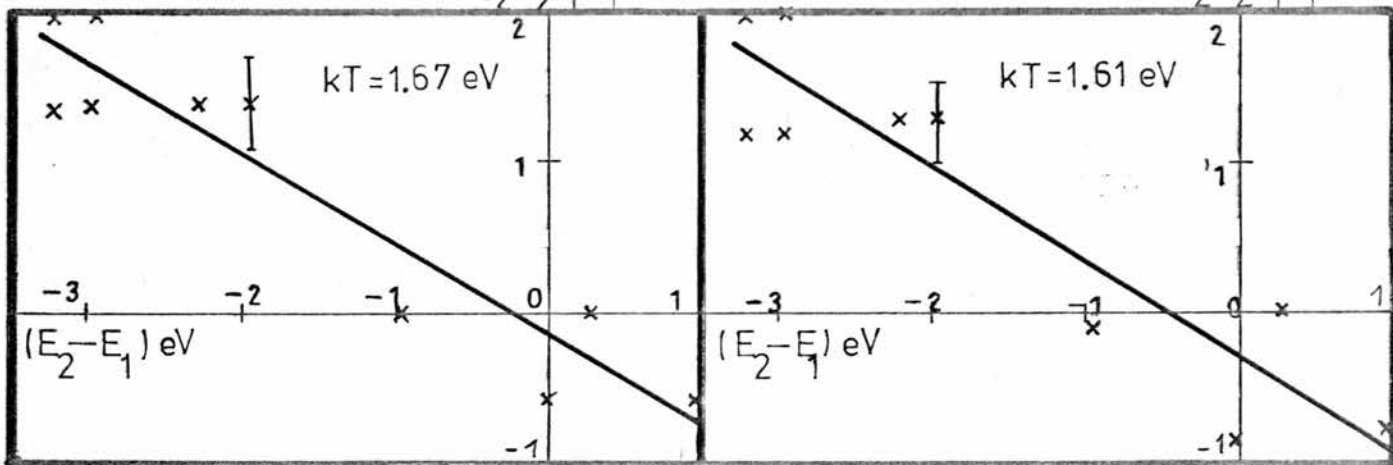


RO mode + spark

QS mode + spark

$$\ln \frac{g_1 A_1 I_2 \lambda_2}{g_2 A_2 I_1 \lambda_1}$$

$$\ln \frac{g_1 A_1 I_2 \lambda_2}{g_2 A_2 I_1 \lambda_1}$$



RO mode

QS mode

Plots of $\ln(g_1 A_1 I_2 \lambda_2 / g_2 A_2 I_1 \lambda_1)$ vs $(E_2 - E_1)$ constructed using Fe II line pairs.

FIG F1: ELECTRON TEMPERATURES OF Fe PLASMAS PRODUCED USING THE FOUR EXCITATION MODES.

REFERENCES

1. Adams W E (1968), Lawrence Radiation Lab UCRL-50463.
2. Adrain R S (1977), private communication.
3. Afanasyev Y V, Krokhin O N, Sklizkov G V (1966), IEEE Jnl Quant Elec. QE-2, 483-486.
4. Afanasyev Y V, Korkhin O N (1967), Sov Phys JETP 25, 639-645.
5. Ahrens L H, Taylor S R (1961), "Spectrochemical Analysis" 2nd ed (Pergamon Press).
6. Archbold E, Harper D W, Hughes T P (1964) Brit Jnl App Phys 15, 1321-1326.
7. Askaryan G A, Moroz E M (1963), Sov Phys JETP 16, 1638-1639.
8. Baker R M (1963) Electronics 36, Feb 1, 36-38.
9. Baldwin J M (1970), App Spectrosc 24, 429-435.
10. Batanov B A, Bogatyrev V A, Sukhodrev N K, Fedrov V B (1973), Sov Phys JETP 37, 419-423.
11. Bennett C A, Franklin N L (1954), "Statistical Analysis in Chemistry and Chemical Engineering" (Wiley).
12. Betz H T, Johnson G L (1971), "Analytical Emission Spectroscopy Vol 1, Pt I", 323-381, Ed E L Grove (Dekker).
13. Bleaney B I, Bleaney B (1957), "Electricity and Magnetism" (Oxford).
14. Boland B C, Irons F E, McWhirter R W P (1968), J Phys B (Ser 2) 1, 1180-1191.
15. Boumans P W J M (1966), "Theory of spectrochemical Excitation" (Hilger).
16. Boumans P W J M (1972), "Analytical Emission Spectroscopy Vol 1, Pt II", 107-180, Ed E L Grove (Dekker).
17. Carslaw H S, Jaeger J C (1959), "Conduction of Heat in Solids" 2nd ed (Oxford).
18. Caruso A, Bertotti B, Giupponi P (1966), Nuovo Cimento 45B, 176-188.
19. Caruso A, Gratton R (1968), Plasma Phys 10, 867-877.
20. Cerrai E, Trucco R (1968), Energia Nucleare 15, 581-587.
21. Chang W S C (1969), "Principles of Quantum Electronics" (Addison-Wesley).
22. Cooper J (1966), Rep Prog Phys 29, 35-130.
23. Corliss C H, Bozmann W R (1962) "Experimental Transition Probabilities for Spectral Lines of Seventy Elements" NBS-22 (NBS).
24. De Michelis C (1970), IEEE Jnl Quant Elec QE-6, 630-641.
25. Feldman C (1960), "Encyclopaedia of Spectroscopy" 222-224, Ed G L Clark (Reinhold).
26. Griem H R (1964), "Plasma Spectroscopy" (McGraw-Hill).
27. Hughes T P (1975), "Plasmas and Laser Light" (Hilger).
28. Kaminov I P, Turner E H (1966), Proc IEEE 54, 1374-1390.

29. Krokhin O N (1965), Sov Phys Tech Phys 9, 1024-6.
30. Krokhin O N (1972), "Laser Handbook" 1371-1407, Eds F T Arrechi,
E O Schulz-Dubois (North Holland).
31. Landau H G (1950), Quant J App Maths 8, 81-94.
32. Landau L D, Lifshitz E M (1959) "Fluid Mechanics" (Pergamon Press).
33. Ley J M, Christmas T M, Wildey C G (1970), Proc Inst Elec Eng
117, 1057-1062.
34. Lochte-Holtgreven W (1968), "Plasma Diagnostics" Ed. (North Holland).
35. Longhurst R S (1967) "Geometrical and Physical Optics" 2nd ed. (Longmans).
36. Maitland A, Watson J (1976) "Electro-Optics/Laser International '76:
Conference Proceedings" 167-172, Ed H G Jerrard (IPC).
37. McWhirter R W P (1965), "Plasma Diagnostic Techniques" 205-264,
Eds R H Huddleston, S L Leonard (Academic Press).
38. Mees C E K (1954), "The Theory of Photographic Process" (McMillan).
39. Mika J, Torok T (1974), "Analytical Emission Spectroscopy" (Butterworth).
40. Moenke H, Moenke-Blankenburg L (1973), "Laser Micro-Spectrochemical Analysis" (Hilger)
41. Moenke-Blankenburg L (1972), Nouv Rev Optique Appliquee 3 243-248.
42. Morton K L, Nohe J D, Madsen B S (1973), App Spectrosc 27, 109-117.
43. Nohe J D, Morton K L (1970), Western Elec Eng 14, 34-41.
44. Paul D M (1972), "PhD Thesis - The Stimulated Raman Effect", Univ. of St Andrews.
45. Petkov A P, Petkova L G, Dimitrov G (1969), Comptes Rendus de l'acad. Bulg
des Sciences 22, 983-988.
46. Piepmeier E H, Malmstadt M V (1969), Anal Chem 41, 700-707.
47. Raspberry S D, Scribner B F, Margoshes M (1967), App Opt 6, 81-93.
48. Ready J F (1971), "Effects of High Power Laser Radiation" (Academic Press).
49. Schroth H (1972), Z Anal Chem 261, 21-29 (In German).
50. Scott R H, Strasheim A (1970), Spectrochim Acta 25B, 311-332.
51. Watson, J, Maitland A (1977), J Phys E (Sci Instr) 10, 1227-8.
52. Wieise W L, Smith M W, Miles B M (1969), "Atomic Transition Probabilities
Vol II" NSRDS-NBS22 (NBS).
53. Yamane T, Matsushita S (1972), Spectrochim Acta 27B, 27-33.